ELECTRONIC STRUCTURE AND THERMOELECTRIC PROPERTIES OF NARROW BAND
GAP SEMICONDUCTORS AND PSEUDO-GAP SYSTEMS

By

Dat Thanh Do

A DISSERTATION

Submitted
to Michigan State University
in partial fulfillment of the requirements
for the degree of

Condensed Matters Physics - Doctor Of Philosophy

2013

ABSTRACT

ELECTRONIC STRUCTURE AND THERMOELECTRIC PROPERTIES OF NARROW BAND
GAP SEMICONDUCTORS AND PSEUDO-GAP SYSTEMS

By

Dat Thanh Do

The direct energy conversion from heat to electricity without any moving part using the thermo-electric effects is attractive and has many promising applications in power generation and heat pumping (refrigeration) devices. However, the wide use of thermoelectric materials in daily life is still not practical due to its low efficiency. Presently, there has been renewed interest in thermo-electrics with new strategies for improving the efficiency, mostly by controlling the morphology and dimensionality, and manipulating the electronic structure of novel complex systems. There are new questions arise and several old questions have not yet been answered. My group at Michigan State University has been actively working on narrow band gap semiconductors and pseudo-gap systems including BiTe, BiSe, SbTe, $AgPb_mSbTe_{m+2}$ (LAST), III-VI compounds, Mg_2Si, Cu_3SbSe_4, Fe_2VAl, ZrNiSn, etc. , focusing on their thermoelectrics related properties. This dissertation tries to address some of the fundamental questions on the electronic structure and related thermoelectric properties of narrow band gap semiconductors and pseudo-gap systems, employing the state-of-art density functional theory (DFT) and Boltzmanns transport equation. I focuses on some well-known materials including Heusler compound, Fe_2VAl, tetrahedrally bonded compounds (Cu_3SbSe_4 and related systems) and a newly reported novel nanocomposite system of Half-Heusler–Heusler (ZrNiSn–$ZrNi_2Sn$). For the first two systems (Heusler and tetrahedrally coordinated systems), the effects of correlated electrons in the system containing d-electrons, valency of sp-elements, and the role of lone-pair electrons in band gap formation and effects on thermoelectric properties are fully investigated. For the third system, Half-Heusler–Heusler nanocomposite, I report a detailed energetics analysis of the nanostructure formation and its effects on the electronic structures of the interested systems.

To my family

ACKNOWLEDGEMENTS

TABLE OF CONTENTS

LIST OF TABLES

LIST OF FIGURES

LIST OF SYMBOLS AND ABBREVIATIONS

α Ratio of exact Hartree-Fock exchange in hybrid functional HSE06

ε_0 Electrical susceptibility

ε_i Eigenvalue of a single-electron wavefunction

η_c Carnot efficiency

$\hbar$ Planc's constant

κ Thermal conductivity

κ_i Thermal conductivity of element i

κ_{elec} Thermal conductivity due to electrons

κ_{latt} Thermal conductivity due to lattice vibration

ω Screening parameter in hybrid functional HSE06

Ψ Many-body wavefunction

ψ_i Single-electron wavefunction

σ Electrical conductivity

$\tau_{\mathbf{k}}$ Relaxation time of carrier with momentum $\mathbf{k}$

σ, σ_i Spin index

a_0 The first Bohr radius, $a_0 = \frac{4\pi\varepsilon_0\hbar^2}{m_e e^2} \approx 0.529\text{Å}$

E_{xc} Exchange-correlation energy

$f(\varepsilon)$ Fermi-Dirac distribution, $f(\varepsilon) = \frac{1}{e^{\beta(\varepsilon-\mu)}+1}$

U On-site Coulomb repulsion parameter in LDA+U

COP   Coefficient of Performance, percent (%)

DFT   Density functional theory

FH   (Full) Heusler compounds, in this thesis it is usually referred to $ZrNi_2Sn$

GGA   Generalized gradient approximation

HFA   Hartree-Fock approximation

HH   Half-Heusler compounds, in this thesis it is usually referred to ZrNiSn

HSE06 Hybrid functional with screened exact exchange potential proposed by Heyd, Scuseria and Ernzerhof

IEA   International Energy Agency

KS   Kohn-Sham

L(S)DA Local (spin) density approximation

LDA+U, GGA+U LDA, GGA with on-site Coulomb repulsion correction

NBGS Narrow-band-gap semiconductor

RPA   Random phase approximation

TE   Thermoelectric(s)

TEG   Thermoelectric generator

TI   Topological insulator

$\mathbf{E}$ Electrical field

E Total energy of a system

e Electron's charge

$\hat{H}$ Hamiltonian operator

k_B Boltzmann's constant, $k_B = 8.6173324 \times 10^5 \text{eV/K}$

m_e Electron's mass

N Number of electrons

$\hat{n}$ $\hat{n}(\mathbf{r}) = \sum_{i=1,N} \delta(\mathbf{r} - \mathbf{r}_i)$ is the particle density operator

$\hat{O}$ Operator corresponding to an observable

S Seebeck coefficient or thermopower

S_i Thermopower of element i

T Operating temperature ($T = (T_h + T_c)/2$)

T_c Temperature of heat sink

T_h Temperature of heat source

$\hat{T}$ Kinetic energy operator

$\hat{V}_{ext}$ External potential operator

$\hat{V}_{int}$ Electron-electron interaction potential operator

Z Figure of merit

ZT Dimensionless figure of merit, where T is temperature

CHAPTER 1

INTRODUCTION

1.1 Thermoelectrics

In this era of technology, energy is a key factor in any economy. In fact, our world runs on energy. According to International Energy Agency (IEA) "World energy outlook 2012"[1], 81% of total primary energy consumption is fossil fuel preserved in the form of coal, petroleum, and natural gas. The energy consumption has increased about 35% from 1990 to 2010 and the same rate is expected for the next tens years. This brings the world's energy demand up to about 15 billions tonne of oil equivalent (toe) (or about six hundred millions Watt-second) per year by 2035. The reserve sources of fossil fuel are limited and will run out in the future. There is therefore an urgent need to use energy more efficiently and to find other sustainable forms of energy such as solar, wind power, bio fuel cell, etc. Among the ongoing directions, thermoelectric converters, with high enough efficiency, can serve well for both purposes.

1.1.1 Brief history of thermoelectrics

Thermoelectric converter directly converts heat gradient into electrical current or vice versa. The mechanism behind such devices is the thermoelectric effect which is usually referred to as Seebeck-Peltier effect to honor the two physicist who discovered it almost two centuries ago.

In 1821, the Baltic German physicist Thomas Johann Seebeck discovered that a circuit of two dissimilar metals could deflect the compass needle when exposed to a temperature gradient.[2] Seebeck, however, first thought it was "Magnetism induced by the temperature difference". It was quickly realized that the temperature difference produces a potential (voltage V) which drives an electrical current through a closed circuit, and that current deflects the compass needle. It was Hans Christian Ørsted, a Danish physicist, who first used the term "thermoelectricity". The
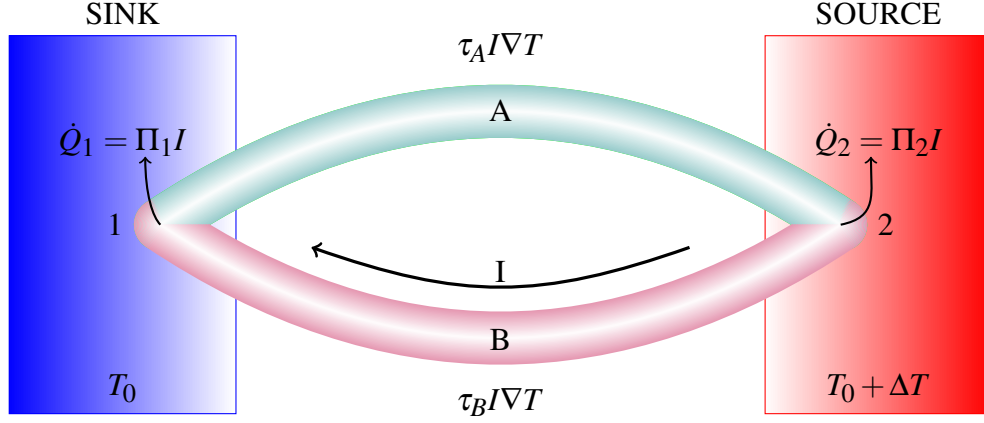
Figure 1.1: Schematic diagram of a simple thermo-couple made of two conductors A and B with junction 1 and 2 kept in a heat sink and heat source respectively. (For interpretation of the references to color in this and all other figures, the reader is referred to the electronic version of this dissertation.)

potential difference generated was found to be independent of the distribution of temperature but proportional to the temperature difference (ΔT) between two junctions[3]

$$V_{AB} = S_{AB}\Delta T, \tag{1.1}$$

where the proportional coefficient S_{AB} is called thermopower or Seebeck coefficient. V_{AB} and S_{AB} are positive if the current flows from A to B at the hot junction. This is the mechanism of a simple thermo-couple as depicted in figure 1.1.

About a decade after Seebeck's discovery, in 1834, the French physicist Jean Charles Athanase Peltier discovered the reverse process when observing that an electrical current could heat or cool the junction of two dissimilar metals.[4] In 1838, Lenz showed that depending on the direction of the electrical current, heat could be removed or added to the junction.[5] The heat being transferred in a unit of time is proportional to the current

$$\dot{Q}_{AB} = \Pi_{AB}I, \tag{1.2}$$

where Π_{AB} is called the Peltier coefficient. Similar to the equation of Seebeck effect, $\dot{Q}_{AB}$ and Π_{AB} are positive if heat is absorbed when the current flows from A to B.

Seebeck-Peltier effects are additive, meaning if there are two junction AB and BC the effective proportionality coefficients of AC is the summation of the former

$$V_{AC} = V_{AB} + V_{BC} = (S_{AB} + S_{BC})\Delta T, \tag{1.3}$$

$$\dot{Q}_{AC} = \dot{Q}_{AB} + \dot{Q}_{BC} = (\Pi_{AB} + \Pi_{BC})I. \tag{1.4}$$

This additive property implies that the the Seebeck(Peltier) coefficient of any pair AB is the difference between absolute Seebeck(Peltier) coefficients, $S(\Pi)$,

$$S_{AB} = S_A - S_B \text{ and } \Pi_{AB} = \Pi_A - \Pi_B. \tag{1.5}$$

These absolute quantities were formulated later by William Thomson (also known as Lord Kelvin).[4] Thomson studied the Seebeck-Peltier effects and discovered a new effect called Thomson effect

$$\dot{Q}_A = \tau_A I \nabla T \tag{1.6}$$

predicting that the rate of heat absorption per unit length of a conductor is proportional to the electrical current I and temperature gradient ∇T. The proportional coefficient τ is called Thomson coefficient. He then derived the relation between the three thermoelectric coefficients by applying the first and second laws of thermodynamics on the thermoelectric circuit. The first law of thermodynamics requires that the work done by the Seebeck potential must equal to the thermal energy absorbed from the surounding

$$V = V_{AB} = V_B - V_A = \Pi_1 - \Pi_2 + \int_{T_0}^{T_0 + \Delta T} (\tau_B - \tau_A) dT \tag{1.7}$$

or

$$dV = d\Pi + (\tau_B - \tau_A) dT. \tag{1.8}$$

This equation is called the first Thomson (or Kelvin) relation. The second law of thermodynamics requires that the total change in entropy must be zero which give us

$$0 = \frac{\Pi_1}{T_0} - \frac{\Pi_2}{T_0 + \Delta T} + \int_{T_0}^{T_0 + \Delta T} \frac{\tau_B - \tau_A}{T} dT. \tag{1.9}$$

3

From (1.8) and (1.9) one gets

$$S = \frac{dV}{dT} = \frac{d\Pi}{dT} + \tau_B - \tau_A \qquad (1.10)$$

$$0 = \frac{d\Pi}{dT} - \frac{\Pi}{T} + \tau_B - \tau_A \qquad (1.11)$$

and obtains the second Thomson relation

$$\Pi = ST \qquad (1.12)$$

Differentiating (1.12) with respect to T and using (1.10), one gets

$$\frac{dS}{dT} = \frac{\tau_A - \tau_B}{T} \qquad (1.13)$$

which give the expression for absolute Seebeck coefficient of A at given T

$$S_A = \int_0^T \frac{\tau_A}{T} dT \qquad (1.14)$$

and the absolute Peltier coefficient of A

$$\Pi_A = T S_A. \qquad (1.15)$$

1.1.2 Mechanisms of thermoelectric effects

Seebeck-Peltier effect involves two physical phenomena: (i) charge-carrier diffusion and (ii) phonon drag. The former occurs when a conductor exposed to a temperature gradient. There is unbalance in hot and cold carrier concentration at the two ends of a conductor, the hot carriers tend to diffuse from the hot end to the cooler one to reach a steady state. The charge-carrier diffusion builds up a net charge at the cold end, giving rise to an electrostatic potential counteracting the chemical potential of the diffusion and brings the system to equilibrium. In the beginning, thermocouple was made of metals, however, more practical approach is using alternative n-type and p-type semiconductors (figure 1.2) connected by metals. In these devices, charges flow through the n-type element, cross the metallic connector and pass into the p-type one, creating a current. The diffusion of charges (and so the mobility and the effective mass of carriers) is affected by scattering. There are two

4
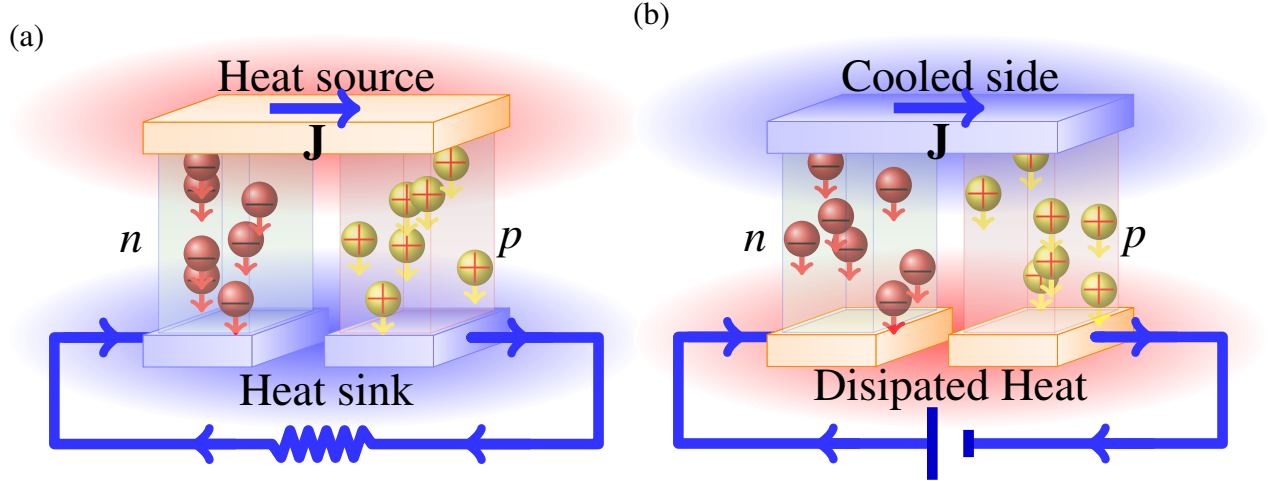
Figure 1.2: Schematics explain (a) the mechanism of Seebeck, temperature gradient drives the movement of carriers, creating a current, and (b) Peltier effects, the current of carriers transfer the heat from cool side to the hot side.

categories of scattering,[6] namely lattice vibrations or phonon and lattice imperfection, hence, the thermopower of a material depends greatly on impurities, imperfections and structural changes.

In addition to charge-carrier diffusion, the latter effect, phonon drag, is found to produce large thermoelectric effects in some semiconductors at low temperature (but not very low temperature).[6] The physics is that in pure system, at low temperature, electron-phonon scattering is predominant. Electrons have a very long relaxation time, and transfer their momentum to phonons in the direction of the electric current. This energy transport contributes to the Peltier heat which may be much larger than the former effect. This happens for

$$T \approx \frac{1}{5}\theta_D,\tag{1.16}$$

where θ_D is the Debye temperature. At higher temperature the phonon-phonon scattering suppresses the phonon-drag effect.

1.1.3 Thermoelectric applications

About 90 per cent of the world's energy is generated by burning fossil fuel, and in the best scenario the ratio of fossil fuel is still about 80 percent by 2035[1]. The efficiency of typical heat engines is about $30 - 40$ percent, leaving more than half of energy lost in form of waste heat. Thermoelectric

devices can convert part of that waste into electricity and greatly improve the operating efficiency of the engines. Moreover, the ability of operating without mechanically moving parts and with very low maintaining requirement makes thermoelectric device greatly promising for a wide range applications. They can fall into two categories: (i) power generation (using Seebeck effect), and (ii) heat pumping or refrigeration (using Peltier effect).

The first commercial thermoelectric generator (TEG), made of ZnSb and constantan in USSR, was dated back to 1948, produced electricity strong enough to power a radio.[7] Since then, the field has been moving much further. Its applications ranges from big space missions[8–10] to micropower harvesting.[11]

The thermoelectric module called Radioisotope Thermoelectric Generator (RTG) has played a key role in many missions of the United States National Aeronautics and Space Administration (NASA). The first use of RTGs was in the spacecraft "Transit 4A" launched in 1961 and then in many other missions after. Recently an eighth RTG configuration, called the Multi-Mission Radioisotope Thermoelectric Generator (MMRTG), has recently been used on the Mars Science Laboratory rover, Curiosity. RTGs use radioactive isotope plutonium-238 decay as the heat source and are preferable over other types of power generators because of its (i) *long life time* which suitable a long mission in the deep space, (ii) ability to operate in an *extreme environment* such as the high-radiation belts of Jupiter, extreme temperature on moon, or dust storm on Mars, (iii) *operational independence* which guarantees to providing needed power regardless of the spacecraft position or orientation and (iv) its reliability which has been proven to run for decades.

The most active area of thermoelectric application is in the automotive industry. Both major automotive companies have thermoeletric development programs.[12] It is estimated that in a vehicle using internal combustion engine, only 25 percent of provided energy is used to move it, 75 percent is just wasted, in which about 40 percent can be used for a thermoelectric power generator.[12] TEG can use the wasted heat to recharge the battery. This can help to reduce or even eliminate the need for alternator, and as a result reduce the load on the engine, therefore, improve fuel efficiency by the order of 10 percent.[11] Similar applications can be used in any
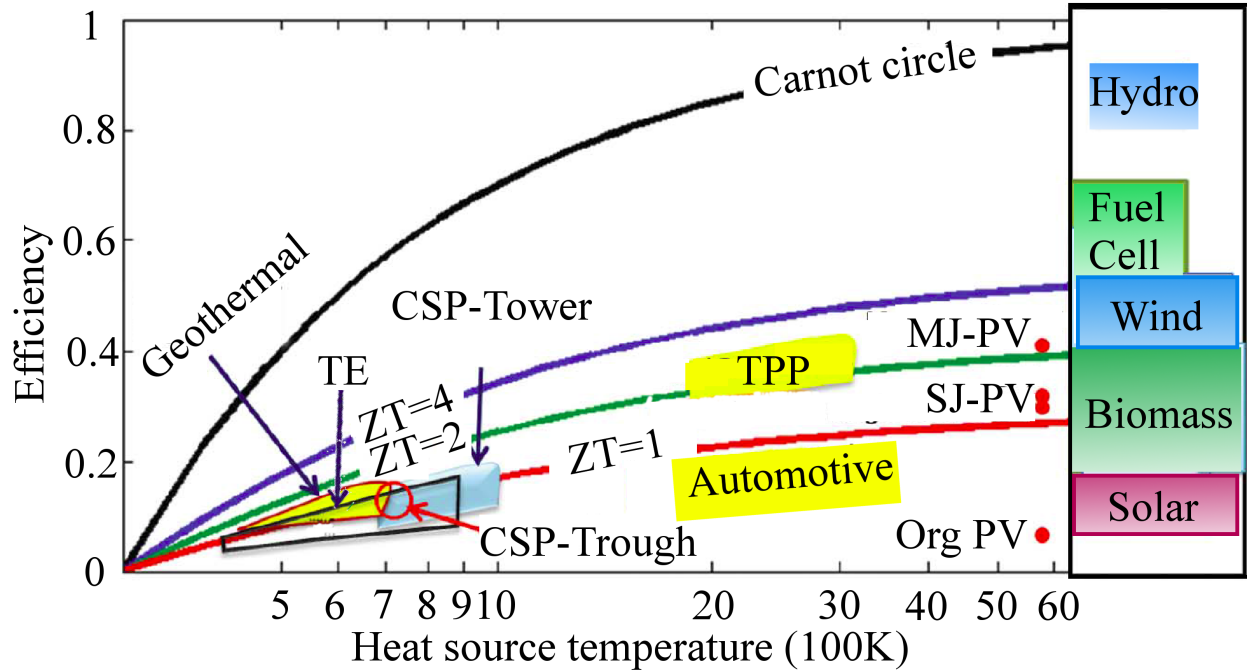
Figure 1.3: (Source: Zebarjadi et al. [14]) Power generation efficiency versus temperature of the hot side, plotted for different energy conversion technologies. The cold side is assumed to be at room temperature. The efficiency range of some of the other renewable energy technologies is marked in a bar on the right-hand side of the graph. In this graph PV is photovoltaic; CSP denotes concentrated solar power; SJ and MJ denotes single- and multiple-junction; and Org, TE, and TPP denote organic, thermoelectric and thermionic devices, and thermal power plan respectively.

thermal power plan to recover wasted heat.

Along with the development of science and technology, small and portable applications need power sources smaller and lighter than conventional batteries. A TEG using combustible fuel could be a promising substitution. There is, however, one big challenge that it needs at least 500°C in order to reach desired efficiency.[11] Going to much smaller in size, TEG proves its strength since other types are not scalable or at lease have much lower efficiency.[13] At small scale, TEG can havest very small amount of heat for low power applications, such as wireless sensor networks, mobile devices or medical applications.[11]

Despite the low efficiency in current thermoelectrics ($< 10\%$), thanks to its unique properties such as having no mechanical moving parts, fluid or refrigerants, flexible shape (they can be very small), long life time and controllable, TE cooler and heater (heat pump) become common in daily
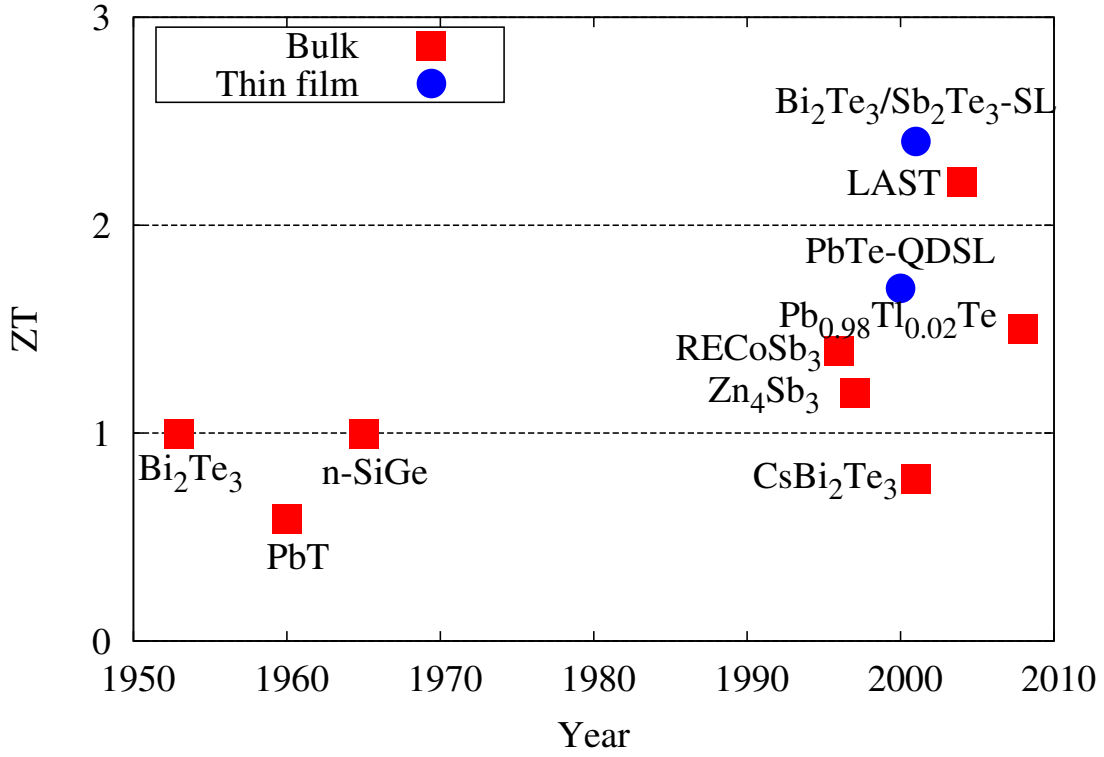
Figure 1.4: (Source: Tritt [15]) *ZT* of several TE materials and year of their discovery, showing how *ZT* or materials have been improved.

life.[14] Such applications include portable mini cooler, refrigerator, coffee warmer. Thermoelectric heat pumps are also found in temperature/weather control devices such as cooled seat, weather vest, temperature regulators of semiconductor lasers, and medical.[14] However, for large scale applications involving higher powers, one need to develop (or discover) thermoelectrics with higher efficiency ($\sim 20\%$). This is the driving force behind current research in novel thermoelectrics.

1.1.4 Figure of merit and device efficiency

The maximum efficiency that any thermal process can have is the Carnot efficiency η_c of an adiabatic circle. The efficiency of a TE device, usually referred as coefficient of performance (COP), is given by

$$COP = \eta_c \times M, \tag{1.17}$$

where M is the merit factor which is positive and smaller than unity. COPs are different for the refrigerator and the power generator. This thesis is concerned mainly with the latter for which the COP is given by

$$\text{COP}_G = \eta_c \times M = \frac{\Delta T}{T_h} \times \frac{\sqrt{1+ZT}-1}{\sqrt{1+ZT}+T_c/T_h}, \tag{1.18}$$

where T_h, T_c, and ΔT are temperatures of the hot (heat source) and the cold (heat sink) ends, and the difference between them respectively, $T = 1/2(T_h + T_c)$ is the operating temperature. The figure of merit Z is given by

$$Z = \frac{1}{T}\frac{S^2\sigma}{\kappa}, \tag{1.19}$$

in which σ and κ are the electrical and thermal conductivity respectively and S is thermopower (Seebeck coefficient). One often refers to ZT as the dimensionless figure of merit. Note that ZT depends only on properties of materials such as S, σ, and κ. The larger the ZT, the higher is the efficiency. The relation between efficiency and temperature for different ZT is given in figure 1.3. For comparison, the efficiency of other energy sources and their temperature range is also given in the same figure. In automotive industry, the state of thermoelectric is currently at the first generation of thermoelectric module with ZT=1 and the second generation with ZT=2 is under progress.[16] To make thermoelectric applications economically viable, we need ZT of $\sim$3. Even though, there is, in principle, no upper limit of ZT, obtaining high ZT, however, is not an easy job. The history of thermoelectrics reveals that for almost a century after the Seebeck's discovery of thermoelectric effect, ZT barely reached unity (figure 1.4). It is during the last few decades that the thermoelectric research has come with some break through ideas and new directions which can improve ZT up to $\sim$ 2.5. According to equation 1.19, a good thermoelectric material needs (i) large Seebeck coefficient, (ii) high electrical conductivity, and (iii) low thermal conductivity. The difficulty in designing high ZT materials is the conflicting requirements of properties. An example of this competing relation is given for a homogeneous conductor as followings.

(i) In order to get large Seebeck coefficient, which, for homogeneous conductor, is given by[17]

$$S = \frac{8\pi^2 k_B^2}{2eh^2}m^*T\left(\frac{\pi}{3n}\right)^{2/3}, \tag{1.20}$$
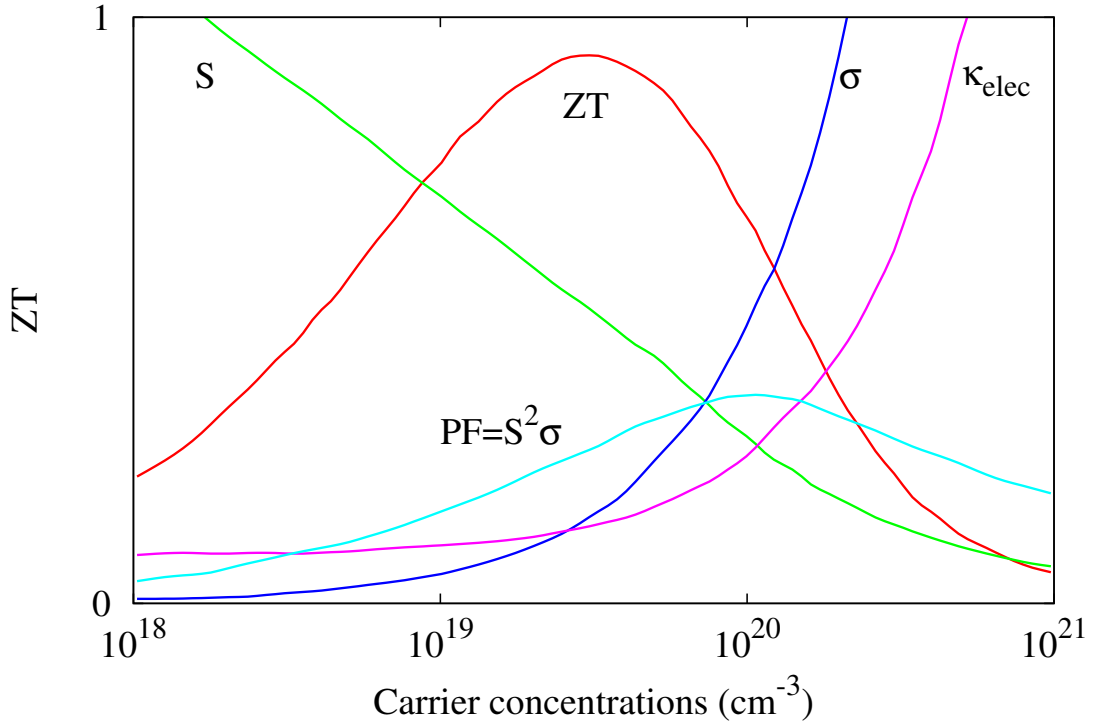
Figure 1.5: Competing relation between S, σ, and κ

where k_B and h are the Boltzmann, Planck constants respectively, one needs a low carrier concentration n with large effective mass m^*, or low carrier mobility μ.

(ii) On the other hand, a high electrical conductivity requires large n and high μ since

$$\sigma = ne\mu, \tag{1.21}$$

where e is the charge of the carriers.

(iii) The electronic part of the thermal conductivity can be related to electrical conductivity by Wiedemann-Franz law

$$\kappa = \kappa_{latt} + \kappa_{elec} \tag{1.22}$$

$$= \kappa_{latt} + LT\sigma = \kappa_{latt} + LTne\mu, \tag{1.23}$$
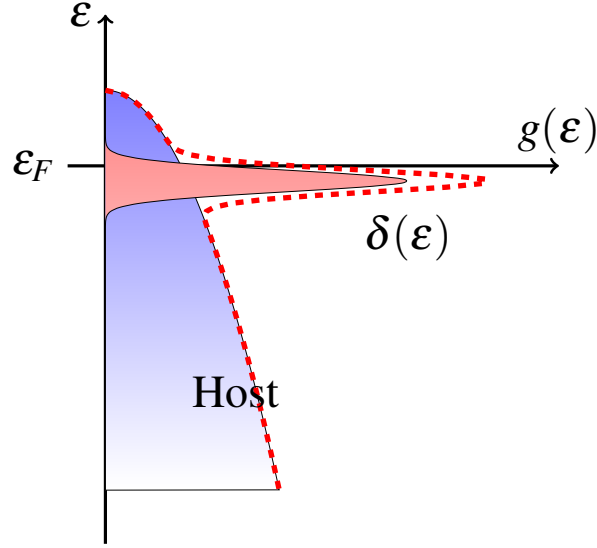
Figure 1.6: Schematic diagram of the density of state of a material with a delta function defect state.

where κ_{latt} and κ_{elec} are thermal conductivities due to lattice vibrations (phonons) and electrons, and L is Lorentz number. It means in order to get low thermal conductivity one needs small n and μ.

This conflicting relation is demonstrated in figure 1.5. Hence, a large ZT could be only found with optimized value of S, σ, and κ, which is a challenging problem. It turns out that semiconductors with small band gaps ($\sim$0.2–0.5 eV) or pseudo-gap systems are the best candidates for thermoelectric applications at room temperature.[18] For a brief discussion of semiconductors and pseudo-gap systems see section 1.3.

1.2   Theoretical aid in pursuing better figure of merit (ZT)

Extensive works have been done in trying to maximize the magnitude of ZT. Approaches to improve the performance of TE materials can be categorized into two types: (i) engineering electronic structures to optimize S,σ and κ_{elec}, and (ii) engineering phonons to minimize κ_{latt}. Following the first approach (engineering electronic structures), Mahan and Sofo [17] on their quest to "The

best thermoelectric" predicted that the enhancement of S can be achieved in a system where exist a rapid change in the density of states $g(\varepsilon)$ near the Fermi level. This prediction can be easily understood using the Mott's formula for thermopower which is given by

$$
\begin{aligned}
S &= \frac{\pi^2}{3}\frac{k_B}{q}k_B T \left\{ \frac{d[ln(\sigma(\varepsilon))]}{d\varepsilon} \right\}_{\varepsilon=\varepsilon_F} \\
&= \frac{\pi^2}{3}\frac{k_B}{q}k_B T \left\{ \frac{1}{n}\frac{dn(\varepsilon)}{d\varepsilon} + \frac{1}{\mu}\frac{d\mu(\varepsilon)}{d\varepsilon} \right\}_{\varepsilon=\varepsilon_F},
\end{aligned} \tag{1.24}
$$

where $n(\varepsilon) = g(\varepsilon)f(\varepsilon)$ is the carrier density, $f(\varepsilon) = 1/(Exp[(\varepsilon - \mu)/k_B T]$ is the Fermi function, $\mu(\varepsilon)$ is carrier's mobility at energy ε, and ε_F is the Fermi level. The Mott's equation predicts that large S can be obtained when DOS (the first term in the bracket of Eqn. 1.24) or carrier's mobility (the second term in the bracket of Eqn. 1.24) varies rapidly at the Fermi level. One approach on this direction is to find a material with a rapidly-varying region in DOS which is accessible by doping. An example for this approach is the Heusler compoud Fe_2VAl[19], which has a steep DOS near the band edge. Chapter 3 will be dedicated for discussing the electronic and thermoelectric properties of this system. Another approach to achieve a large change of DOS in a small range of energy is to introduce a delta (resonant) states into the electronics structure of the host materials (Fig. 1.6). This approach has been quite successful in improvement of ZT. For example, in the classic thermoelectric material PbTe, theoretical calculations by Ahmad et al. [20] (2006) predicted that doping of group III elements (Ga, In, Tl) creates resonant levels. Heremans et al. [21] later reported a large enhancement of ZT in Tl-doped PbTe whose $ZT = 1.5$ was found at 700 K compared to $ZT = 0.7$ for the host material PbTe.

Another effect which possibly improves thermoelectric performance and can be achieved by engineering electronic structure is energy filtering. Detailed discussions of this effect can be found in reference [22] and [14], and references therein. This effect can enhance the performance of thermoelectric materials by blocking low-energy electron, and thus increase the average heat transfer by an electron. This effect can be achieved by nanostructure inclusion in the host materials. An exciting example of this approach is the work on Half-Heusler–(Full) Heusler nanocomposites initiated by Makongo et al. [23] who reported a significant improvement of the powerfactor by $\sim 25\%$.

I will discuss more about this system in chapter 5 of this thesis.

Engineering phonons approach to lower the thermal conductivity of thermoelectric materials was considered as early as 1974 by Rowe [24], and later by Slack and Hussain [25]. Following this path, one looks for materials with complex structures and/or with large number of atoms per unitcell since the thermal conductivity is predicted to be inversely proportional to the number of atoms per unitcell[26]. This is the rationale for studying some of materials discussed in chapter 4 of this thesis. Recently, Skoug et al. [27], Zhang et al. [28] brought back the important relation between lone-pair electrons and the aharmonicity of phonon spectrum of materials. Zhang et al. calculated the phonon spectrum and suggested that lone-pair electrons created arharmonicity of and softened phonon modes, producing large Grüneisen parameter, and thus lowing thermal conductivity due to phonon-phonon scattering. Chapter 4 will discuss more on this mater for tetrahedrally bonded compounds.

1.3 Narrow band gap semiconductors and pseudo-gap systems

The area of semiconductor is one of the fastest developing fields in both science, technology and industry which totally change the life of the mankind. The first production of semiconductor transistor was announced just sixty years ago. Nowadays, it involves virtually every thing around us from simple daily task to the way we communicate and work. It is hard to imagine how the world would turn out to be if not for the development of semiconductor. The first recorded observation of semiconductor dates back to 1833 when Michael Faraday reported that the electrical conductivity of sulphurette of silver (silver sulfide) increases with increasing of temperature[29] which he thought to be related to the tension. The properties of semiconductor came to be understood about a century later, thanks to the quantum mechanics study by Wilson in 1931.[30] Semiconductor is now known to have a forbidden gap in the energy spectrum, in which the electronic states are not allowed to exist. The increase in the conductivity of a semiconductor with increasing temperature is known to be due to the excited electrical carriers when electrons jump from the valence bands to the conduction bands. There is a thin line that distinguishes semiconductor from insulator
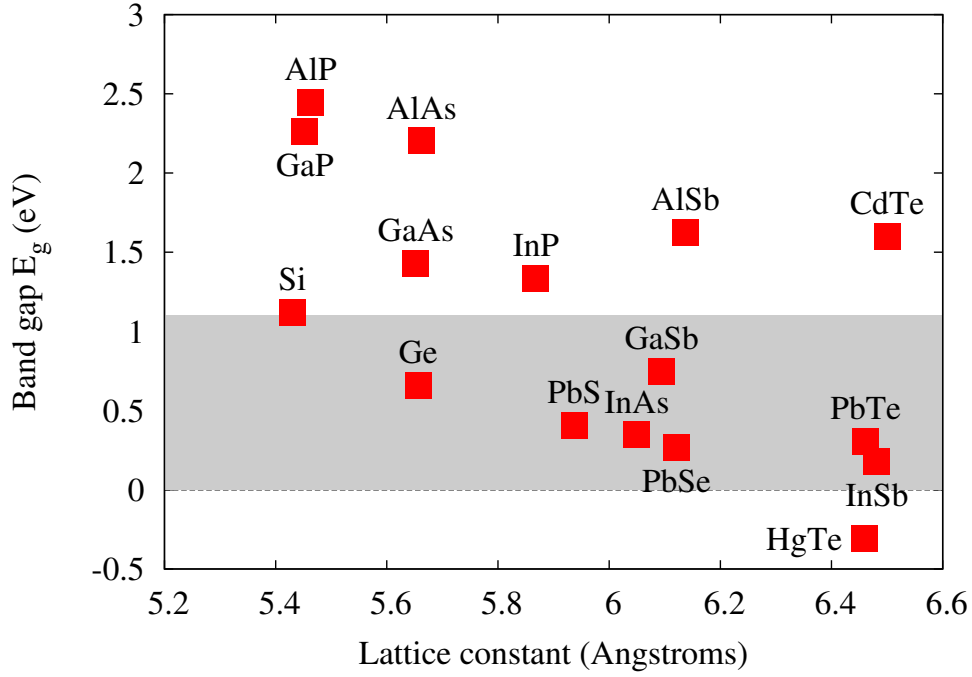
Figure 1.7: (Source: Lin and Kuo [31]) Band gap of several typical semiconductors. The shade indicates the range of narrow-band-gap semiconductors.

since both have a forbidden band gap in the electronic structure. The gap of semiconductor is usually smaller than that of insulator ($\sim$5.5 eV for diamond) so that the excitation occurs at ordinary temperatures. Figure 1.7 shows values of band gap for several well-known semiconductors.

A vast amount of work has been devoted to the understanding of semiconductor or related effects, covering from fundamental physics to technological application. Many aspects of semiconductor have been revealed and many more are being explored. Examples of the applications and interesting phenomena in semiconductors can be found in overwhelming numbers of publications in the literature, including, but not limit to, thermoelectrics, spintronics, electronics, etc. . Recently, a new phenomenon that has attracted a lot of attention lately is in the field of topological insulator (TI) discovered in 2005.[32]. Except for its misleading name, TIs are small band gap semiconductors with topologically protected surface states. In this thesis, I only deal with semiconductors for thermoelectric applications.

Semiconductors can be classified into two categories, direct and indirect band gap. In direct-
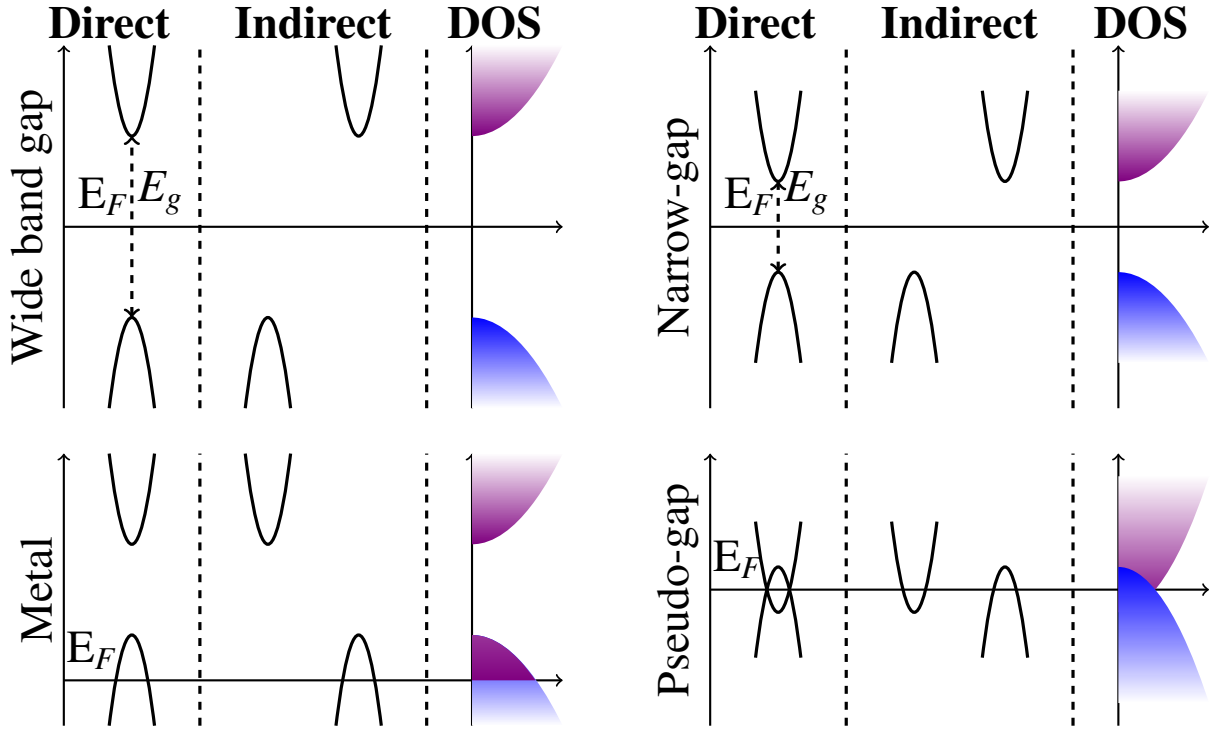
Figure 1.8: Diagram explaining different scheme of band gap in a semiconductor.

band-gap semiconductors (for example, GaAS, InP, GaN, etc), the lowest of the conduction bands and the highest of valence bands occur at the same symmetric point in the first Brillouin Zone (IBZ), whereas in indirect-band-gap semiconductors, they occur at different symmetric points (see Fig. 1.8). Another way to classify semiconductors is based on the magnitudes of their band gaps, one has either large-band-gap, narrow-band-gap or pseudo-gap semiconductors. A diagram demonstrate the different types of band gap in semiconductor is given in figure 1.8. The definition of narrow-gap semiconductor is not quite strict. Since the history of narrow-band-gap semiconductors (NBGS) came along with its application in infrared emitting and detecting, usually NBGS is limited to those with the band gap (E_g) corresponding to an infrared absorption cut-off wavelength over $2\mu m$ ($\sim$0.6 eV).[33] However, one could also refer to NBGS as those having band gap smaller than that of silicon ($\sim$1.1 eV). The renewed interest in NBGS for its potential thermoelectric application was inspired by the works of Mahan and Sofo in from 1989–1994[18, 34] who suggested that NBGS are the best candidates for TE application. Beside NGBS, pseudo-gap

materials are also interesting systems which can be used in thermoelectric applications. Pseudo-gap materials have an overlap between conduction bands and valence bands, giving rise to a small but finite density of states at the Fermi level. Our group at Michigan State University has been working extensively on the branch of narrow-band-gap (NBGS) and pseudo-gap semiconductors with the focus on their thermoelectric (TE) application (an introduction on thermoelectrics is given in section 1.1). We have been working on a wide range of materials including well known NBGS such as BiTe, BiSe, SbTe, $AgPb_mSbTe_{m+2}$ (LAST), III-VI compounds, Mg_2Si, Cu_3SbSe_4, etc.

1.4   Outline of the dissertation

In this dissertation, I have used first principle calculations using density functional theory (DFT), which is discussed in chapter 2, and reported the results of my works done in the last several years on the electronic and thermoelectric properties of selected NBGS including Heusler compounds (mainly Fe_2VAl), tetrahedrally bonded I_3-V-VI_4 chalcogenides (I = Cu, V = P, As, Sb, and Bi, and VI = S, Se, and Te), and $ZrNiSn$-$ZrNi_2Sn$ mixture.

The results can be divided into two parts: the first part includes chapter 3 and 4, and the second part includes chapter 5. The first part focuses on understanding the fundamental properties of Heusler compound Fe_2VAl and the tetrahedrally coordinated compounds. I address the questions about the band gap of these materials using different levels of approximation in DFT and study their thermoelectric properties using Boltzmann's transport equation. Most of the works in this part have been published in references [35], [36], and [37]. The second part dedicates for studying the formation of the Heusler phase nanostructures in the Half-Heusler matrix or vice versa, and analyzing their electronic structures with a discussion on how they can affect the thermoelectric properties of these materials.

In chapter 6, I will summarize my findings and propose some further works.

Electronic structure plays a key role in understanding physical properties of materials, in particular, their thermoelectric properties. The methods of calculating electronic structure, especially the Density functional theory (DFT), have developed rapidly during the last quarter of the last century, due to the development of computing techniques and the power of modern computers. There is a large selection of available DFT-based computational codes (programs) which can be easily used to calculate electronic structure of materials. DFT has become the most successful tool in studying physical properties materials. Even though DFT is an exact theory, all the calculations are done using, at least, some approximations. Each approximation is suitable for some specific cases, thus, it is very important to understand the theoretical basis behind these calculations and their limitations. In this chapter I shall review some of the fundamentals of electronic structure theory, focusing on DFT, and discuss several approximations to it. The Boltzmann's transport equation will also be discussed as a bridge connecting calculated electronic structure to the thermoelectric (transport) properties of a material.

Some of the contents of this chapter follow the spirit of the "Electronic Structure: Basic Theory and Practical Methods" by Martin [38].

2.1 Basic equations

Electronic structure, following the discovery of electrons in the late 1800s, is the concept used for the electron configuration, or the arrangement of electrons in atoms, molecules, and solids. Theory of electronic structure is a combination of quantum mechanics and statistical physics.

The problem of dealing with a realistic electron system is that it is a many-body system. In order to understand the behavior of such electrons, one has to start with the Hamiltonian for electrons

and nuclei,

$$\hat{H} = -\frac{\hbar^2}{2m_e} \sum_i \nabla_i^2 - \sum_{i,I} \frac{Z_I e^2}{|\mathbf{r}_i - \mathbf{R}_I|} + \frac{1}{2} \sum_{i \neq j} \frac{e^2}{|\mathbf{r}_i - \mathbf{r}_j|} - \sum_I \frac{\hbar^2}{2M_I} \nabla_I^2 + \frac{1}{2} \sum_{I \neq J} \frac{Z_I Z_J e^2}{|\mathbf{R}_I - \mathbf{R}_J|}, \quad (2.1)$$

where electrons, with charge e and mass m_e, are denoted by lower case subscripts, and nuclei, with charge Z_I and mass M_I, are denoted by upper case subscripts. For simplicity, we adopt the Hartree atomic units where $\hbar = m_e = 4\pi/\varepsilon_0 = 1$. Using the Born-Oppenheimer approximation[38], one can neglect the kinetic energy of nuclei and rewrites the Hamiltonian as

$$\hat{H} = \hat{T} + \hat{V}_{ext} + \hat{V}_{int} + E_{II}, \quad (2.2)$$

where the electron kinetic energy is

$$\hat{T} = -\frac{1}{2} \sum_i \nabla_i^2, \quad (2.3)$$

$\hat{V}_{ext}$ is the potential due to the nuclei, given by

$$\hat{V}_{ext} = \sum_{i,I} V_I(|\mathbf{r}_i - \mathbf{R}_i|) = \sum_{i,I} \frac{Z_I}{|\mathbf{r}_i - \mathbf{R}_i|}, \quad (2.4)$$

$\hat{V}_{int}$ is the electron-electron interaction,

$$\hat{V}_{int} = \frac{1}{2} \sum_{i \neq j} \frac{1}{|\mathbf{r}_i - \mathbf{r}_j|}, \quad (2.5)$$

and E_{II} is the interaction between static nuclei. In general, E_{II} can include other terms that contribute to the total energy but does not directly affect the electronic behavior. Also, E_{ext} can have other "external potentials" acting on electrons, for instance, electric fields, magnetic fields, etc.

The wavefuntions describing electrons is the solution of the time-dependent Schrödinger equation

$$i\hbar \frac{d\Psi(\{\mathbf{r}_i\};t)}{dt} = \hat{H}\Psi(\{\mathbf{r}_i\};t), \quad (2.6)$$

where the many-body state Ψ is a function of electron position $\mathbf{r}_i$ and time t. It is noted that the spin subscript is omitted and assumed to be included in the coordinate $\mathbf{r}_i$. The wavefunction can be written as $\Psi(\{r_i\};t) = \Psi(\{\mathbf{r}_i\})e^{-iEt}$, and it also satisfies the time-independent Schrödinger equation

$$\hat{H}|\Psi\rangle = E|\Psi\rangle, \quad (2.7)$$

where E is the energy associated with an eigenstate $|\Psi\rangle$. The ground state wavefunction Ψ_0 is the state with the lowest energy and can be determined by minimizing the total energy with respect to parameters appearing in $|\Psi\rangle$.

The time-independent expression for an observable is given by the expectation value of the corresponding operator $\hat{O}$,

$$\langle \hat{O} \rangle = \frac{\langle \Psi | \hat{O} | \Psi \rangle}{\langle \Psi | \Psi \rangle}. \tag{2.8}$$

Applying this equation to the density operator $\hat{n}(\mathbf{r}) = \sum_{i=1,N} \delta(\mathbf{r} - \mathbf{r}_i)$, one gets an important quantity in the electronic structure theory, the density of particles,

$$n(\mathbf{r}) = \frac{\langle \Psi | \hat{n} | \Psi \rangle}{\langle \Psi | \Psi \rangle} = N \frac{\int d^3 r_2 \cdots d^3 r_N \sum_{\sigma_1} |\Psi(\mathbf{r}, \mathbf{r}_2, \mathbf{r}_3, ..., \mathbf{r}_N)|^2}{\int d^3 r_1, d^3 r_2 \cdots d^3 r_N |\Psi(\mathbf{r}_1, \mathbf{r}_2, \mathbf{r}_3, ..., \mathbf{r}_N)|^2}, \tag{2.9}$$

where N is the total number of electrons, σ_1 is the spin index associated with $\mathbf{r}$. The integral form of the density is obtained by tracing over all variables, taking into account the symmetry of wavefunction over electron positions. If the σ_1 index is omitted, one gets the density of one spin-component. Similarly, the total energy of the system is obtained by calculating the expectation value of the Hamiltonian,

$$E = \frac{\langle \Psi | \hat{H} | \Psi \rangle}{\langle \Psi | \Psi \rangle} = \langle \hat{T} \rangle + \langle \hat{V}_{int} \rangle + \int d^3 r V_{ext}(\mathbf{r}) n(\mathbf{r}) + E_{II}, \tag{2.10}$$

It is convenient to organize the terms in the energy into charge-neutral groups,

$$E = \langle \hat{T} \rangle + \left(\langle \hat{V}_{int} \rangle - E_{Hartree} \right) + E^{CC}, \tag{2.11}$$

where

$$E_{Hartree} = \frac{1}{2} \int d^3 r d^3 r' \frac{n(\mathbf{r})n(\mathbf{r}')}{|\mathbf{r} - \mathbf{r}'|}, \tag{2.12}$$

is the self-interaction energy of the density $n(\mathbf{r})$ treated as a classical charge density, and

$$E^{CC} = E_{Hartree} + \int d^3 r V_{ext}(\mathbf{r}) n(\mathbf{r}) + E_{II}, \tag{2.13}$$

is the classical Coulomb energy. The middle term in 2.11, $\langle \hat{V}_{int} \rangle - E_{Hartree}$, is the difference between the Coulomb energies of interacting, correlated electrons with density $n(\mathbf{r})$ and that of a

continuous classical charge distribution having the same density. This term defines the exchange-correlation energy, E_{xc}, which is an essential and perhaps the most problematic part in DFT. A discussion of this term is the central focus of this chapter. It is noted that all the Coulomb and Hartree terms are long-range interactions, whereas the exchange-correlation term is short-range, since the long-range part is canceled in the difference.

2.2 Independent-electron – Hartree and Hartree-Fock approximation

It is impossible to solve the Schrödinger equation exactly, especially for a large many-electron system. It is important to find an effective approximation. One approximation which is used extensively till today is the independent-electron approximation (mean-field theory). This approximation assumes that the electrons are uncorrelated except that they follow the exclusion principle and an electron moves in an average potential provided by the others. There are two basic approaches which characterize independent-electron approximation, they are Hartree, and Hartree-Fock approximations.

2.2.1 Hartree approximation

In the Hartree approximation, the effective potential includes the effect of real interactions in a averaging way but does not include the Pauli principle explicitly in the wavefunction (Fermion antisymmetry). The many-electron wavefunction can be considered as a multiple of the single-particle wavefunctions,

$$\Psi(\{\mathbf{r}_i\}) = \prod_{i=1}^{N} \psi_i(\mathbf{r}_i),$$ (2.14)

where N is the number of electrons. The many-body problem, thus, becomes an effective single-electron equation,

$$\hat{H}_{eff}\psi_i^{\sigma}(\mathbf{r}) = \left[-\frac{1}{2}\nabla^2 + V_{eff}^{\sigma}(\mathbf{r})\right]\psi_i^{\sigma}(\mathbf{r}) = \varepsilon_i^{\sigma}\psi_i^{\sigma},$$ (2.15)

where $V_{eff}^{\sigma}(\mathbf{r})$ is an effective potential acting on electrons of spin σ and position $\mathbf{r}$. The ground state for many non-interacting electrons is obtained by filling the lowest eigenstates obeying the

exclusion principle. The use of this approximation is the core of DFT which will be discussed later in this chapter.

At finite temperature, it is straight forward to apply statistical mechanics of non-interacting fermions, with the Fermi-Dirac equilibrium distribution of electron,

$$f(\varepsilon_i^{\sigma}) = \frac{1}{e^{\beta(\varepsilon_i^{\sigma} - \mu)} + 1}, \tag{2.16}$$

where μ is the chemical potential of the electrons. One can get the total energy by weighted sum of the eigenvalues of 2.15

$$E(T) = \langle \hat{H} \rangle = \sum_{i,\sigma} f(\varepsilon_i^{\sigma}) \varepsilon_i^{\sigma} \tag{2.17}$$

And the one-electron density operator can be defined as

$$\hat{\rho} = \sum_i |\psi_i^{\sigma}\rangle f_i^{\sigma} \langle \psi_i^{\sigma}|, \tag{2.18}$$

and one can get the density matrix for explicit spin and position representation,

$$\rho(\mathbf{r}, \sigma; \mathbf{r}', \sigma') = \delta_{\sigma, \sigma'} \sum_i \psi_i^{\sigma*}(\mathbf{r}) f(\varepsilon_i^{\sigma}) \psi_i^{\sigma}(\mathbf{r}'), \tag{2.19}$$

the diagonal part gives the electron density,

$$n^{\sigma}(\mathbf{r}) = \rho(\mathbf{r}, \sigma; \mathbf{r}, \sigma) = \sum_i f(\varepsilon_i^{\sigma}) \left| \psi_i^{\sigma}(\mathbf{r}) \right|^2. \tag{2.20}$$

An example of the simplest model system in condensed matter is the homogeneous electron gas. In this model the nuclei are replaced by a uniform positive charge. The system is specified by its density $n = N/\Omega$, which can be characterized by the parameter r_s such that

$$\frac{4\pi}{3} r_s^3 = \Omega/N = \frac{1}{n}. \tag{2.21}$$

The Hamiltonian for this system is given by

$$\hat{H} = -\frac{1}{2} \sum_i \nabla_i^2 + \frac{1}{2} \left[\sum_{i \neq j} \frac{1}{|\mathbf{r}_i - \mathbf{r}_j|} - \int d^3 r d^3 r' \frac{n^2}{|\mathbf{r} - \mathbf{r}'|} \right] \tag{2.22}$$

which can be rewritten in terms of $\tilde{\mathbf{r}} = \mathbf{r}/r_s$ as

$$\hat{H} = \left(\frac{a_0}{r_s} \right)^2 \sum_i \left[-\frac{1}{2} \tilde{\nabla}_i^2 + \frac{1}{2} \frac{r_s}{a_0} \left(\sum_{j \neq i} \frac{1}{|\tilde{\mathbf{r}}_i - \tilde{\mathbf{r}}_j|} - \frac{3}{4\pi} \int d^2 \tilde{\mathbf{r}} \frac{1}{|\tilde{\mathbf{r}}|} \right) \right], \tag{2.23}$$

where a_0 is the first Bohr radius. This expression shows that the properties of a system with the density r_s/a_0 are equivalent to a system at fixed density but with scaled electron-electron interaction $e^2 \to (r_s/a_0)e^2$.

Applying the non-interacting approximation, the solutions of the Schrödinger equation are normalized plane waves $\psi_k = (\frac{1}{\Omega^{1/2}})e^{i\mathbf{k}\cdot\mathbf{r}}$ with energy $\varepsilon_{\mathbf{k}} = \frac{1}{2}k^2$, where $\mathbf{k}$ is the wavevector. The density for each spin can be found

$$\rho(\mathbf{r},\mathbf{r}') = \rho(|\mathbf{r}-\mathbf{r}'|) = \frac{1}{(2\pi)^3}\int d\mathbf{k} f(\varepsilon_{\mathbf{k}})e^{i\mathbf{k}\cdot(\mathbf{r}-\mathbf{r}')} \tag{2.24}$$

using $r = |\mathbf{r}-\mathbf{r}'|$ one finds

$$\rho(r) = \frac{k_F^3}{e\pi^2}\left[3\frac{\sin(k_F r)-k_F r\cos(k_F r)}{(k_F r)^3}\right], \tag{2.25}$$

where k_F is the Fermi wavevector given by

$$\frac{4\pi}{3}(k_F)^3 = \frac{(2\pi)^3}{\Omega}N. \tag{2.26}$$

2.2.2 Hartree-Fock approximation (HFA)

In the Hartree-Fock approach, one starts from a properly antisymmetrized determinant wavefunction (satisfying Fermi statistics) with fixed number of electrons, N, and finds the single determinant that minimizes the total energy for the full interacting Hamiltonian. In the absence of spin-orbit interaction, the determinant wavefunction can be written as

$$\Psi(\{\mathbf{r}_i,\sigma_i\}) = \frac{1}{(N!)^{1/2}}\begin{vmatrix} \phi_1(\mathbf{r}_1,\sigma_1) & \phi_1(\mathbf{r}_2,\sigma_2) & \cdots & \phi_1(\mathbf{r}_N,\sigma_N) \\ \phi_2(\mathbf{r}_1,\sigma_1) & \phi_2(\mathbf{r}_2,\sigma_2) & \cdots & \phi_2(\mathbf{r}_N,\sigma_N) \\ \vdots & \vdots & \ddots & \vdots \\ \phi_N(\mathbf{r}_1,\sigma_1) & \phi_N(\mathbf{r}_2,\sigma_2) & \cdots & \phi_N(\mathbf{r}_N,\sigma_N) \end{vmatrix}, \tag{2.27}$$

where $\phi_i(\mathbf{r}_i, \sigma_i) = \psi_i^\sigma(\mathbf{r}_j)\alpha_i(\sigma_j)$, $\alpha_i(\sigma_i)$ is the spin eigenstate. The expectation value of the Hamiltonian is given by

$$
\begin{aligned}
\langle\Psi|\hat{H}|\Psi\rangle = &\sum_{i,\sigma}\int d\mathbf{r}\,\psi_i^{\sigma*}(\mathbf{r})\left[-\frac{1}{2}\nabla^2 + V_{ext}(\mathbf{r})\right]\psi_i^\sigma(\mathbf{r}) + E_{II} \\
&+\frac{1}{2}\sum_{i,j,\sigma_i,\sigma_j}\int d\mathbf{r}d\mathbf{r}'\,\psi_i^{\sigma_i*}(\mathbf{r})\psi_j^{\sigma_j*}(\mathbf{r}')\frac{1}{|\mathbf{r}-\mathbf{r}'|}\psi_i^{\sigma_i}(\mathbf{r})\psi_j^{\sigma_j}(\mathbf{r}') \\
&-\frac{1}{2}\sum_{i,j,\sigma}\int d\mathbf{r}d\mathbf{r}'\,\psi_i^{\sigma*}(\mathbf{r})\psi_j^{\sigma*}(\mathbf{r}')\frac{1}{|\mathbf{r}-\mathbf{r}'|}\psi_j^\sigma(\mathbf{r})\psi_i^\sigma(\mathbf{r}'),
\end{aligned}
\tag{2.28}
$$

where the first term is the sum over the one-body expectation values, the second term is the interaction energy between ions which can be neglected as discussed earlier, the third term is the direct or Hartree energy, the forth term is the exchange or the Fock part. The Hamiltonian includes unphysical self-interaction energy ($i = j, \sigma_i = \sigma_j$), however, they are canceled between the Hartree and the Fock terms. The exchange potential exists only between electrons with same spins and is non-local, making it more difficult to calculate. Variation of $\psi_i^{\sigma*}(\mathbf{r})$ then leads to the Hartree-Fock equation

$$
\begin{aligned}
\left[-\frac{1}{2}\nabla^2 + V_{ext}(\mathbf{r}) + \sum_{j,\sigma_j}\int d\mathbf{r}'\,\psi_j^{\sigma_j*}(\mathbf{r}')\psi_j^{\sigma_j}(\mathbf{r}')\frac{1}{|\mathbf{r}-\mathbf{r}'|}\right]\psi_i^\sigma(\mathbf{r}) \\
-\sum_j\int d\mathbf{r}'\,\psi_j^{\sigma*}(\mathbf{r}')\psi_i^\sigma(\mathbf{r}')\frac{1}{|\mathbf{r}-\mathbf{r}'|}\psi_j^\sigma(\mathbf{r}) = \varepsilon_i^\sigma\psi_i^\sigma(\mathbf{r}).
\end{aligned}
\tag{2.29}
$$

This equation can be written as

$$
\hat{H}_{eff}^i\psi_i^\sigma(\mathbf{r}) = \left[-\frac{1}{2}\nabla^2 + \hat{V}_{eff}^{i,\sigma}(\mathbf{r})\right]\psi_i^\sigma(\mathbf{r}) = \varepsilon_i^\sigma(\mathbf{r}),
\tag{2.30}
$$

where

$$
\hat{V}_{eff}^{i,\sigma}(\mathbf{r}) = V_{ext}(\mathbf{r}) + V_{Hartree}(\mathbf{r}) + \hat{V}_x^{i,\sigma}(\mathbf{r}),
\tag{2.31}
$$

$$
\hat{V}_x^{i,\sigma}(\mathbf{r}) = -\sum_j\int d\mathbf{r}'\,\psi_j^{\sigma*}(\mathbf{r}')\psi_i^\sigma(\mathbf{r}')\frac{1}{|\mathbf{r}-\mathbf{r}'|}\frac{\psi_j^\sigma(\mathbf{r})}{\psi_i^\sigma(\mathbf{r})}
\tag{2.32}
$$

For the homogeneous electron gas, the Hartree-Fock equation can be solved analytically, leading to

$$
\varepsilon_k = \frac{1}{2}k^2 + \frac{k_F}{\pi}f(x),
\tag{2.33}
$$
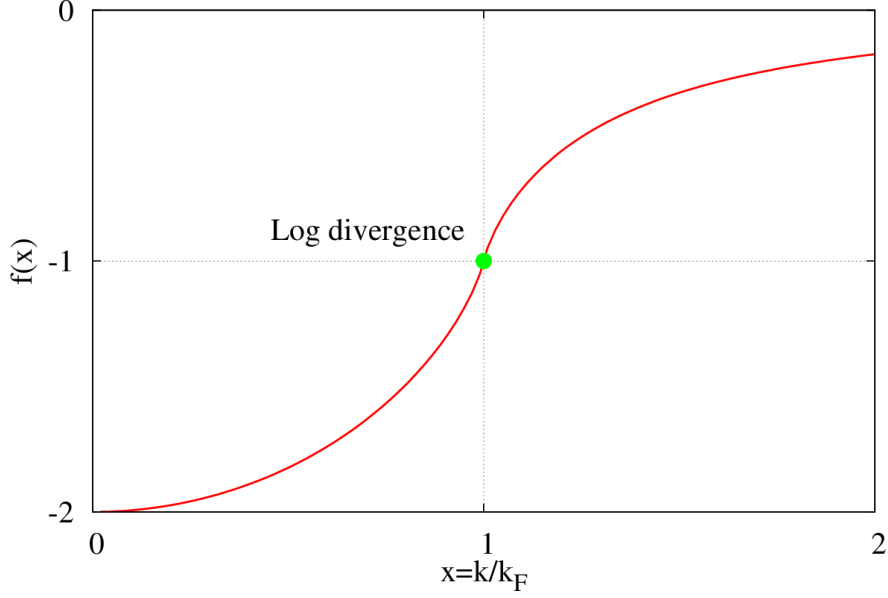
Figure 2.1: The factor $f(x)$ in Hartree-Fock approximation for homogeneous electron gas.

where

$$f(x) = -\left(1 + \frac{1-x^2}{2x} ln\left|\frac{1+x}{1-x}\right|\right), \tag{2.34}$$

with $x = k/k_F$.

Figure 2.1 shows that $f(x)$ is always negative with $f(0) = -2$ and $f(x \to \infty) = 0$. There is a singularity at the Fermi level ($x = 1$), however the value of $f(x)$ is well defined, $f(x \to 1) = -1$. Thus, the band width is boarder (by $\Delta W = k_F/\pi$ for homogeneous electron gas) in Hartree-Fock than in Hartree approximation. The singularity at the Fermi level is due to the long-range Coulomb interaction. This problem leads to zero density of state at the Fermi level. This failure of Hartree-Fock approximation persists even for electron in a solid if the system is metallic. It can be avoided if there is a finite band gap (i.e. insulator or semiconductor) or if the Coulomb interaction is screened to be an effective short-range interaction.

2.3 Exchange and correlation

As mentioned above, the key problem in electronic structure theory is the exchange-correlation part. The interactions between electrons always involve pairs of electron, thus, the two-body correlation function is sufficient to describe many properties. If we denote $n(\mathbf{r}, \sigma; \mathbf{r}', \sigma')$ as the probability of finding two electrons with spins σ and σ', at positions $\mathbf{r}$ and $\mathbf{r}'$ respectively, and $n(\mathbf{r}, \sigma)$ as the probability of finding an individual electron with spin σ at position $\mathbf{r}$, the measure of correlation function for a pair of electrons is given by

$$\Delta n(\mathbf{r}, \sigma; \mathbf{r}', \sigma') = n(\mathbf{r}, \sigma; \mathbf{r}', \sigma') - n(\mathbf{r}, \sigma)n(\mathbf{r}', \sigma') \tag{2.35}$$

The electron correlation is neglected in Hartree-Fock approximation, (except that required by the exclusion principle) and must be distinguished from the exchange hole in HFA, which is given by

$$\Delta n_{HFA}(\mathbf{r}, \sigma; \mathbf{r}', \sigma') = -\delta_{\sigma,\sigma'} \left| \sum_i \psi_i^{\sigma*}(\mathbf{r}) \psi_i^{\sigma}(\mathbf{r}') \right|^2, \tag{2.36}$$

with

$$n_{HFA}(\mathbf{r}, \sigma; \mathbf{r}', \sigma') = \frac{1}{2!} \sum_{i,j} \left| \begin{matrix} \psi_i(\mathbf{r}, \sigma) & \psi_i(\mathbf{r}', \sigma') \\ \psi_j(\mathbf{r}, \sigma) & \psi_j(\mathbf{r}', \sigma') \end{matrix} \right|^2 \tag{2.37}$$

On the other hand, the exchange term explicitly appears in the Hartree-Fock approximation, it includes two effects: Pauli exclusion and the self-term ($i = j$ in eqn. 2.28) which must cancel the unphysical self-term in the direct Coulomb Hartree energy. The exchange term lowers the total energy, which may be interpreted as the interaction of each electron with a positive "exchange hole" surrounding it. The exchange energy in HFA can be written in terms of the exchange hole as

$$E_x = \left[\langle \hat{V}_{int} \rangle - E_{Hartree}(n) \right]_{HFA} = \frac{1}{2} \sum_\sigma \int d^3r \int d^3r' \frac{\Delta n_{HFA}(\mathbf{r}, \sigma; \mathbf{r}', \sigma')}{|\mathbf{r} - \mathbf{r}'|} \tag{2.38}$$

As one can see from Eqn. 2.38, calculation of E_x involves computation of a non-local quantity $\Delta n_{HFA}(\mathbf{r}, \sigma; \mathbf{r}', \sigma')$ which is computationally demanding. As we will see later, DFT dramatically reduces this computational complexity.

2.4 Fundamentals of density functional theory (DFT)

The original form of density functional theory was proposed by Thomas[39] and Fermi[40] in 1927, shortly after Schrödinger [41] (1926) published his paper marking the beginning of wave mechanics. However it did not attract much attention due to the rough approximation which missed essential physics and chemistry, such as shell structures of atoms and binding energy of molecules. The modern formulation of DFT was formulated about 40 years later by Hohenberg and Kohn (1964)[42], who considered the electron density a basic (fundamental) variable from which other properties can be calculated. Later, Kohn and Sham (1965)[43] developed the theory in terms of solving a set of single-particle equations, also known as Kohn-Sham equations. One of the reasons which makes DFT a powerful tool in condensed matter theory, as Kohn put it in his Nobel lecture[44], is that it breaks the exponential wall in many-electron wavefunction method which makes it extremely difficult to calculate the electronic structure for a system with number of electrons in the neighborhood of $N_0 \approx 10$ or larger. Thanks to the development in numerical techniques as well as the improvement of modern computers, DFT can handle much larger number of electrons.

The DFT is based upon two Hohenberg-Kohn theorems[42]. Here, only the theorems are presented for the sake of completeness. The proofs of these theorems are fairly simple and can be found in Hohenberg and Kohn's original paper or in the reference [38] or [44].

Theorem 1. *For any system of interacting particles in an external potential $V_{ext}(\mathbf{r})$, the potential $V_{ext}(\mathbf{r})$ is determined uniquely, except for a constant, by the ground state particle density $n_0(\mathbf{r})$.*

Since the Hamiltonian is thus fully determined, except for a constant shift of the energy, it follows that the many-body wavefunctions for all states (ground and excited) are also determined. It naturally follows that

Corollary 1. *All properties of the system are completely determined given only the ground state density $n_0(\mathbf{r})$.*

This theorem, however, only states that in order to understand properties of a system, only the ground state density is required but does not give any guidance on how to find that density, which is given in the second theorem.

Theorem 2. *A universal functional for the energy $E[n]$ in terms of the density $n(\mathbf{r})$ can be defined, valid for any external potential $V_{ext}(\mathbf{r})$. For any particular $V_{ext}(\mathbf{r})$, the exact ground state energy of the system is the global minimum value of this functional, and the density $n(\mathbf{r})$ that minimizes the functional is the ground state density $n_0(\mathbf{r})$.*

This leads to a lemma

Corollary 2. *The functional $E[n(\mathbf{r})]$ alone is sufficient to determine the exact ground state energy and density.*

One can easily generalize these theorems to a system with several types of particles since they only change the term $\int d^3 r V_{ext}(\mathbf{r}) n(\mathbf{r})$ in the Halmiltonian. Any such pair of external potential and density will obey Hohenberg-Kohn theorems. For example, one can formulate the spin density functional theory for a system under external magnetic field where spin up and spin down electrons are treated as different types of particles. Within this theory, the particle density is the sum of up- and down-spin density,

$$n(\mathbf{r}) = n_\uparrow(\mathbf{r}) + n_\downarrow(\mathbf{r}), \tag{2.39}$$

and the spin density is

$$s(\mathbf{r}) = n_\uparrow(\mathbf{r}) - n_\downarrow(\mathbf{r}). \tag{2.40}$$

The energy functional now becomes

$$E = E_{HK}[n,s] = E'[n], \tag{2.41}$$

where n in $E'[n]$ is a function of both position $\mathbf{r}$ and spin σ.

Even with two Hohenberg-Kohn theorems and their lemmas, it is still difficult to solve the Schrödinger equation to get the energy and the density of electrons. Another essential part in DFT

27

is the Kohn-Sham ansatz[43] which, in principle, leads to exact calculation of electronic structure for many-body system using independent-particle methods. Kohn and Sham proposed that the ground state density of an interacting system is equal to that of a suitably chosen non-interacting system, leading to soluble independent-particle equations, with all the many-body terms included in a exchange-correlation functional of the density. This approach has proven to be very powerful and has become the basis of most "*first-principles*" or "*ab-initio*" calculations.

The Kohn-Sham ansatz is based on two assumptions:

1. The exact ground state density can be represented by the ground state density of an auxiliary non-interacting system.

2. The auxiliary Hamiltonian is chosen to have the usual kinetic term and an effective local potential $V_{eff}^{\sigma}(\mathbf{r})$.

Then, the density of particles and the ground state energy functional in Kohn-Sham approximation can be written as

$$n(\mathbf{r}) = \sum_{\sigma} n(\mathbf{r}, \sigma) = \sum_{\sigma} \sum_{i=1}^{N^{\sigma}} |\psi_i^{\sigma}(\mathbf{r})|^2, \tag{2.42}$$

$$E_{KS} = T_s[n] + \int d\mathbf{r} V_{ext}(\mathbf{r}) n(\mathbf{r}) + E_{Hartree}[n] + E_{II} + E_{xc}[n], \tag{2.43}$$

where N^{σ} is number of electrons with spin σ, T_s is the kinetic energy of the independent-electron system, given by

$$T_s = -\frac{1}{2} \sum_{\sigma} \sum_{i=1}^{N^{\sigma}} \langle \psi_i^{\sigma} | \nabla^2 | \psi_i^{\sigma} \rangle = \frac{1}{2} \sum_{\sigma} \sum_{i=1}^{N^{\sigma}} \int d^3 r |\nabla \psi_i^{\sigma}(\mathbf{r})|^2, \tag{2.44}$$

the Hartree energy is given by

$$E_{Hartree}[n] = \frac{1}{2} \int d^3 r d^3 r' \frac{n(\mathbf{r}) n(\mathbf{r}')}{|\mathbf{r} - \mathbf{r}'|}. \tag{2.45}$$

All the effects of many-body exchange and correlation are incorporated into E_{xc} which can be written as

$$E_{xc}[n] = \langle \hat{T} \rangle - T_s[n] + \langle \hat{V}_{int} \rangle - E_{Hartree}[n]. \tag{2.46}$$

So, in principle, if E_{xc} is known the the exact ground state energy and density of the particles can be found.

Using variational method, one gets the Kohn-Sham equations

$$(H_{KS}^{\sigma} - \varepsilon_i^{\sigma})\psi_i^{\sigma}(\mathbf{r}) = 0, \tag{2.47}$$

where

$$H_{KS}^{\sigma}(\mathbf{r}) = -\frac{1}{2}\nabla^2 + V_{KS}^{\sigma}(\mathbf{r}), \tag{2.48}$$

$$= -\frac{1}{2}\nabla^2 + V_{ext}(\mathbf{r}) + V_{Hartree}(\mathbf{r}) + V_{xc}^{\sigma}(\mathbf{r}). \tag{2.49}$$

The eigenvalues of the Kohn-Sham equations have, in general, no physical meaning with only one exception – the highest eigenvalue in a finite system, which is minus of the ionization energy and is exact.[45]

In order to find the form of E_{xc} and V_{xc}^{σ}, one can approximate them as a local or nearly local functional of the density. The exchange-correlation energy can be written as

$$E_{xc}[n] = \int d\mathbf{r}\, n(\mathbf{r})\varepsilon_{xc}([n],\mathbf{r}), \tag{2.50}$$

where ε_{xc} is an energy per electron. Note that for simplicity only non-polarized case is considered. ε_{xc} is related to the exchange-correlation hole and their relation can be found using the "adiabatic connection" formula with the scaled electronic charge λe^2, where λ varies from 0 (non-interacting) to 1 (actual value),

$$E_{xc}[n] = \int_0^1 d\lambda \langle \Psi_{\lambda}| \frac{dV_{int}}{d\lambda} |\Psi_{\lambda}\rangle - E_{Hartree}[n] = \frac{1}{2}\int d^3r\, n(\mathbf{r}) \int d^3r' \frac{\bar{n}_{xc}(\mathbf{r},\mathbf{r}')}{|\mathbf{r}-\mathbf{r}'|} \tag{2.51}$$

in which, $\bar{n}_{xc}(\mathbf{r},\mathbf{r}')$ is called "coupling-constant-averaged hole",

$$\bar{n}_{xc}(\mathbf{r},\mathbf{r}') = \int_0^1 d\lambda\, n_{xc}^{\lambda}(\mathbf{r},\mathbf{r}'). \tag{2.52}$$

Here $n_{xc}(\mathbf{r},\mathbf{r}')$ is the exchange hole, given in eqn. 2.37, summed over parallel and anti-parallel spin. Finally one gets the expression for the exchange-correlation density

$$\varepsilon_{xc}([n],\mathbf{r}) = \frac{1}{2}\int d^3r' \frac{\bar{n}_{xc}(\mathbf{r},\mathbf{r}')}{|\mathbf{r}-\mathbf{r}'|}. \tag{2.53}$$

This equation shows that the exact exchange-correlation energy can be considered as the average of the exchange-correlation hole over the interaction from independent-particle ($e^2 = 0$) to fully interacting electrons ($e^2 = 1$). This becomes an important rationale for improvements of the approximation for E_{xc}, i.e. the hybrid functional approach which will be discussed later in this chapter.

The exchange-correlation potential V_{xc}^{σ} now can be found from the functional derivative of E_{xc},

$$V_{xc}^{\sigma}(\mathbf{r}) = \varepsilon_{xc}([n], \mathbf{r}) + n(\mathbf{r}) \frac{\delta \varepsilon_{xc}([n], \mathbf{r})}{\delta n(\mathbf{r}, \sigma)}. \tag{2.54}$$

It is important to note that the second term in 2.54 (sometimes called the "response potential") is discontinuous at a band gap. This leads to a "derivative discontinuity" that changes all the electrons' potential by a constant when a single electron is added to the system. Thus, even with exact Kohn-Sham theory, the obtained band gap is not the same as the actual one. This discontinuity can be understood by analyzing the kinetic energy of the independent-electron system T_s in Eqn. 2.44. Since, ψ_i^{σ} are different for different bands, T_s changes discontinuously when going from an occupied to an empty band. Thus it has discontinuous derivative with respect to density for filled bands. It can also be seen that the exact exchange-correlation functional must have discontinuous derivative. This discontinuity, however, cannot be incorporated into simple functionals such as local density (LDA) and generalized gradient (GGA) approximations (which are discussed later in this chapter), leading to what has been known as "Band-gap problem" in semiconductors.

2.5 Functionals for exchange and correlation

The central problem in DFT is how to treat the exchange-correlation energy E_{xc} or the exchange-correlation potential $V_{xc}^{\sigma}(\mathbf{r})$. This has been an active field in the DFT in the last several decades. All treatments of exchange-correlation functional are approximated and can be classified into two main categories: (1) local and semi-local approximation, i.e. local (spin) density approximation (LDA/LSDA), generalized gradient approximation (GGA), meta-GGA and (2) non-local approximation such as hybrid functional (hyper-GGA), random phase approximation, etc.
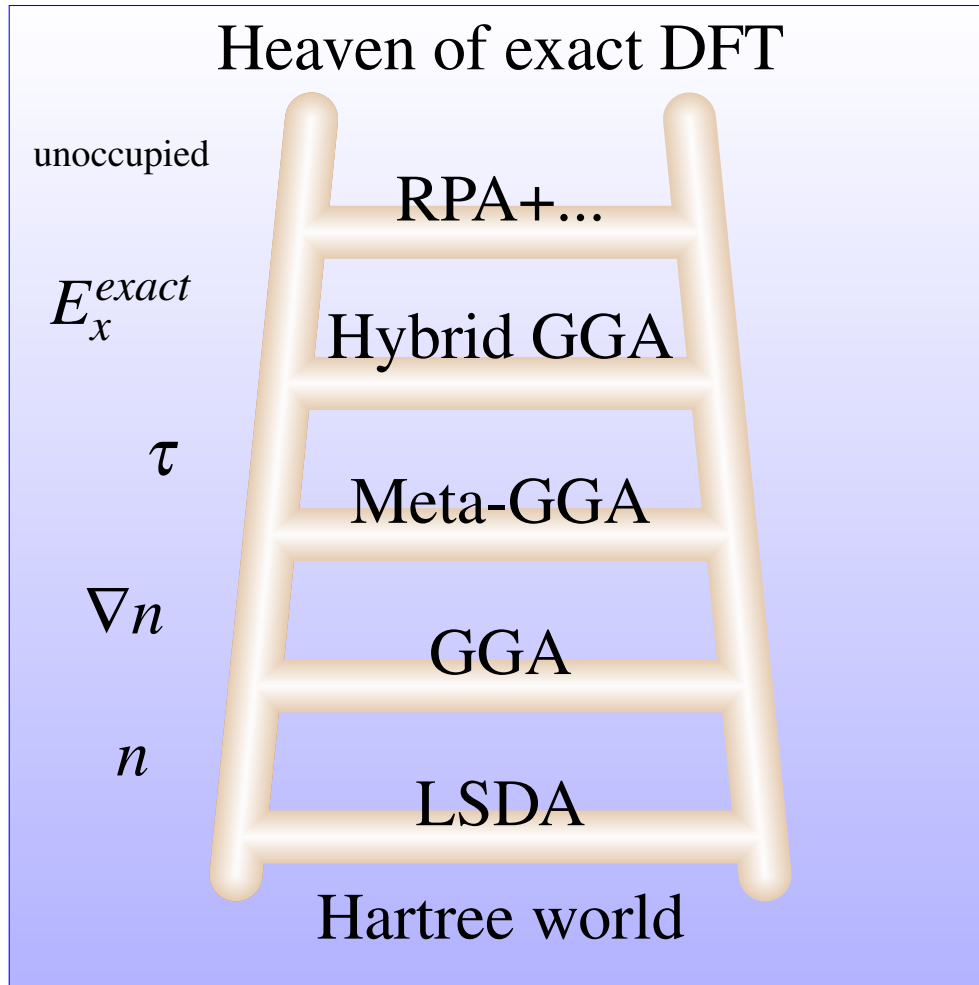
Figure 2.2: The ladder of density functional theory. Notations on the left side represent the terms added to the theory, i.e. only density n functional is considered in LSDA, GGA adds gradient correction ∇n, meta-GGA adds kinetic energy density τ, hybrid GGA takes into account parts of exact non-local exchange energy E_x^{exact}, RPA includes unoccupied orbital.

The improvement of exchange-correlation approximations can be visualized as climbing a ladder (sometimes called Jacob ladder)[46] – which can be sometimes slippery – of which the ground is mean field Hartree system and the top is the exact Kohn-Sham exchange-correlation functional (figure 2.2). As one climbs up the ladder, the exchange-correlation functionals become more complicated, more sophisticated and, in general, more accurate (but not always). (list of some approximations are given in Table 2.1) The first three rungs of the ladder are local/semi-local approximations where the first rung of the ladder is L(S)DA in which exchange-correlation is functional of only the local spin density $n^\sigma(\mathbf{r})$, the second rung is GGA which adds the gradient correction of the

Table 2.1: Summary of approximations used in DFT

Rung	Name	Exchange	Correlation	%HF/screening
LDA	PZ[a]	PZ	PZ	–
GGA	PBE[b]	PBE[47]	PBE[47]	–/–
	PW91[c]	PW91[48]	PW91[48]	–/–
	EV93[d]	EV93[49]	LSDA	–/–
	WC[e]-PBE	WC[50]	PBE[47]	–/–
Meta-GGA	TPSS[f]	TPSS[51]	TPSS[51]	–/–
	mBJ[g]	mBJ[52]	PBE[47]	–/–
Hybrid	B3LYP	B[h][53]	LYP[i][54]	16-20/No[55]
	B3PW91	B[53]	PW91[48]	16-20/No
	B1LYP	B[53]	LYP[54]	/No[56]
	B1WC	WC[50]	PW91[48]	16-20/No[57]
	PBE0	PBE[47]	PBE[47]	25/No[58]
	HSE[j]	PBE[47]	PBE[47]	25/Yes[59–61]

[a]Perdew and Zunger
[b]Perdew, Burke and Ernzerhof
[c]Perdew and Wang
[d]Engel and Vosko
[e]Wu and Cohen

[f]Tao, Perdew, Staroverov and Scuseria
[g]modified Becke-Johnson potential
[h]Becke
[i]Lee, Yang and Parr
[j]Heyd, Scuseria and Ernzerhof

density, and the third rung is meta-GGA, where the kinetic energy dependence is included. These semi-local approximations work well for many systems where the density varies slowly. They fail where one has a non-uniform, high density and rapidly varying regions, or has an open systems where the number of electrons fluctuates. The fourth and the fifth rungs of the ladder are non-local approximations where the non-local exchange is included. Computationally, the difficulty of calculations changes slightly at the first three rungs of approximation but then increases steeply by the fourth rung. It is one of the reasons why the non-local approximation was not widely used until last several years when the computing technologies became affordable for such calculations.

It is important to point out that while for the first three and the fifth rungs, the functionals do not involve any fitting, for the forth one, empirical fitting is unavoidable.

The next section gives a brief introduction to some of the approximations including LSDA, GGA, LDA+U and hybrid functional. These approximations have been used in my calculations of electronic structures of complex multi-component systems. Descriptions of other approximation

can be found in literature, such as in reference [38].

2.5.1 Local (spin) density approximation (LSDA) and the gradient correction (GGA)

The first local density approximation was proposed by Dirac [62] to be used with Thomas-Fermi density functional[39, 40]. Later, in 1951, Slater [63], starting from Hartree-Fock approximation, proposed the local spin density approximation (LSDA) which included spin-dependent functional. Within LSDA the exchange-correlation can be written in general as

$$
\begin{aligned}
E_{xc}^{LSDA}[n^{\uparrow}, n^{\downarrow}] &= \int d^3 r n(\mathbf{r}) \varepsilon_{xc}(n^{\uparrow}(\mathbf{r}), n^{\downarrow}(\mathbf{r})) \\
&= \int d^3 r n(\mathbf{r}) \left[\varepsilon_x(n^{\uparrow}(\mathbf{r}), n^{\downarrow}(\mathbf{r})) + \varepsilon_c(n^{\uparrow}(\mathbf{r}), n^{\downarrow}(\mathbf{r}))(\mathbf{r}) \right],
\end{aligned}
\tag{2.55}
$$

where ε_{xc} is assumed to be the same as in a homogeneous electron gas. In this equation the spin-quantization axis is assumed to be the same everywhere (collinear spin). For the non-collinear case, one can replace the density by the local spin density matrix

$$
\rho^{\alpha\beta}(\mathbf{r}) = \sum_i f_i \psi_i^{\alpha*}(\mathbf{r}) \psi_i^{\beta}(\mathbf{r}).
\tag{2.56}
$$

Now the Kohn-Sham hamiltonian becomes a 2×2 matrix. The only complication now is that one has to find the local axis of spin quantization. The form of ε_{xc} is, however, the same.

LSDA works the best for systems close to a homogeneous gas (nearly free-electron metal) and the worst for the inhomogeneous ones (atoms, molecules or localized-electron systems). The reason is that, unlike in Hartree-Fock approximation, the unphysical self-term in Hartree interaction is only approximately canceled by the exchange term. This error is negligible in a homogeneous (delocalized) system. Furthermore, LSDA also misses the derivative discontinuity of energy functional which generally underestimates the band gap in semiconductors and insulators.

The first step to improve LSDA is by taking into account the effect of spatially varying density (inhomogeneous) by including the gradient of density in the functional. There are various approaches to achieve this goal, among which generalized gradient approximation (GGA) is the

most successful and widely used. In GGA, the E_{xc} can be written as

$$E_{xc}^{GGA}[n^\uparrow, n^\downarrow] = \int d^3rn(\mathbf{r})\varepsilon_{xc}(n^\uparrow, n^\downarrow, |\nabla n^\uparrow|, |\nabla n^\downarrow|, ...),$$

$$= \int d^3rn(\mathbf{r})\varepsilon_x^{hom}(n)F_{xc}(n^\uparrow, n^\downarrow, |\nabla n^\uparrow|, |\nabla n^\downarrow|, ...), \qquad (2.57)$$

where ε_x^{hom} is the exchange energy of the unpolarized homogeneous electron gas and F_{xc} is a dimensionless function.

For the exchange part, F_x, it is easy to show that only spin-unpolarized consideration is sufficient. The expansion of F_x is given, to some lowest orders, by

$$F_x = 1 + \frac{10}{81}s_1^2 + \frac{146}{2025}s_2^2 + \cdots, \qquad (2.58)$$

where s_m are dimensionless reduced density gradients defined as

$$s_m = \frac{1}{(2k_F)^m}\frac{|\nabla^m n|}{n} \qquad (2.59)$$

The correlation part is more difficult and can be expanded in s_m as

$$F_c = \frac{\varepsilon_c^{LDA}}{\varepsilon_x^{LDA}}(1 - 0.219.51s_1^2 + \cdots). \qquad (2.60)$$

There are many forms for $F_x(n,s)$, where only terms with order of $s = s1$ or lower are considered, higher terms ($m \geq 2$) are neglected. Among those forms, there are three commonly used forms proposed by Becke [53], Perdew and Wang [48] and Perdew et al. [47]. For small s, ($0 < s \leq 3$) – slowly varying density – which is relevant for most physical systems, different GGAs give similar improvements. Even though GGA has been successfully used to predict properties of many system, its accuracy is still not enough and the improvement over LDA is modest.

2.5.2 Local treatment of strongly correlated electron systems: LDA+U

As discussed earlier, in LSDA, the self-interaction energy is only partly canceled, and the discontinuity in derivative of energy with respect to density at integral values of n is not included. These problems are severe for systems with localized electrons such as d of f electrons. There exist

34

corrections to this problem within the local approximation including *self interaction correction* (SIC)[64] and LDA+U[65]. While SIC can produce very well the nature of localized electrons, its one-electron energies are usually in strong disagreement with experiments. Here we only discuss the LDA+U approximation, which can be regarded as a first-principles method since U can be calculated from *ab-initio* calculations, making it parameter-free.

LDA+U is the method that involve LDA- or GGA-type (more correctly GGA+U) calculations with an additional orbital-dependent Hubbard-like interaction, $\frac{1}{2}U\sum_{i\neq j}n_i n_j$, where $N = \sum_i n_i$ is the total number of localized (says d) electrons. Here, U is an effective Coulomb repulsion energy needed to place two electrons on the same orbital, and is given by

$$U = E(d^{n+1}) + E(d^{n-1}) - 2E(d^n), \tag{2.61}$$

where d denotes localized orbitals such as those occupied by d and f electrons. One also has to subtract the Coulomb energy which is already included in LDA, $E = UN(N-1)/2$, to avoid double counting. The energy in LDA+U, then , is given by

$$E = E_{LDA} - \frac{U}{2}N(N-1) + \frac{1}{2}U\sum_{i\neq j}n_i n_j. \tag{2.62}$$

The orbital energies ε_i are derivatives of the total energy with respect to orbital occupations n_i:

$$\varepsilon_i = \varepsilon_{LDA} + U(\frac{1}{2} - n_i). \tag{2.63}$$

This equation means that, if one neglects the hybridization between the localized and extended states, the effect of U is to shift the LDA orbital energy by $-U/2$ for occupied bands ($n_i = 1$) and $U/2$ for unoccupied bands ($n_i = 0$). Taking into account the exchange effect between the same spin electrons, the energy becomes

$$E = E_{LDA} - \frac{U}{2}N(N-1) - \frac{J}{4}N(N-2) + \frac{1}{2}U\sum_i n_i^\sigma n_i^{-\sigma} + \frac{U-J}{2}\sum_{i\neq j}n_i^\sigma n_j^\sigma, \tag{2.64}$$

35

where U and J can be obtained by using the Slater integrals F^k[66]

$$U = F^0, \tag{2.65}$$

$$U - J = F^0 - (F^2 + F^4), \tag{2.66}$$

$$J = \frac{F^2 + F^4}{14} \tag{2.67}$$

One can calculate U and J by from constrained DFT calculations using supercell model. In a method proposed by Gunnarsson et al. [67] one removes the transfer integrals between the d orbitals and the other orbitals in a system and obtains U by using the equation $U = \delta^2 E / \delta n_d^2$.[66, 68]

Various examples of LDA+U calculations are given in the reference [65]. A well-known example is the case of CuO-based superconductors[65] which are found to be non-magnetic metals in LDA and GGA calculations whereas LDA+U calculations give the correct antiferromagnetic insulators. Another example showing the severe errors in LDA/GGA which can be corrected by LDA+U is the case of CoO Mott-insulator. CoO has a large band gap of 2.4 eV[38] which is predicted to be a metal within LDA/GGA, with Co-d state located at the Fermi level[69]. LDA+U[65, 70] correctly opens a band gap in good agreement with experiment.

Anisimov et al. [65] brought up an important relationship between LDA+U and the Green function (GF) method; GF correctly describes the frequency-dependent quasiparticle energies. A simple approximation to the GF method is GW approximation (GWA)[71], where G and W stand for Green and response functions respectively. The authors note that both GW approximation and LDA+U are Hartree-Fock-like theories which give the corrections to the electron self-energy. The only difference between the two methods is the procedure for calculating the screened Coulomb interaction. In LDA+U, it can be done by using constrained DFT, whereas GWA requires the computation of a much more difficult response function W. Thus, LDA+U can be considered, at least for localized orbitals, an approximation of GWA.

2.5.3 Non-local treatment of exchange-correlation in correlated electron systems: Hybrid functional theory

In spite of the success of local DFT approximations, they fails in many cases where it is believed that non-local effect of exchange-correlation are important. In chapter 4 I will discuss one of such systems. To tackle this problem, hybrid functionals have been introduced. The rationale for the hybrid functional theory arises from the equation 2.51 which can be written as

$$E_{xc} = \int_0^{\lambda} d\lambda E_{xc,\lambda}, \tag{2.68}$$

where

$$E_{xc,\lambda} = \langle \Psi_{\lambda} | \frac{dV_{int}}{d\lambda} | \Psi_{\lambda} \rangle - E_{Hartree}[n]. \tag{2.69}$$

At $\lambda = 0$ the non-interacting Kohn-Sham system is recovered and at $\lambda = 1$ it is the fully interacting system. The first formulation of hybrid function was proposed in 1993 by Becke [72] who assumed a linear dependence on λ and approximated the integral by

$$E_{xc}^{h} = \frac{1}{2}(E_x^{HF} + E_{xc}^{DFA}), \tag{2.70}$$

where $E_x^{HF} = E_{xc,\lambda=0}$ is the exact exchange energy of Kohn-Sham orbital, E_{xc}^{DFA} is the exchange-correlation energy at $\lambda = 1$ in the density functional approximation (DFA), such as LDA or GGA. Later Becke [55] parameterized the formulation including three fitting parameters $(\alpha_0, \alpha_x, \alpha_c)$,

$$E_{xc}^{h} = E_{xc}^{LDA} + \alpha_0(E_x^{HF} - E_x^{DFA}) + \alpha_x E_x^{Becke} + \alpha_c E_c, \tag{2.71}$$

where E_x^{Becke} is the exchange energy in the form proposed by Becke himself[53]. For convenience, each formulation of hybrid functional method is usually named in such a way that it indicates which exact exchange and which correlation function used. For example, two popular formulations of such three-parameter hybrid functional are B3PW91 and B3LYP (some of other formulations are given in table 2.1), both of which use the exact exchange proposed by [55], the former uses the GGA exchange-correlation by Perdew and Wang [48] while the latter uses that by Lee et al. [54]. This three-parameter formulation later was simplified to one-parameter with $\alpha_x = 1 - \alpha_0 = 1 - \alpha$

37

and $\alpha_c = 1$,[56] i.e.,

$$E_{xc}^h = E_{xc}^{DFA} + \alpha(E_x - E_{xc}^{DFA}). \tag{2.72}$$

Perdew, Ernzerhof and Burke[58] suggest the use of $\alpha = 1/4$. Combining with PBE[47] correlation one ends up with the popular un-screened hybrid functional PBE0[58].

In all the approximation discussed above, the bare Coulomb interactions are considered which include short-range and long-range parts. This greatly increases the demand of computational resources for hybrid functional calculations. It is, however, known that the short-range exchange interaction decays exponentially as a function of the distance. Furthermore, the long-range Coulomb interaction causes a divergence near the Fermi level as discussed earlier. This problem can be avoided by screening the interaction. The formulation for hybrid functionals based on a screened Coulomb potential was proposed by Heyd, Scuseria and Ernzerhof (HSE) in 2003[59] which was then amended in 2006[61] (HSE06). In this formalism the Coulomb operator is split into short-range (SR) and long-range (LR) components:

$$\frac{1}{r} = \frac{erfc(\omega r)}{r} + \frac{erf(\omega r)}{r}, \tag{2.73}$$

where $erfc(\omega r) = 1 - erf(\omega r)$ and ω is an adjustable parameter. The short- and long-range parts correspond to the *erfc* and *erf* terms respectively. At $\omega = 0$, the long-range term vanishes and a full range operator recovered, which is PBE0-type. At $\omega = \infty$, the interaction is completely screened so that it falls back to (semi)local approximation. In HSE06, the PBE correlation is used and the energy functional can be written as

$$E_{xc}^{PBEh} = \alpha E_x^{HF,SR}(\omega) + (1-\alpha)E_x^{PBE,SR}(\omega) + E_x^{PBE,LR}(\omega) + E_c^{PBE}. \tag{2.74}$$

Thus, in this formulation, the non-local HF exchange is included only in the *SR* term whereas the *LR* term is that of PBE. This approach not only helps to reduce the computing demand but also removes the Fermi surface singularity. HSE showed that screened-Coulomb-interaction hybrid calculations greatly improved the DFT results[59–61] especially in obtaining the band gaps which were in much better agreements with experiments. HSE-type calculations have proved to be suc-

cessful in many systems[59–61] with "standard" values of parameters, $\alpha = 1/4$ and $\omega = 0.2$. In this thesis, most of the HSE calculations were done using these values.

2.6 Boltzmann's equation for transport

As discussed in chapter 1, Boltzmann's equation of transport is the most successful and practical approach to study thermoelectric properties of materials. Applying this approach, one can calculate transport quantities, particularly thermoelectric properties, from the electronics structure obtained from DFT or similar calculations. In this section, I give a brief introduction about Boltzmann's transport equation in the presence of temperature gradient, more comprehensive discussions can be found in other textbooks on solid states physics, such as "Principles of the Theory of Solids" by Ziman [73].

For a steady state, the Boltzmann's equation is given by

$$\left[\frac{\partial f_{\mathbf{k}}(\mathbf{r},t)}{\partial t}\right]_{diff} + \left[\frac{\partial f_{\mathbf{k}}(\mathbf{r},t)}{\partial t}\right]_{field} + \left[\frac{\partial f_{\mathbf{k}}(\mathbf{r},t)}{\partial t}\right]_{scatt} = 0, \tag{2.75}$$

where the subscripts $diff$, $field$ and $scatt$ denote the terms corresponding to diffusion, external field and scattering respectively, $f_{\mathbf{k}}(\mathbf{r},t)$ is the probability of having an electron (hole) with wave vector $\mathbf{k}$ at position $\mathbf{r}$ in space at a given time t. Note that $f_{\mathbf{k}}(\mathbf{r},t)$ is not for the equilibrium but for the steady state. At equilibrium, $f_{\mathbf{k}}^0(\mathbf{r})$ is the single particle Fermi distribution,

$$f_{\mathbf{k}}^0 = \frac{1}{\exp\left(\frac{\varepsilon_{\mathbf{k}} - \mu}{k_B T(\mathbf{r})}\right) + 1}, \tag{2.76}$$

where $\varepsilon_{\mathbf{k}}$ is the energy corresponding to the wavevector $\mathbf{k}$, μ is the chemical potential and k_B is the Boltzmann constant. (The band index has been omitted for simplicity.) We assume that each state $\mathbf{k}$ is two-fold spin degenerate and ignore the spin index since we do not consider magneto transport in this thesis. The Boltzmann's equation states that the net rate of change in $f_{\mathbf{k}}(\mathbf{r},t)$ is zero for any $\mathbf{k}$ at given point in space.

In order to find the explicit solution to the Boltzmann's equation we apply Liouville's theorem for $\mathbf{r}$,

$$f_{\mathbf{k}}(\mathbf{r},t) = f_{\mathbf{k}}(\mathbf{r} - t\mathbf{v}_{\mathbf{k}}, 0), \tag{2.77}$$

where $\mathbf{v}_{\mathbf{k}} = \partial \varepsilon_{\mathbf{k}}/\partial \mathbf{k}$. The diffusion term in 2.75 can be written as

$$\left[\frac{\partial f_{\mathbf{k}}(\mathbf{r})}{\partial t} \right]_{diff} = -\frac{\partial f_{\mathbf{k}}}{\partial T} \frac{\partial T}{\partial \mathbf{r}} \cdot \frac{\partial \mathbf{r}}{\partial t} = -\frac{\partial f_{\mathbf{k}}}{\partial T} \mathbf{v}_{\mathbf{k}} \cdot \nabla T. \tag{2.78}$$

The derivative of $f_{\mathbf{k}}$ with respect to T can be evaluated by using the definition of Fermi distribution,

$$\frac{\partial f_{\mathbf{k}}}{\partial T} = \frac{\exp\left(\frac{\varepsilon_{\mathbf{k}} - \mu}{k_B T} \right)}{\left[\exp\left(\frac{\varepsilon_{\mathbf{k}} - \mu}{k_B T} \right) + 1 \right]^2} \frac{\varepsilon_{\mathbf{k}} - \mu}{k_B T^2} = \left(-\frac{\partial f_{\mathbf{k}}}{\partial \varepsilon_{\mathbf{k}}} \right) \frac{\varepsilon_{\mathbf{k}} - \mu}{T}. \tag{2.79}$$

One, then, gets the rate of change of the distribution function due to diffusion:

$$\left[\frac{\partial f_{\mathbf{k}}(\mathbf{r})}{\partial t} \right]_{diff} = \left(-\frac{\partial f_{\mathbf{k}}}{\partial \varepsilon_{\mathbf{k}}} \right) (\varepsilon_{\mathbf{k}} - \mu) \left(-\frac{\mathbf{v}_{\mathbf{k}} \cdot \nabla T}{T} \right). \tag{2.80}$$

Similarly, one can apply Liouville theorem in $\mathbf{k}$-space and consider only external electric field $\mathbf{E}$, where

$$\hbar \dot{\mathbf{k}} = e\mathbf{E}, \tag{2.81}$$

to get the formulation for the external field term,

$$\left[\frac{\partial f_{\mathbf{k}}}{\partial t} \right]_{field} = e \left(-\frac{\partial f_{\mathbf{k}}}{\partial \varepsilon_{\mathbf{k}}} \right) \mathbf{v}_{\mathbf{k}} \cdot \mathbf{E}. \tag{2.82}$$

The scattering term in 2.75 is more complicated and in general is energy-dependent. Within the scope of this thesis, we make relaxation time approximation which have been successfully applied in many system.[74] Within this approximation the scattering term can be given by

$$\left[\frac{\partial f_{\mathbf{k}}}{\partial t} \right]_{scatt} = -\frac{f_{\mathbf{k}} - f_{\mathbf{k}}^0}{\tau_{\mathbf{k}}} = -\frac{g_{\mathbf{k}}}{\tau_{\mathbf{k}}}, \tag{2.83}$$

where $g_{\mathbf{k}} = f_{\mathbf{k}} - f_{\mathbf{k}}^0$, $\tau_{\mathbf{k}}$ is the carrier's relaxation time. Equation 2.75 can be rewritten as

$$g_{\mathbf{k}} = e\tau_{\mathbf{k}} \left(-\frac{\partial f_{\mathbf{k}}}{\partial \varepsilon_{\mathbf{k}}} \right) \mathbf{v}_{\mathbf{k}} \cdot \mathbf{E} + \tau_{\mathbf{k}} \left(-\frac{\partial f_{\mathbf{k}}}{\partial \varepsilon_{\mathbf{k}}} \right) (\varepsilon_{\mathbf{k}} - \mu) \left(-\frac{\mathbf{v}_{\mathbf{k}} \cdot \nabla T}{T} \right) \tag{2.84}$$

In order to make use of this equation to get other transport properties of materials one can start with the microscopic and macroscopic Ohm's law which relate the current density to the applied electric field and temperature gradient. The microscopic Ohm's law is given by

$$\mathbf{J} = \frac{1}{V}\sum_{\mathbf{k}} e f_{\mathbf{k}} \mathbf{v}_{\mathbf{k}} = \frac{1}{V}\sum_{\mathbf{k}} e g_{\mathbf{k}} \mathbf{v}_{\mathbf{k}}, \tag{2.85}$$

since there is no current at equilibrium,

$$\sum_{\mathbf{k}} e f_{\mathbf{k}}^0 \mathbf{v}_{\mathbf{k}} = 0, \tag{2.86}$$

where V is the volume in real space.

Using the expression of $g_{\mathbf{k}}$ and grouping out the common terms, one can rewrite $\mathbf{J}$ as

$$\mathbf{J} = \frac{1}{V}\sum_{\mathbf{k}} e^2 \tau_{\mathbf{k}}\left(-\frac{\partial f_{\mathbf{k}}}{\partial \varepsilon_{\mathbf{k}}}\right)\mathbf{v}_{\mathbf{k}}\mathbf{v}_{\mathbf{k}} \cdot \left(\mathbf{E} + \frac{1}{eT}\frac{\sum_{\mathbf{k}}\tau_{\mathbf{k}}\left(-\frac{\partial f_{\mathbf{k}}}{\partial \varepsilon_{\mathbf{k}}}\right)(\varepsilon_{\mathbf{k}}-\mu)\mathbf{v}_{\mathbf{k}}\mathbf{v}_{\mathbf{k}}}{\sum_{\mathbf{k}}\tau_{\mathbf{k}}\left(-\frac{\partial f_{\mathbf{k}}}{\partial \varepsilon_{\mathbf{k}}}\right)\mathbf{v}_{\mathbf{k}}\mathbf{v}_{\mathbf{k}}}\cdot(-\nabla T)\right). \tag{2.87}$$

Comparing with the macroscopic Ohm's law in the presences of an external electric field and temperature gradient, given by

$$\mathbf{J} = \overleftrightarrow{\sigma}\mathbf{E} + \overleftrightarrow{\sigma}\overleftrightarrow{S}(-\nabla T) = \overleftrightarrow{\sigma}\left(\mathbf{E} + \overleftrightarrow{S}(-\nabla T)\right), \tag{2.88}$$

one get the expressions for conductivity, $\overleftrightarrow{\sigma}$, and thermopower (Seebeck coefficient), $\overleftrightarrow{S}$, tensors,

$$\overleftrightarrow{\sigma} = \frac{e^2}{V}\sum_{\mathbf{k}}\tau_{\mathbf{k}}\left(-\frac{\partial f_{\mathbf{k}}}{\partial \varepsilon_{\mathbf{k}}}\right)\mathbf{v}_{\mathbf{k}}\mathbf{v}_{\mathbf{k}}, \tag{2.89}$$

$$\overleftrightarrow{S} = (\overleftrightarrow{\sigma})^{-1}\overleftrightarrow{A}, \tag{2.90}$$

where $\overleftrightarrow{A} = \frac{e}{VT}\sum_{\mathbf{k}}\tau_{\mathbf{k}}\left(-\frac{\partial f_{\mathbf{k}}}{\partial \varepsilon_{\mathbf{k}}}\right)(\varepsilon_{\mathbf{k}}-\mu)\mathbf{v}_{\mathbf{k}}\mathbf{v}_{\mathbf{k}}$.

For isotropic system electrical conductivity σ and thermopower S can be calculated using

$$\sigma = e^2 \int_{-\infty}^{+\infty} d\varepsilon\left(-\frac{\partial f_0}{\partial \varepsilon}\right)\Sigma(\varepsilon), \tag{2.91}$$

$$S = \frac{e}{T\sigma}\int_{-\infty}^{+\infty} d\varepsilon\left(-\frac{\partial f_0}{\partial \varepsilon}\right)\Sigma(\varepsilon)(\varepsilon-\mu), \tag{2.92}$$

where μ is the chemical potential, e is the electron charge, f_0 is the Fermi-Dirac distribution function, and $\Sigma(\varepsilon)$, called the transport distribution function, is given by

$$\Sigma(\varepsilon) = \frac{1}{3}\sum_{n,\vec{k}} \mathbf{v}(n,\vec{k})^2 \tau(n,\vec{k})\delta(\varepsilon - \varepsilon(n,\vec{k})).$$ (2.93)

In Eqn. (2.93), n is the band index and the summation is over the first Brillouin zone (BZ), $\mathbf{v}(n,\vec{k})$ is the carrier velocity of an electron in state $(n,\vec{k})$, and $\tau(n,\vec{k})$ is the relaxation time.

By analogy, one can follow a similar procedure for electronic heat current and obtain the expression for zero-field electronic thermal conductivity due to electrons

$$\overleftrightarrow{\kappa}_{elec} = \frac{1}{VT^2}\sum_{\mathbf{k}} \tau_{\mathbf{k}}\left(-\frac{\partial f_{\mathbf{k}}}{\partial \varepsilon_{\mathbf{k}}}\right)(\varepsilon_{\mathbf{k}} - \mu)^2 \mathbf{v_k}\mathbf{v_k}.$$ (2.94)

From the expression of conductivity and thermopower, one can easily see the inverse relation between them, i.e. S decreases with increasing σ, whereas the opposite can be said for κ_{elec}. These competing relations, which are discusses in Chapter 1, make the job of optimizing thermoelectric properties a difficult and challenging one.

2.7 Computational details

In this thesis, most of the calculations were done using the projector-augmented wave (PAW) method[75, 76] as implemented in the VASP code.[77–79] (exceptions will be noted). In all these calculations we used a plane-wave energy cutoff of 400 eV and an energy convergence criterion (between two successive self-consistent cycles) of 10^{-4} eV (total energy/unit cell). Perdew-Burke-Ernzerhof (PBE)[47] formulation was used for the exchange-correlation functional.

For comparison, the meta-GGA called modified Becke-Johnson potential (m-BJ) is also considered for some systems. These calculations were carried out using linearized augmented plane wave (LAPW) method as implemented in Wien2K[80] package, with a plane-wave cutoff parameter RKMAX=7.

For GGA+U calculations, we used the formalism proposed by Dudarev et al.[81], where the on-site repulsion and exchange are incorporated through a parameter $U_{eff} = U - J$, where U and

J are the Coulomb and exchange terms (screened) respectively. In this approach, total energy is rewritten as:

$$E_{GGA+U} = E_{GGA} + \sum_i \frac{U_{eff,i}}{2} \sum_\sigma \left[\left(\sum_{m_1} n_{i,m_1,m_1}^\sigma \right) - \left(\sum_{m_1,m_2} n_{i,m_1,m_2}^\sigma n_{i,m_2,m_1}^\sigma \right) \right] \qquad (2.95)$$

where E_{GGA} and E_{GGA+U} are the energies in GGA and GGA+U approximations, respectively; m_1 and m_2 are the orbital quantum numbers ($m = -2, -1, 0, 1, 2$ for the d states) and n_{i,m_1,m_2}^σ are the matrix elements of the density operator $\hat{n}_i^\sigma$ associated with spin σ and site i in this basis. For simplicity, hereinafter, we will refer to U_{eff} as U.

Boltzmann transport theory was used to calculate thermopower S as a function of carrier concentration (both n and p types) and temperature. For simplicity we used rigid band and constant relaxation time approximations (for a justification see a recent paper by Lee and Mahanti, Phys. Rev. B 2012) to calculate S. These calculations were done using the BoltzTrap pacakage of Madsen and Singh[68]. For accurate computation of transport velocities (and hence S) we used dense **k**-meshes (ranging from $21 \times 21 \times 21$–$41 \times 41 \times 41$ for different systems).

CHAPTER 3

HEUSLER COMPOUND – Fe$_2$VAl: EFFECTS OF ON-SITE COULOMB REPULSION

3.1   Introduction

(Full) Heusler compounds are a class of promising thermoelectric materials. They have a stoichio-metric composition with the general formula X_2YZ, where X and Y are two different transition metals (TMs) and Z is a metalloid. They crystallize in a cubic structure corresponding to the space group L2$_1$. After their first discovery by Friedrich Heusler in 1903, more and more Heusler-type alloys have been found and studied extensively.[85] Among them, Fe$_2$VAl based compounds came to the research community's attention in 1997 when Nishino et al. [82] pointed out a possible existence of d-electron heavy-fermion behaviour (commonly seen in f-electron system) in this compound. Their heat capacity measurement at low temperature (1.6-6 K) showed a linear term with a γ value of 14 mJ mol^{-1} K^{-2} from which a large electron effective mass ($10m_e$, where m_e is the free electron mass) was estimated. Photoemission spectrum showed a clear Fermi edge in-dicating metal-like characteristics. In contrast, by fitting the resistivity to an exponential function of E_g/T in the temperature range 400 to 800 K, Nishino et al. [82] found that Fe$_2$VAl behaved like a semiconductor with $E_g \approx 0.1$ eV. These experimental results are quite intriguing. This dual nature was also seen in NMR experiments by Lue and Ross [83] By measuring the T-dependence of Knight shift (K_s) and the nuclear spin relaxation time (T_1) and fitting these two quantities to functions of E_g/T, they found a band gap of 0.21-0.22 eV for K_s and 0.27 eV for T_1. Surprisingly,

Table 3.1: Summary of experimental studies of energy gap in Fe$_2$VAl

Group - year	Measured quantity	E_g (eV)
Nishino *et al.* - 1997[82]	Resistivity (400–800 K)	0.1
Lue *et al.* - 1998[83]	NMR (250–550K)	
	• Knight shifts (K_s)	0.21–0.22
	• Spin relaxation rate (T_1)	0.27
Okamura *et al.* - 2000[84]	Photo-conductivity (9–295K)	0.1 - 0.2

Table 3.2: Summary of previous theoretical studies on Fe_2VAl electronic structure

Group - Year	Method	a(Å)	E_g (eV)	$g(E_F)$ (eV^{-1}/$f.u.$)
Singh & Mazin - 1998[87]	LSDA, LAPW (LMTO)	5.76	-0.2	0.3
Weinert & Watson - 1998[88]	LDA, (FLASTO)		-0.2	–
Weht & Pickett - 1998[89]	GGA, PBE	5.76	-0.2∼-0.1	0.1
Guo et $al.$ - 1998[90]	LSDA	5.68	-0.2	0.54
Kumar et $al.$ - 2009[91]	GGA, PBE	5.712	–	0.19

in addition to the activated behaviour, they also found metallic characteristics through Korringa law. [86] Using the Korringa relation, they found a finite DOS $g(E_F)$ at the Fermi level (E_F), and estimated its V-d component to be about 1.7×10^{-2} eV^{-1} per V atom. The actual $g(E_F)$ should be somewhat larger. Okamura et al. [84] using photoconductivity measurements also reported similar results for Fe_2VAl with a band gap of 0.1-0.2 eV and a finite DOS at the Fermi level. The experimental results of the band gap and the temperature range in which they were measured are summarized in Table 3.1. Based on the transport measurements and the finite DOS at E_F, it was argued that Fe_2VAl was a semimetal with a pseudo-gap. This implies that there is a small overlap between the valence band and the conduction band. This overlap gives rise to a negative band gap $E_g = E_{c,min} - E_{v,max} < 0$, where $E_{c,min}$ and $E_{v,max}$ are the minimum of the conduction and the maximum of the valence band, respectively. However the value of this negative band gap is not known from the experiments. Note that the notation of negative band gap E_g and the positive pseudo-gap can be distinctly different.

The existence of a negative band gap E_g in the electronic structure of Fe_2VAl has been found in several density functional theory (DFT) calculations within either LDA or GGA; [87–91] a summary of these theoretical calculations is given in Table 3.2. All the LDA/GGA calculations indicate that Fe_2VAl has a well-developed negative band gap, with the valence band maximum (VBM) at the Γ point and the conduction band minimum (CBM) at the X point (Γ and X are two symmetry points in the first Brillouin Zone of a FCC lattice), coming mainly from the Fe-t_{2g} and V-e_g states, respectively. The negative band gap was found to be $-0.1 \sim -0.2$ eV, and there is

a small but finite DOS at the Fermi level, qualitatively consistent with the Korringa law and the linear T-dependence of the heat capacity at low T. However, as we will discuss later, the calculated DOS at E_F is an order of magnitude larger than that estimated from Korringa's law and an order of magnitude smaller to explain the observed large low-T heat capacity. Nevertheless, these band structure calculations also revealed that Fe_2VAl had sharp edges in the DOS near the Fermi level which is a desirable feature for a good thermoelectric, as suggested by Mahan and Sofo. [17]

Encouraged by the sharp edges in the calculated DOS of Fe_2VAl, thermoelectric properties have been studied experimentally, including our own EFRC[1] group at Michigan State University[19]. In addition, several attempts have been made to improve its thermopower S, for example by incorporating anti-site defects (increasing ratio of V/Fe) [92] or by doping at the Al site with Si, Ge, and Sn. [19, 93, 94] In the present work we will not be concerned with the V/Fe anti-site defects since they give rise to localized states near the Fermi energy and their effects on the transport properties are difficult to calculate accurately. Our focus here is to see how well one can understand the experimental data without involving the effect of defects. Experimentally it is found that nominally pure Fe_2VAl is a p-type thermoelectric (in agreement with Hall measurement. [95]) In the temperature range $T = 100 - 400$ K, S was found to be 10–50 μV/K. When Al was partially replaced by Si, Ge, or Sn[19, 93, 94], more electrons were put in the system and turned it into an n-type thermoelectric. These measurements show that the highest S (in magnitude) is about -150 μV/K, obtained for 5–6 % of Al substitution corresponding to an electron doping of 1.1–1.3$\times 10^{20}$ cm^{-3} (assuming each dopant replacing an Al donates one electron).

In spite of extensive experimental works, there is no direct spectral evidence supporting the existence of either a real or a pseudo gap in Fe_2VAl. From a theoretical prospective, there is also no systematic study of the relationship between the LDA/GGA electronic structure and thermoelectric properties in the pseudo-gap regime and how does theory compare with experiment. Furthermore, we know that LDA and GGA do not do well vis-à-vis band gaps in semiconductors due to the self-interaction error inherent in the LDA/GGA potential and vanishing of the discontinuity of the

---

[1]Energy Frontier Research Center, a project funded by the US Department of Energy

exchange-correlation potential as a function of the level occupation at E_F as discussed in chapter 2. The errors in LDA and GGA are severe in describing accurately the localized electrons in d or f states, i.e. transition metal and rare earth compounds. Whether there will be similar problems in pseudo-gap or zero-gap systems (when the overlap between conduction band and valence band is small) is not known. Recently, Bilc and Ghosez [96] used B1WC hybrid functional [57] (see table 2.1) to study Fe_2VAl. They used ratio of $\alpha = 0.16$ exact exchange and found it to be a semiconductor with a band gap of 0.34 eV. Later in this chapter I will compare this value of band gap to that obtained using LDA+U and other method as well as hybrid functional with different parameter α.

In this chapter, I explore the effect of Coulomb repulsion associated with the d-electrons of Fe and V electrons Fe_2VAl using GGA+U method (see Sec. 2.5.2), which gives quite reasonable results for relatively low computational cost. This method has been found to be quite successful in several other Heusler compounds containing d-electrons such as Co_2FeSi, Co_2MnSi. [97, 98] I systematically investigate the effect of the on-site Coulomb repulsion U at both Fe and V sites on the electronic structure and thermoelectric properties of Fe_2VAl. U was first treated as a parameter to understand how the band structure is affected by the values of U at different transition metal sites. Then the values of U were calculated using constrained DFT method (see section 2.7). The calculated band structure for these values of U then is used to investigate the carrier concentration and temperature dependence of thermopower, look for their optimum values and compare with the experiment.

The chapter is arranged as follows. In Sec. 3.2, I briefly describe the computational procedure beyond which already discussed in section 2.7. Results and discussions on electronic structure and thermoelectric properties are presented in Sec. 3.3 and Sec. 3.4. A brief summary is given in Sec. 3.5. Most of materials presented in this chapter are published in the reference [35].

3.2 Computational details

The on-site Coulomb interaction was added using GGA+U method within the scheme suggested by Dudarev et al. [81] (see section 2.5.2). The values of U for Fe and V are calculated using the constrained DFT method, where the effective Coulomb repulsion energy is given by

$$U_{eff} = \varepsilon_{d\uparrow} \left(\frac{n}{2} + \frac{1}{2}, \frac{n}{2} \right) - \varepsilon_{d\uparrow} \left(\frac{n}{2} + \frac{1}{2}, \frac{n}{2} - 1 \right)$$
$$- \varepsilon_F \left(\frac{n}{2} + \frac{1}{2}, \frac{n}{2} \right) + \varepsilon_F \left(\frac{n}{2} + \frac{1}{2}, \frac{n}{2} - 1 \right) \tag{3.1}$$

where $\varepsilon_{d\uparrow}(n_\uparrow, n_\downarrow)$ and $\varepsilon_F(n_\uparrow, n_\downarrow)$ are respectively the spin-up d-eigenvalue and the Fermi energy for the configuration of $n_\uparrow$ up-spins and $n_\downarrow$ down-spins, n is the total number of d-electrons.

Since this method of calculating U involves varying the occupation number, which is not allowed in VASP, The Wien2k package [80] was used, following the procedure suggested by Madsen and Novák. [68] A $2 \times 2 \times 2$ fcc supercell was used within PBE-GGA [47] with a plane wave cutoff RK$_{max}$=7 and a Fourier expansion cutoff G$_{max}$=9. Values of U_{eff} were found to be 4.0 and 1.5 eV for Fe and V, respectively. The value of U_{eff} for V is smaller than that of Fe as expected. Note that in the atomic limit the value of U very high. In extended systems, since the effective Coulomb interaction is screened by the cloud of electrons, the value of U is much smaller. For example, $U \approx 20$ eV for atomic Fe, whereas it is $\sim 6.2 - 6.8$ eV for Fe metal [66] and $\sim 4.8 - 7.4$ eV for Fe oxide. [68] Thus the small value of U_{eff} of Fe that we obtained suggests a strong screening effect in Fe$_2$VAl.

In this chapter, the effect of Coulomb repulsion was first investigated with various values of U on Fe and V sites separately to understand how different bands are affected by U. For this purpose three situations were consider for each atom: weak (U_{eff} =1 eV), intermediate (U_{eff} =2 eV), and strong (U_{eff} =4 eV) repulsion limits (comparing to typical d bandwidth of 1.5–2 eV). GGA+U calculations were then done with U values obtained using the constrained DFT method. In the rest of this chapter the suffix "eff" will be omitted from U_{eff}.

Thermopower S was calculated using Boltzmann transport equation in constant relaxation time and rigid band approximations. [74] Since Fe$_2$VAl is a cubic system, its transport tensors are
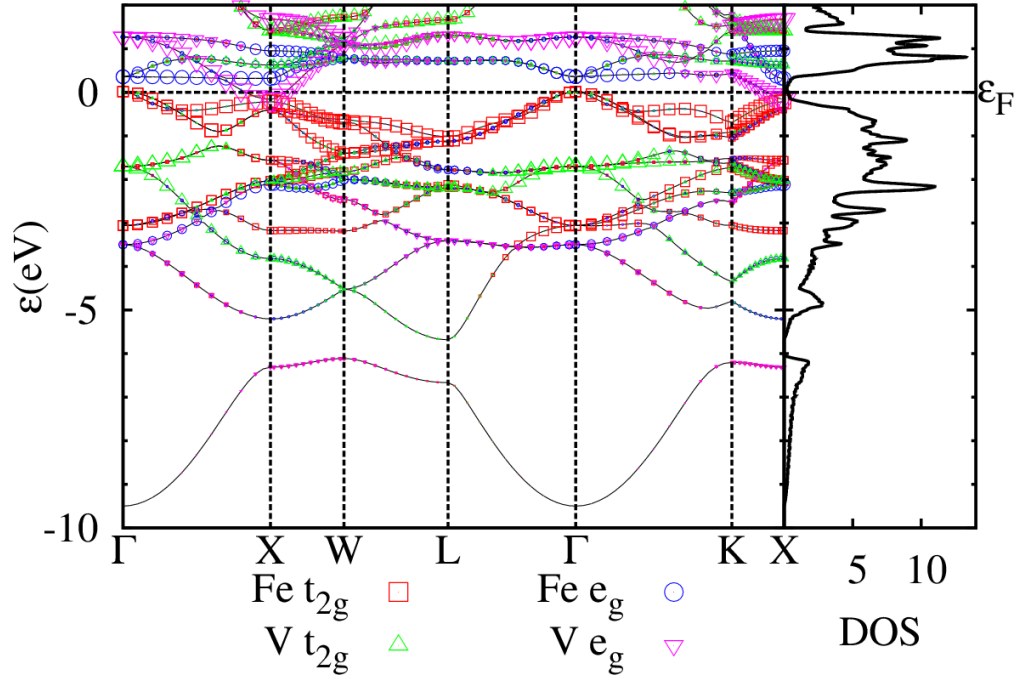
Figure 3.1: Band structure of Fe_2VAl showing *d*-characters of Fe and V (left); and DOS (right). E_F denotes the Fermi level set to be zero. The size of the symbols represents the strength of orbital characters.

diagonal and all the diagonal elements are the same and electrical conductivity σ and thermopower (Seebeck coefficient) *S* are given by Eqn. 2.91 and 2.92 respectively. Here $\tau(n, \vec{k})$ is assumed to be constant. The energy dispersion was first obtained with Monkhorst-Pack mesh of $41 \times 41 \times 41$ **k**-points, then the transport coefficients were calculated from the resulting eigenvalues employing the Boltztrap code developed by Madsen and Singh. [74] As mentioned earlier, this chapter discusses only the thermopower *S*.

3.3   Electronic structure: Pseudo-gap versus real gap

In Fig. 3.1 (left panel) the energy bands were shown together with Fe- and V-*d* characters along different symmetry directions of the first BZ. The right panel gives the DOS of Fe_2VAl which clearly shows a pseudo-gap structure near E_F. The zero of energy has been chosen to be at the Fermi level. The present GGA band structure results agree with the previous GGA calculations of other groups [87–91] in which Fe_2VAl has a negative band gap of $E_g \sim -0.17$ eV. Certain general

features of the band structure are the following: It has a deep and rather broad Al s-band from -10 to -6 eV. Note that here 0 eV is assumed at Fermi level. The bands from -5 to 2 eV result from the hybridization of Fe and V d-orbitals with a small admixture of Al p-orbitals (only Fe-d and V-d characters are shown in Fig. 3.1). The pseudo-gap is formed by a nondegenerate V-e_g band minimum at the X point and a three-fold degenerate Fe-t_{2g} band at the Γ point. Near 0.3 eV there is a very narrow band originating from Fe-e_g states which gives rise to a sharp edge in the conduction band DOS. These Fe- and V-d bands are important features which are relevant to the low-energy physics in general and the thermoelectric properties in particular. Weht and Pickett [89] suggested that the excitonic effect may be important in this region.

The band structure of Fe$_2$VAl near the Fermi-level shows that there are three-fold degenerate hole pockets centered around the Γ point with nearly same effective mass and a nondegenerate electron pockets centered around the X points. Since there are three inequivalent X points in the BZ this compensates for the 3-fold degeneracy of valence band when one compares the contributions from holes and electrons to the thermopower. The calculated DOS at the Fermi energy for the undoped system is 0.27 eV^{-1} per formula unit (f.u.). This gives a γ value for the linear heat capacity of 0.63 mJ mol^{-1} K^{-2}, nearly the same as 0.69 mJ mol^{-1} K^{-2} reported by Guo et al. [90] in their LSDA calculation. The small difference between the two theoretical values may be due to the different lattice constants and different methods which have been used. However, both these values are an order of magnitude smaller than the experimentally measured low-T γ value of 14 mJ mol^{-1} K^{-2}.[82]

As seen in Fig. 3.1 (right panel), there is a rapid rise in the DOS near 0.3 eV (in the conduction band) and a similar one but less rapid at -0.2 eV (in the valence bands). As we will discuss later, one obtains large values of S (magnitude) when Fe$_2$VAl is heavily doped, either n-type or p-type, so that the chemical potential approaches these rapidly increasing parts of the DOS. This result is expected, as already discussed in section 1.2.

When the on-site Coulomb repulsion U is turned on, as one would expect (see Chap. 2) the occupied d-states are pushed down in energy whereas the unoccupied states are pushed up. This
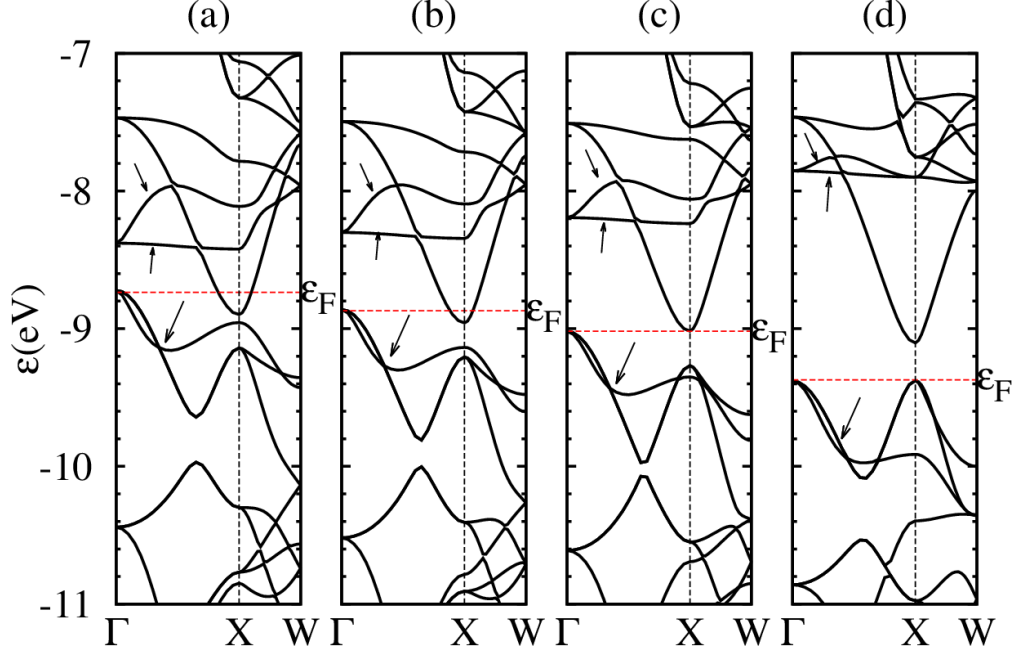
Figure 3.2: Band structure of Fe_2VAl in absolute scale for U_{Fe} of (a) 0 eV, (b) 1 eV, (c) 2 eV and (d) 4 eV. The Fe-e_g and Fe-t_{2g} bands are pointed out by arrows.

is clearly seen in Figs. 3.2 and 3.3. In order to see how different bands change due to the on site Coulomb repulsion, the bands structure was plotted in the absolute scale focusing on the bands near the Fermi level in the range from -11 to -7 eV. Fig. 3.2 shows the bands structures with U_{Fe} =0,1, 2, and 4 eV at the Fe site only. In this case V bands are relatively unaffected while the unoccupied Fe-e_g bands are pushed up and the occupied Fe-t_{2g} bands are pushed down. For a quantitative measure of the effect of U_{Fe}, we define a quantity $\Delta_{e_g,t_{2g}}$ which is the splitting between the Fe-e_g conduction band and the Fe-t_{2g} topmost valence band at the Γ point. The value of $\Delta_{e_g,t_{2g}}$ changes by 0.22, 0.48 and 1.18 eV for U_{Fe}=1, 2, and 4 eV, respectively. As expected, the larger the value of U_{Fe}, the larger is the change in the energy difference. However, the changes in the energies are about 22∼30 % of the values of the parameter U_{Fe}. This is due to the hybridization of Fe-d, V-d and some Al-p orbitals, which weakens the effect of U. In the weak repulsion regime, the parameter U_{Fe} has very small effect on the band gap. In the intermediate and strong repulsion cases the effects are significant. The relative shift of the bands results in changing the pseudo gap to a real gap. For $U_{Fe} = 1$ eV the pseudo-gap remains while the values of the band gap are

0.002 eV and 0.27 eV corresponding to $U_{Fe} = 2$ eV and 4 eV, respectively.

Looking more carefully at the changes in the band structures (see Fig. 3.2), one can point out an interesting change in Fe-t_{2g} bands at the X point. In the absence of U_{Fe}, the t_{2g} bands of Fe splits into two levels, where a nondegenerate band is located at ≈ 0.15 eV above the two-fold degenerate one. Note that the nondegenerate band consists of Fe-t_{2g} only while the two-fold degenerate band shows strong hybridization, with a small contribution of Fe-t_{2g} and large contribution of p-like plane-wave states. On the other hand, at the Γ point, the VBM is 3-fold degenerate coming from hybridization of Fe- and V-t_{2g} orbitals. In the presence of U_{Fe}, the bands without hybridization are strongly affected by U_{Fe}, whereas the bands with stronger hybridization, specially when p states are involved, are not affected much by U_{Fe}. This results in the change in the ordering of these levels (at X and Γ) when U_{Fe}=4 eV. The nondegenerate band is pushed down more strongly than the two-fold degenerate one. As a consequence, when U_{Fe}=4 eV, reversed ordering of these levels is observed at the X point, i.e. the two-fold degenerate Fe-t_{2g} band becomes the highest occupied band. This makes the system a direct band gap semiconductor and also brings more hole pockets into the system even with small doping levels. This would make Fe$_2$VAl a better p-type thermoelectric (which will be discussed in detail later in this chapter). Similar effect is also seen in Fe-e_g conduction bands. Without U_{Fe}, at the X point, the second and fourth lowest-energy bands have pure Fe-e_g character while the third one is a hybridized band of Fe-e_g and V-t_{2g}. By turning on the Fe-site Coulomb repulsion, the energy difference between the second and fourth bands remain nearly the same, whereas that between the second and third bands is decreased.

Analogous band shifting is seen when we turn on the Coulomb repulsion at the V site only: The Fe bands remain nearly unchanged whereas the V-e_g bands, since they are mainly unoccupied, are shifted upwards (shown in Fig. 3.3). There is however a difference in the way V d-bands react when we include U effect on the V site. The V-e_g bands, most of which lie above the Fermi level, is affected strongly by U_V since it is predominantly of V-e_g character. The energy of this band is changed about 13–20 % of the U_V value. On the other hand, the occupied bands which hybridize with Fe-t_{2g} are shifted by less than 1 % of the U_V value (Note that U_{Fe}=0). In the case when one
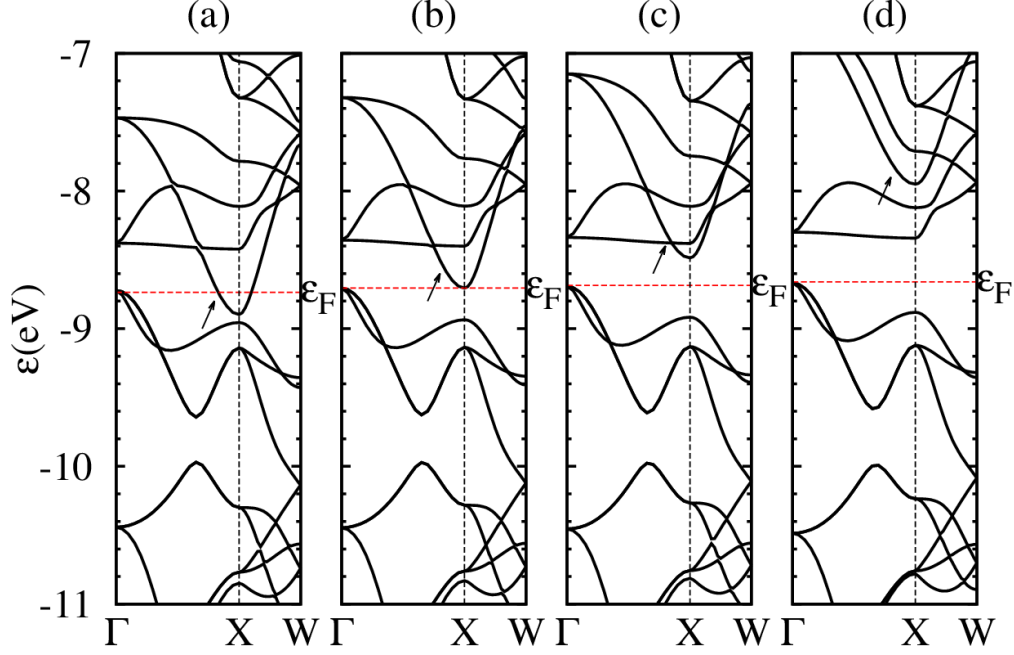
Figure 3.3: Band structure of Fe_2VAl in absolute scale for U_V of (a) 0 eV, (b) 1 eV, (c) 2 eV and (d) 4 eV.The V-e_g bands are pointed out by an arrow.

considers U_V at the V site only, even a weak repulsion causes a significant change in the band gap. For U_V=1 eV, Fe_2VAl becomes an almost zero-gap system; for U_V=2 eV there is a real gap of 0.21 eV; when U_V=4 eV the V-e_g band is pushed up so much that the flat Fe-e_g band becomes the lowest conduction band and the gap is now 0.32 eV.

When we turn on U at both Fe and V sites the net effect appears to be roughly a combination of individual Fe and V effects. For the U values obtained from constrained DFT as described in Sec. 3.2 (U_{Fe} =4 eV and U_V =2 eV), the calculated band structure is shown in Fig. 3.4(b). A band gap of 0.55 eV is obtained and it is both direct and indirect since the highest occupied states at the Γ and the X points are nearly degenerate (as discussed in the case U_{Fe} =4 eV above).

As mentioned in Sec. 3.1, several improvements beyond LDA/GGA have been done to take better account of localized d-electron systems. Here I compare the results obtained using different approximations including improved GGA by Engel and Vosko [49], hybrid functional: PBE0, [58], HSE06[59–61] and B1WC [57] as well as the recently propose modified Becke-Johnson (mBJ)[52] which is claimed to give good band gap values which agree well with those obtained using the GW
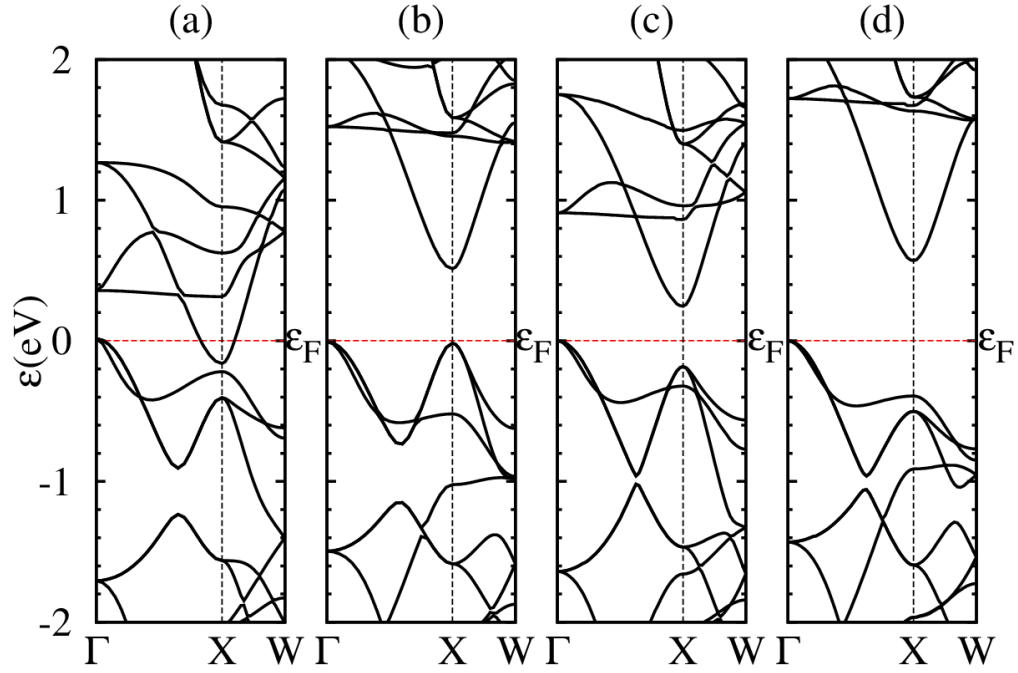
Figure 3.4: Band structure of Fe_2VAl obtained in different methods: (a) GGA-PBE , (b) GGA+U , (c) mBJ and (d) PBE0.

mBJ and PBE0 bands structures were calculated with Wien2K

Table 3.3: Summary of Fe_2VAl band gap using different methods

Method[*]	Parameter	Band gap (eV)
GGA–PBE	–	-0.17[†]
GGA–EV	–	-0.06[†]
mBJ	–	0.22[‡]
GGA+U	$U_{Fe} = 4\,\text{eV}, U_V = 1.5\,\text{eV}$	0.55[†]
PBE0	$\alpha = 0.25$	0.58[‡]
		1.8[†]
HSE06	$\alpha = 0.25,\ \omega = 0.2$	1.1[†]
B1WC	$\alpha = 0.16$	0.34[⊥‡]
	$\alpha = 0.25$	0.62[‡]

[*]For detailed discussion on methods of calculations see Sec. 2.5.3 and table 2.1

[†]Calculated with VASP

[‡]Calculated with Wien2K

[⊥]Reference [96]

method. [71] The summary of methods and corresponding band gaps are given in Table 3.3 and the band structures obtained from some of these methods are shown in Fig. 3.4. Note that some of the results were calculated using Wien2k [80] package (see table 3.3).

We found that both PBE0 and B1WC which are implemented in Wien2K with $\alpha = 0.25$ give quite large band gaps, 0.58 and 0.62 eV, which are very close to our GGA+U result. On the other hand, PBE0 implemented in VASP gives a really large band gap of ~ 1.8 eV. With VASP, when the exact exchange is screened, i.e. as in HSE06, the obtained band gap is reduced to $\sim$1.1 eV, which, however is still twice of that calculated with Wien2K hybrid functional. Note that GGA results agree extremely well between the two DFT codes. This brings up a questions of how non-local exchange is implemented in those programs and how to critically validate the large number of electronic structure codes which are handily available.

Reducing the value of α to 0.16 in B1WC method results in the band gap of 0.34 eV. These values are, however, larger than that obtained from mBJ method which gives 0.22 eV (in reasonable agreement with experimental band gap). It is important to mention that mBJ method, among all the methods we have tried, gives the energy level ordering at the X point very similar to that of seen in the GGA+U calculation. However the change in the band structure seen in mBJ (compare to GGA calculation) is not as large as that seen in GGA+U. Hence the top of the valence band is still at the Γ point and the band gap is indirect in the mBJ band structure.

If mBJ method indeed gives the right band gap for Fe_2VAl and this compound is an intrinsic narrow band gap semiconductor then the large gap (0.55 eV) obtained from GGA+U calculation suggests that the constrained DFT method proposed by Anisimov and Gunnaarsson overestimates the value of U, at least in these ternary compounds with small band gaps. In their method, Anisimov and Gunnarsson only considered the screening from s and p electrons and neglected the effect of d electrons themselves. This might underestimate the screening effect on U because small band gap in this system involves excitations of d-electrons. Suppression of these excitations will tend to give large U values. Having noted this shortcoming of the present U calculations smaller values of U have been checked. Results show that mBJ result could be reproduced by GGA+U with
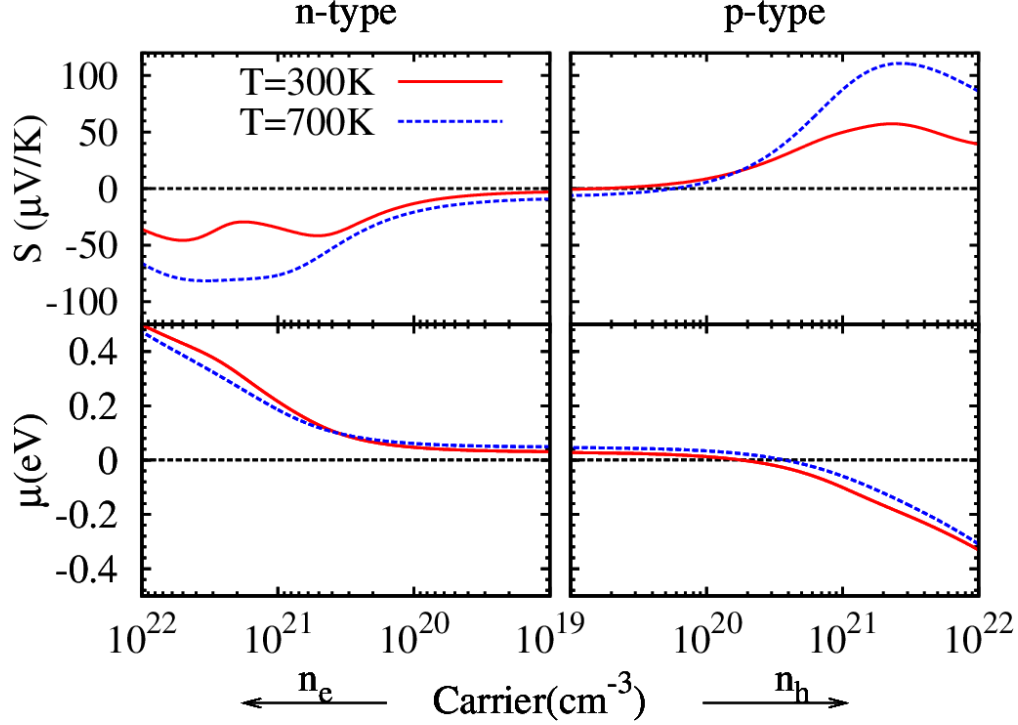
Figure 3.5: Thermopower (S) and chemical potential (μ) versus carrier concentration (n_e, n_h) in the absence of U (the pseudo-gap case) for n- and p-type doping in Fe_2VAl. The Fermi level is chosen to be 0.

U_{Fe}=3 eV and U_V=1 eV. The similarity in the results obtained from mBJ and GGA+U calculation is worth a further study.

3.4 Thermoelectric properties

Thermopower S was calculated using Eqns. (2.91) and (2.92) for different doping levels (different concentrations) and for different temperatures (T) in the range 100–700 K.

3.4.1 GGA calculation

First let us consider the case when U=0 eV (GGA calculation). This corresponds to the negative gap or pseudo-gap picture in which Fe_2VAl is a semi-metal with a small but finite DOS at E_F. In the absence of any doping the electron concentration (n_e) and hole concentration (n_h) are the same. We define the carrier concentration as $n = \frac{1}{V}(N - \int_{-\infty}^{+\infty} D(\varepsilon)f_0(\varepsilon)d\varepsilon)$, where N is the total

number of electrons in the system, V is the volume, $D(\varepsilon)$ is the density of states and $f_0(\varepsilon)$ is the Fermi-Dirac distribution function. The sign of n corresponds to the sign of the charge of the carriers. $n_e = -n$ when n is negative and $n_h = n$ when n is positive. With this definition, carrier concentration is equivalent to the doping level in the experiment. We change n by changing the chemical potential and see how S changes with n, and T. Fig. 3.5 shows thermopower (S) and chemical potential (μ) as a function of n for two different temperatures, 300 K and 700 K. Although the magnitude of S increases with T, the higher the T, the smoother is the variation of S with n, caused by enhanced thermal broadening of the Fermi distribution function (see Eqn. 2.92). The magnitude of S has two peaks for n-type doping, the first one at $n_e \approx 5.1 \times 10^{20}$ cm^{-3} and the second at $n_e \approx 5.0 \times 10^{21}$ cm^{-3}. For p-type doping there is only one peak at and $n_h \approx 2.3 \times 10^{21}$ cm^{-3}. These three concentrations correspond to the chemical potential of 0.13, 0.43, and -0.18 eV, respectively.

We can understand these peaks in magnitude of S by analysing the band structure of Fe$_2$VAl. Let's first understand the n-type thermopower as a function of n. Without doping the chemical potential lies in the overlap region between conduction band and valence band (see Fig. 3.4-(a)). In this region the hole and electron contribution in S cancel each other resulting in very small magnitude of S following the equation $S = \frac{S_e \sigma_e + S_h \sigma_h}{\sigma_e + \sigma_h}$, where S_e, σ_e and S_h, σ_h are thermopowers and electrical conductivities associated with the electrons and holes, respectively. When n_e increase, the chemical potential increases and eventually gets out of the overlap region at ~0.13 eV. As a result, the hole-electron cancellation is suppressed. The suppression of hole-electron cancellation gives rise to the first peak in the n-type S. The second peak in n-type S is obtained when n is high enough for chemical potential to reach the flat band of Fe at 0.43 eV. At this point the magnitude of S gets a large value due to the rapid change in DOS.

Similarly, one can see that the peak in p-type S is due to both suppression of hole-electron cancellation effect and the rapid rise in DOS near -0.18 eV. The coincidence of the two events: getting out of the overlap region and reaching the rapid rise in DOS is the reason why there is only one peak in the magnitude of p-type S.
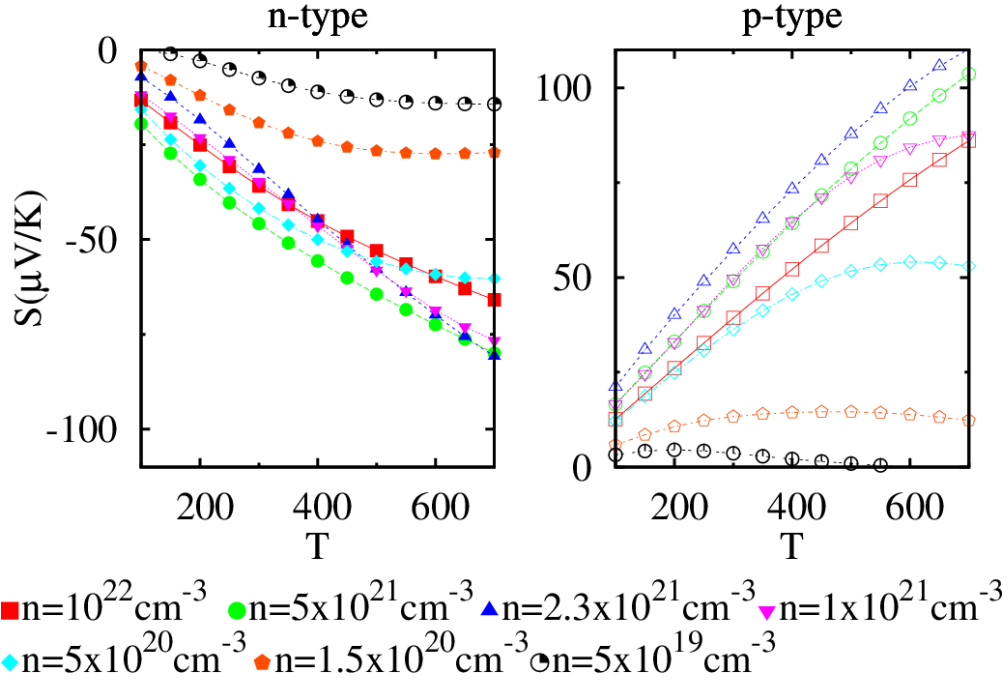
Figure 3.6: S as functions of temperature obtained using the GGA band structure (U=0 eV, the pseudo-gap case) at different concentrations: for n-type (closed symbols) and p-type (open symbols) doping.

It appears from these results that if the band structure of Fe_2VAl is adequately described by LDA or GGA, i.e. it is a pseudo-gap system, then to have large thermopower values one has to go to rather high doping levels when the cancellation effects are nearly absent. However, the carrier concentrations should not be so large that Pauli suppression for degenerate carriers start to reduces $|S|$.

Now let us look at thermopower as a function of temperature. Fig. 3.6 plots S versus T for several carrier concentrations. We will consider n- and p-type dopings separately.

n-type doping: In the temperature range 100–700 K, S has the highest value (magnitude) for $n_e \approx 4 - 6 \times 10^{21}$ cm^{-3}. The magnitude of S increases with T, but the increase is rapid at low T and then slows down at high T. At high T, large number of electron and hole excitations start to dominate, resulting in a cancellation and reduction in S, as seen in figure 3.6 where $T > 700$ K). This electron-hole cancellation is also the reason for small magnitude of S values seen for small n.

p-type doping: One sees behaviour similar to the n-type doping. Again S increases with T and

has small values for low concentrations due to electron-hole cancellation. S is largest (100 μV/K) for $n_h \approx 2 \times 10^{21}$ cm^{-3}. Interestingly, GGA calculation shows that Fe$_2$VAl is a slightly better p-type thermoelectric than n-type. For example, at 700 K, the highest value of the magnitude of S is 110 μV/K for p-doping whereas it is only 80 μV/K for n-doping, about 30 % smaller. To understand this difference we look at the band structure. The electron pockets center around the X points and are non-degenerate (ignoring spin degeneracy), whereas the hole pockets center around the Γ point but are three-fold degenerate. Since there are three inequivalent X points in the BZ and only one Γ point, the difference in the S value cannot be ascribed to the band degeneracy. We believe it is due to the difference in the effective masses of electrons and holes. The Fe dominated holes have larger effective mass and lead to larger S values. This property of the Fe$_2$VAl is different from that of ZrNiSn,[99] which belongs to the class of so called Half-Heusler compounds. In the latter compound the electron pockets centered around the X points are heavier than the hole pockets centered around the Γ point. Consequently, the magnitude of the thermopower is larger for the electrons in ZrNiSn.[99] For more discussions on this compounds see chapter 5.

3.4.2   GGA+U calculation : the effect of finite band gap

As we have discussed earlier, the effect of incorporating U is to decrease the overlap between the valence and the conduction bands and eventually open up the gap. For U_{Fe}=4 eV and U_V=1.5 eV (values calculated using constrained DFT), the band gap is 0.55 eV. For the calculation of the transport coefficients we choose the zero of energy at the middle of the gap. In Fig. 3.7 we give the results of S as a function of T for different values of the concentration. The T-dependence of S for the case of real gap is much simpler compared to the pseudo-gap case. Since there is very little electron-hole cancellation, S follows the Pizarenko relation, i.e. the magnitude of S increase with decreasing carrier concentration. Thus, increasing carrier concentration reduces the magnitude of S. And for the same reason S does not saturate up to 700 K as the thermal excitations of electrons and holes are suppressed due to the large band gap.

   As mentioned above, in the presence of U, valence band maxima near Γ and X points become
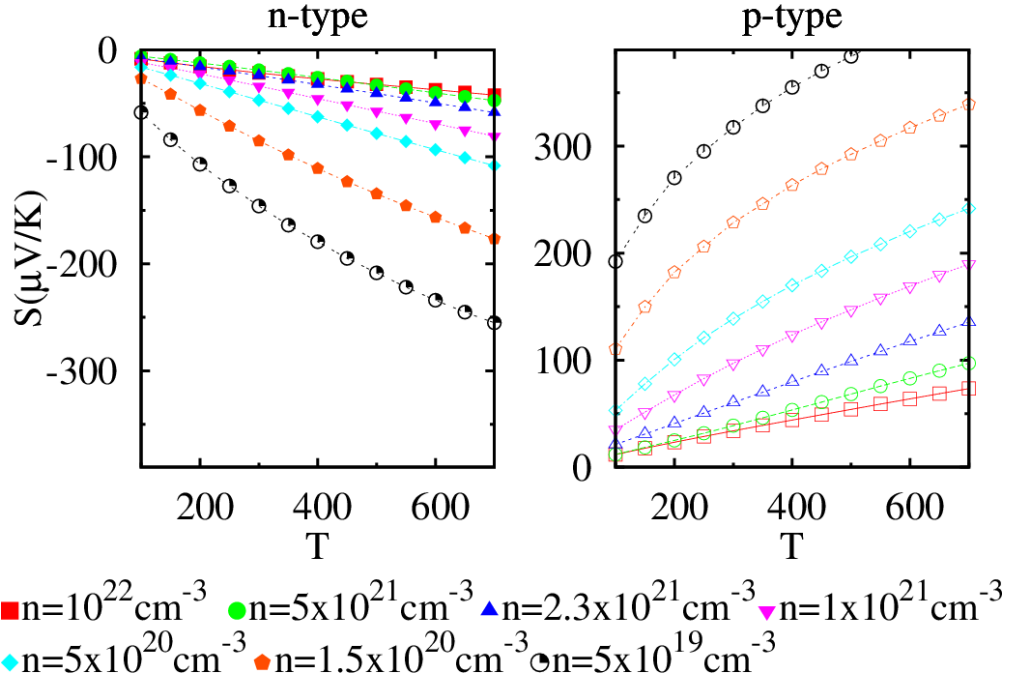
Figure 3.7: *S* as functions of *T* for GGA+U calculation ($U_F e$=4 eV and U_V=1 eV) at different concentration: for *n*-type (closed symbols) and *p*-type (open symbols) doping.

nearly degenerate. Since more hole pockets contribute to transport (both at the Γ and X points) (see Fig. 3.4(b)) we found that opening up of the gap by *U* leads to a better *p*-type thermoelectric. The value of *S* for the *p*-type at concentration of 5×10^{19} cm^{-3} at 700 K is about 3/2 times larger than that for the *n*-type at the same carrier concentration and temperature.

3.4.3 Comparison with experiment and other theoretical results

For comparison, the theoretical results are compared to the experimental results on $Fe_2VAl_{1-x}Ge_x$ by Nishino et al. [93] and $Fe_2VAl_{1-x}Si_x$ by Skoug et al. [19] for *x* values in the range 0.0–0.2. Although these two systems are similar and show qualitatively similar behaviours, there are quantitative differences which might help us in testing our theoretical calculations, particularly the adequacy of the pseudo-gap (or semimetal) picture.

Let us first look at the nominally undoped system (*x*=0). Both experiments show *p*-type behaviour in the temperature range 100–400 K. *S* of nominally undoped system increases slightly with *T* and saturates between 300–400 K. The values of *S* at 300 K, however, differ by nearly a
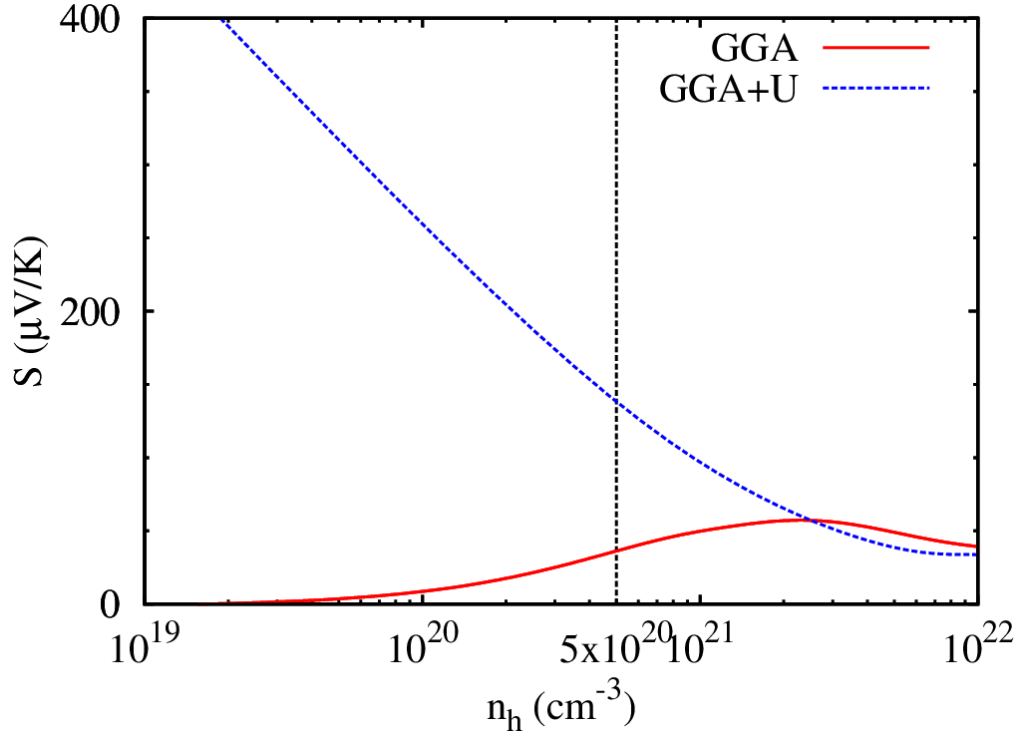
Figure 3.8: Calculated *p*-type *S* as a function of *n* for the cases of: pseudo-gap (GGA calculation) (solid line) and gapped (GGA+U calculation), E_g=0.55 eV, (dashed line) at 300 K.

factor of 2 between the two measurements (25 and 50 μV/K obtained by Nishino *et al.* and by Skoug *et al.* respectively). One can argue that this difference can be due to the difference in the hole concentrations and the small values of *S* can be understood within the pseudo-gap model when the hole concentration lies between 10^{20}–10^{21} cm^{-3}, because in this model, the electron–hole cancellation effect makes *S* to be not only small in magnitude but also a weak function of carrier concentration over a wide range. (see Fig. 3.8). In contrast, for a finite gap case (especially for a large gap 0.55 eV as obtained in the GGA+U calculation) one can not understand the peak in *S* because *S* follows the Pizarenko relation and changes rapidly as the function of carrier concentration (see Fig. 3.8). From Hall measurement done by Nishino *et al.* [95], the hole concentration for the nominally undoped sample is found to be $\approx 5 \times 10^{20}$ cm^{-3}. For this concentration the GGA+U band structure gives $S \approx 140 \mu V/K$ at 300 K, which is about two times larger than the experimental values (25 and 50 μV/K), while GGA band structure gives $S \approx 30 \mu V/K$ in quite good agreement with experiment. This result would then favour the pseudo-gap or semimetal picture. Physically,

61

this means that when the hole concentration is not too large, small S values can be obtained near 300 K only when there is significant electron-hole cancellation.

When one replaces Al by Ge, Si, or Sn, the dopants give an extra electron/dopant to the network and when $x > 0.03$, the alloys show n-type behavior. One significant feature in the n-type compounds studied by both Nishino and Skoug's groups is that for the optimum doping ($x \approx 0.05$–0.06), S shows a minimum between 200–250 K and the value of S near the minimum is about -150 μV/K[19, 93]. For larger x (presumably for larger carrier concentration), the minimum moves towards higher T.

Studying S as the function of T corresponding to the pseudo-gap case (U=0) (Fig. 3.6), we found that that for the entire range of electron concentration $n_e \approx 5 \times 10^{19} - 10^{22}$ cm^{-3}, there is no discernible minimum in S at temperature lower than 500 K and also the magnitude of the S values are less than 60 μV/K (two times smaller than the experimental values) in the temperature range 100–700 K. Both these observations are in disagreement with experiments. So neither the pseudo-gap model nor the model with large band gap ($\sim$0.55 eV) can explain the observed minimum in S at $T \sim 250K$ and its magnitude.

In an attempt to see if a finite gap picture could explain the experimental data I have tried using smaller values of U than that obtained from the constrained DFT calculation. We found that with very small U ($\approx$1 eV) (and almost zero band gap, $E_g \approx 0.07eV$) we could qualitatively reproduce the experimental data of S for the n-type system, particularly the minimum at $\sim$ 250 K (see Fig. 3.9). However in order to get such an agreement with experiment one has to use $n \approx 5 \times 10^{19}$ cm^{-3} which is about one order of magnitude smaller than that obtained from the Hall measurement.[93] For the p-type (nominally undoped) system with hole concentration of 5×10^{20} cm^{-3} (obtained from Hall measurement[93]) the magnitude of S is roughly of the order of the experiment done by Skoug et al. However, S does not saturate in the range 0–700 K.

The above analysis shows that it is difficult to understand the experimental data for both the nominally undoped and n-doped cases using either the pseudo-gap or the real gap model. This conclusion agrees with the work of Bilc and Ghosez [96]who used B1WC hybrid functional
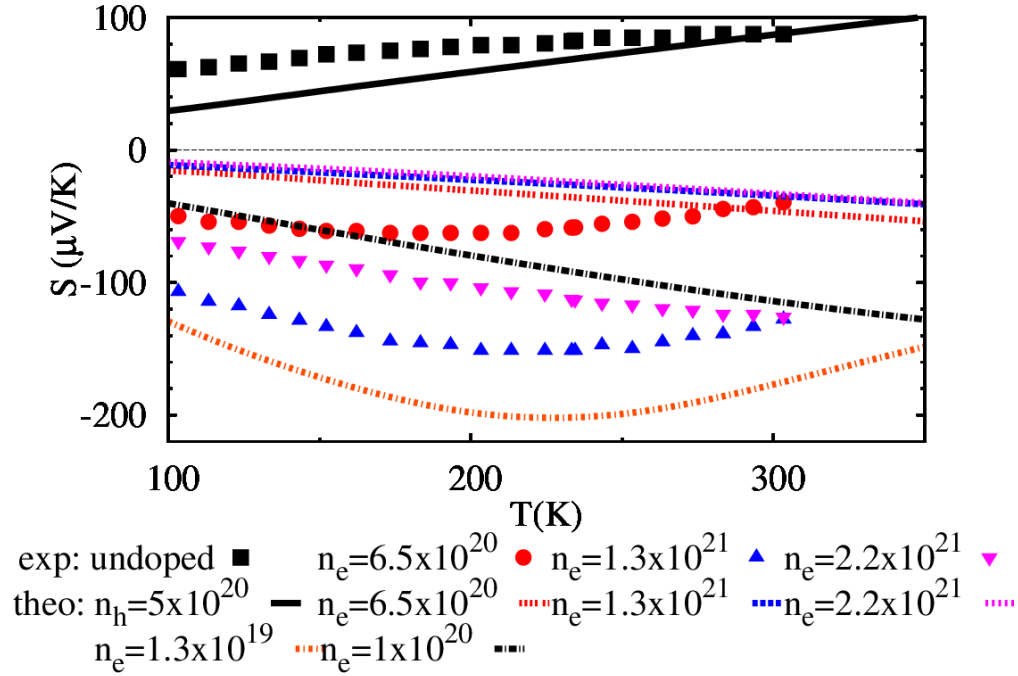
Figure 3.9: Experimental thermopower obtained by doping Si on Al site (symbols) (by Skoug et al. [19]) and theoretical curve (lines) with U=1 eV ($E_g = 0.07\ eV$). (carrier concentrations are given in unit of cm^{-3})

method [57] and found a band gap of about 0.34 eV which lies between our value of 0.55 eV and the experimental value of about 0.2 eV. With this value of band gap they could not reproduce the experimental data. So just scaling the gap to a small value cannot explain the n,T-dependence of S. In order to understand the difference between experiment and theory, one has to overcome several weaknesses of the present calculations.

First, the effect of inter-site Coulomb repulsion between d-electrons at neighbouring V- and Fe-sites has not been included within the present GGA+U approach. Also, GGA+U is essentially a mean-field approximation, and does not include electron-hole excitonic correlations which may alter the electronic states near the Fermi energy in the pseudo-gap or small gap regime. Second, we have used a rigid band model to calculate S. It is possible that the dopants distort the electronic structure near the Fermi energy and hence the rigid band model is not valid any more. [100] Third, there may be defects (Fe-V antisite defects, vacancies, and interstitials) which alter the states near the Fermi energy, giving rise to not only new (and perhaps smaller than the band gap) excitation

energy scales but also to localized states that act as carrier traps.

3.5 Summary

In this chapter I have discussed how the band structure of Fe_2VAl changes when one takes into consideration the effect of intra-site Coulomb repulsion between d-electrons at the Fe and V sites beyond GGA using GGA+U approximation. In Heusler compounds, which contain two different types of transition metal atoms, the effect of U on the band gap depends sensitively on which one of the two transition metal sites one is dealing with. For example, even small values of U_V ($\sim$1 eV) at the V site can open up the gap because the lowest conduction band is predominantly V d-character and gets pushed upward in energy strongly by U_V. In contrast, small values of U_{Fe} ($\sim$1 eV) at the Fe site do not open up the gap, it rather changes the band structure slightly. This is because the top of the valence band is strongly hybridized and is shifted downwards in energy only slightly. Thus one needs a larger value of U_{Fe} ($\sim$2 eV) at the Fe site to open the band gap when $U_V = 0$.

The values of U calculated using constrained density functional theory (U_{Fe}=4 eV for Fe and U_V=1.5 eV for V) are much smaller than the atomic values of U ($\sim$20 eV) indicating a strong screening effect. This is not surprising and is seen in many transition metal compounds. What surprising is that the values which have been calculated for Fe is smaller than that one finds in Fe metal ($\sim$6 eV) since the screening should be stronger in the metal.

Using the values U_{Fe}=4.0 eV and U_V=1.5 eV give a gap of 0.55 eV in Fe_2VAl, considerably larger than that obtained from transport measurements and NMR ($e_g \approx 0.2\ eV$). In this case, S shows characteristics of usual narrow band-gap semiconductor. Both GGA and GGA+U calculations suggest that Fe_2VAl is a better p-type thermoelectric either due to larger hole effective mass (in GGA) or due to large degeneracy (in GGA+U).

Calculations, however, point out that the present models (both pseudo and real intrinsic gap cases), cannot explain all the experimental data on S consistently for both n- and p-doped cases. Band structure calculated using modified Becke-Johnson potential tend to give small band gaps

(0.22 eV). But these results are still not enough to explain the thermopower data. Several limitations of the present models, such as the electron-hole (excitonic) correlation effects, defect induced changes in band structure, etc. , were pointed out and further work should be done.

CHAPTER 4

DIAMOND-LIKE TERNARY COMPOUNDS

4.1 Introduction

Among approaches to improve ZT, reducing lattice thermal conductivity is considerably less complicated (discussed in Sec. 1.1), in the sense that it does not involve other parameters (namely, S, σ, and κ_{elect}). This direction has been quite successful, bringing ZT to the current state of 2–3.[14, 101] One way to reduce thermal conductivity is to increase the number of atoms in a unit cell, following the work of Slack and his colleagues[26] which suggested that thermal conductivity is inversely proportional to the number of ions per unit cell

$$\kappa_{latt} = \frac{B\bar{M}\delta\theta_D^3}{n^{2/3}T\gamma^2},\tag{4.1}$$

where B is a constant, $\bar{M}$ is the average atomic mass, δ is the average volume per atom, θ_D is the average Debye temperature, T is the temperature, n is the number of atoms per unit cell and γ is the Grüneisen constant.

For diamond-like (tetrahedrally bonded) compounds, Grimm and Sommerfeld's rule[102] provides a simple way to search for compounds with greater number of atoms per unit cell. The rule predicts that systems with the average of four valence electrons per atom will have diamond-like structure where all atoms are tetrahedrally coordinated. Applying this rule, one can start from the multiple unit cells of a simple system (say, Silicon) and replace one constituent with two or more of different types, keeping the same average number of valence electrons. For example, we can double the unit cell of Si and then replace two Si by one Zn and one Se to get sphalerite ZnSe (zincblende/wurtzite structure). Similarly, starting from ZnSe with zincblend structure, one can double the unit cell to $(ZnSe)_2$, keep the Se sublattice intact, and replaces two Zn (divalent – II) atoms by Cu (monovalent – I) and In (trivalent – III) to get the chalcopyrite structure. Another example is to triple the ZnSe unit cell and replace the three divalent anions by two monovalent and

66

one tetravalent cations, Cu_2GeSe_3 (in general I_2-IV-VI_3).

While most of diamond-like compounds have been extensively studied for their photovoltaic application due to this wide band gaps, such as $CuInSe_2$[103] which has a band gap of 1.032 eV,[104] recently several Cu-Sb-Se(S) based ternary compounds have been found to exhibit promising thermoelectric properties. [27, 28, 105–109] Among these, Cu_3SbSe_4 (Se4) is a narrow band gap semiconductors [109–111] which gives a large p-type thermopower. [106] Even though several theoretical studies have been done on this compound,[109–111] its electronic and thermoelectric properties are not well understood. In my work, I will be concerned with Se4 and the related systems in the class of I_3-V-VI_4 compounds, where the unit cell is quadruple of ZnSe and 4 divalent cations are replaced by 3 monovalent (Cu,Ag) cations and one pentavalent (P, As, Sb, Bi) cation. The I_3-V-VI_4 compounds are classified into the family of famatinite (Fa) and enargite (En) which have tetragonal and orthorhombic structures respectively.

Tetrahedrally coordinated semiconductors have been studied extensively and have played an important role in our understanding of the relationship between coordination, bonding, and band gap. This relationship is easy to understand in monoatomic covalent solids C, Si, Ge, Sn. In these solids spatially directed sp^3 hybrids form bonding (B) and antibonding (AB) bands.[112, 113] Electrons fill up the bonding bands (valence bands) following the simple Lewis octet rule[114, 115], the antibonding bands (condution bands) are empty, there exists a band gap (E_g) between the valence band maximum and the conduction band minimum. There is a decrease in the splitting between the bonding and anti-bonding bands due to increase in the lattice constant as one goes from C to Sn, with a concurrent reduction in the band widths. The net result is a decrease in E_g which is nearly zero for Sn. Although this qualitative relationship between bonds and band gap is useful, the actual value of E_g depends on other subtleties like the details of band dispersion, spin orbit interaction etc.

The inter-relationship between bonds, bands and band gaps discussed above can be extended to tetrahedrally bonded III-V and II-VI binary compounds.[112, 113] Here again the octet rule plays the dominant role. However the splitting between the valence and the conduction bands and

therefore the band gap depends on other parameters, namely the differences in electron affinity (EA) and ionization energy (IE) of the two components. The bonds now pick up both covalent and ionic characters. The classic works of Pauling[112] and Phillips[113] in relating the ionicity and covalency of a particular bond to the above parameters (Pauling) and to the dielectric properties (Phillips) have given a fundamental understanding of the bonding and structure of these binary compounds. However, these theories do not explicitly address the relationship between band gaps and the nature of bonds. (Phillips ionicity scale does depend indirectly on the band gap through the dielectric constant). The general trend seen in covalent semiconductors, i.e. decrease in E_g with increasing lattice constant (bond length) is also seen in binary tetrahedrally bonded semiconductors. For example $E_g = 6.2$ eV in BN (lattice constant a=0.361 nm) and 0.23 eV in InSb (a=0.648 nm). Although this tendency is quite general the actual values of the band gap depends on the details of band dispersion. Progress in the in electronic structure theories (*ab-initio* DFT both local and non-local, GW, and others) have helped us in addressing the relationship between bonding, band structure and band gaps in these compounds.[38]

Extending the above ideas further to tetrahedrally coordinated ternary compounds, in this case, Fa and En compounds, becomes challenging because of the competition between the natures of different bonds. Both these compounds contain group V ions which can exhibit multiple valency. According to a simple valence count, with Cu (I) being 1+ and Se (VI) 2-, for the charge to be compensated V should be pentavalent (5+) to explain the semiconducting properties of these compounds. However, GGA calculations for Se4 (Wang *et al.* [116]) suggests that Se4 is metallic while experiments reported a band gap of 0.1–0.4 eV.[106, 110, 111] A recent calculation employing the hybrid functional scheme developed by Heyd, Scuseria and Ernzerhof (HSE), which includes non-local exchange interaction, gives a band gap of 0.4 eV[109]. Nevertheless, in all the previous studies of Se4, the questions of Sb valency, the precise nature of the bands near the gap region and the physical origin of the gap formation in Se4 have not been addressed.

This chapter will try to answer some of the questions mentioned above. It is arranged as following. In section 4.2 the crystal structures of Fa and En are briefly reviewed. I will discuss the

band gap formation in Se4 in 4.3 by carrying out extensive *ab-initio* electronic structure calculations using several local/semilocal approximations such as local density approximation (LDA), GGA,[47] GGA+U[66] and recently developed modified Becke-Johnson (m-BJ)[52] exchange potential. In addition, I have also used non-local approximations to exchange correlation potential (HSE06)[59–61] to calculate the electronic structure. Then in section 4.4, I show that the physics of band gap formation is generic for the whole family of I_3-V-VI_4 compounds and study how the band gap varies for different compounds. Then the temperature and carrier concentration dependence of thermopower in Se4 are presented and how they depend on the details of the electronic structure is discussed. Thermoelectric properties of Se4 and summary of the chapter are given in section 4.5 and 4.6 respectively. The results presented in this chapter are partially published in references [36] and [37].

4.2 Crystal structures of Famatinite and Enargite

Systems are considered in this chapter belong to the family of I_3-V-VI_4 compounds where (I) is Cu or Ag, (V) is P, As or Sb, and (VI) is Se or Te. While most Ag-compounds are not found in the literature, Cu-compounds usually crystallize in the Famatinite structure (Fa) and some in the Enargite structure (En). As discussed in the previous section, Famatinite and Enargite structures may be considered as derivatives of the well known Zinc blende and Wurtzite structures respectively. As shown in Fig. 4.1, Fa and En can be obtained by doubling the ZnS unit cell (Zincblende or Wurtzite respectively) and replacing four Zn atoms by three group I element (Ag or Cu) and one group V element (P, As, Sb). This keeps the valence electron count intact (4 divalent Zn vis-à-vis 3 monovalent Ag/Cu and 1 nominally pentavalent P/As/Sb). In our calculations, due to different space groups (body centered tetragonal for Fa and simple orthorhombic for En), the Fa unit cell contains one formula unit while En unit cell has two formula units. This difference gives rise to different Brillouin zones and a difference in the number of bands for a given wave vector **k**, i.e. En has twice as many bands as Fa.

In both the structures, each atom is tetrahedrally coordinated to four nearest neighbors, in which

69
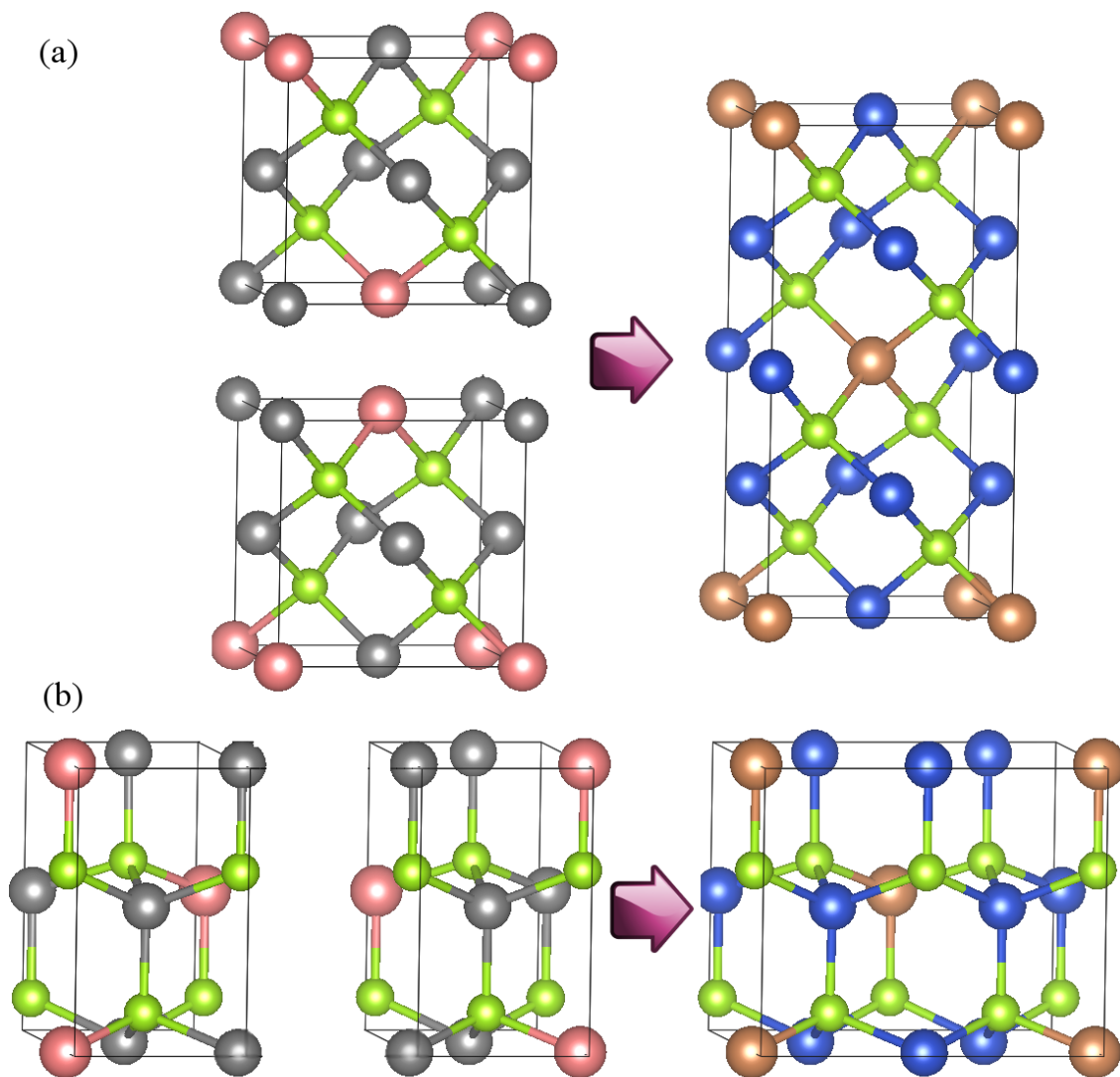
Figure 4.1: Crystal structure of Famatinite (Fa) and Enargite (En) structure are represented as double unit cell of the Zinc blend (top panel) and the Wurtzite (bottom panel). Green represents S (Se, Te), gray represents Zn which are replaced by Copper/Silver (blue) and red represents Zn which are replaced by Sb (P, As, Bi).

Table 4.1: Summary of crystal structures of Cu_3AB_4

B\A	P	As	Sb	Bi
S	En $d = 2.06^{exp\cdot}$[117, 118] 2.11^{GGA}	Fa/En($T_c = 580$)[111] $d = 2.20^{exp\cdot}$[119] 2.31^{GGA}	Fa $d = 2.38^{exp\cdot}$[118] 2.48^{GGA}	Fa d = 2.65^{GGA}
Se	En $d = 2.29 - 2.36^{exp\cdot}$[117] $2.29 - 2.32^{GGA}$	Fa $d = 2.50^{GGA}$	Fa $d = 2.54^{exp\cdot}$[120] 2.65^{GGA}	Fa d = 2.78^{GGA}
Te	$\times$	?	?	$\times$

En = Enargite, Fa = Famatinite, $\times$ = does not exist, ? = unknown, d = nearest neighbor distance between atoms A and B (unit Angstrom). GGA indicates that parameters were relaxed using GGA approximation in the present work.

I and V atoms bond to four VI atoms while VI atoms bond to three I and one V. Table 4.1 presents a summary of crystal types of I_3-V-VI_4 compounds and the bond lengths between V and VI. As the constituent atoms go from smaller to larger radii, the bond lengths increase accordingly. We will show later that the change in bond lengths and the band gaps are intimately related.

4.3 Electronic structure of Cu_3SbSe_4: band gap formation and the role of Sb lone pairs and non-local exchange effect

This section will try to resolve the puzzle about the band gap in Se4 mentioned in section 4.1, by comparing electronic structure obtained using different approximations including GGA, GGA+U and HSE06. In order to understand how the structural property affects the electronic structure of Se4, we also carry out calculations with Cu_3SbSe_3 (hereinafter, it will be referred to as Se3) which has one Se less than Se4, and therefore, does not have the tetrahedrally coordinated structure.

Let us first briefly review the experimentally known atomic structures of these two compounds. Below 700 K Se4 has the Famatinite lattice structure, crystallizing in base centered tetragonal structure (space group I$\bar{4}$2m)[111] (Fig. 4.2(left)). At room temperature, Se4 has lattice constants of $a = 5.661$ Å and $c = 11.280$ Å. [120] Each Cu and Sb is coordinated tetrahedrally to Se while
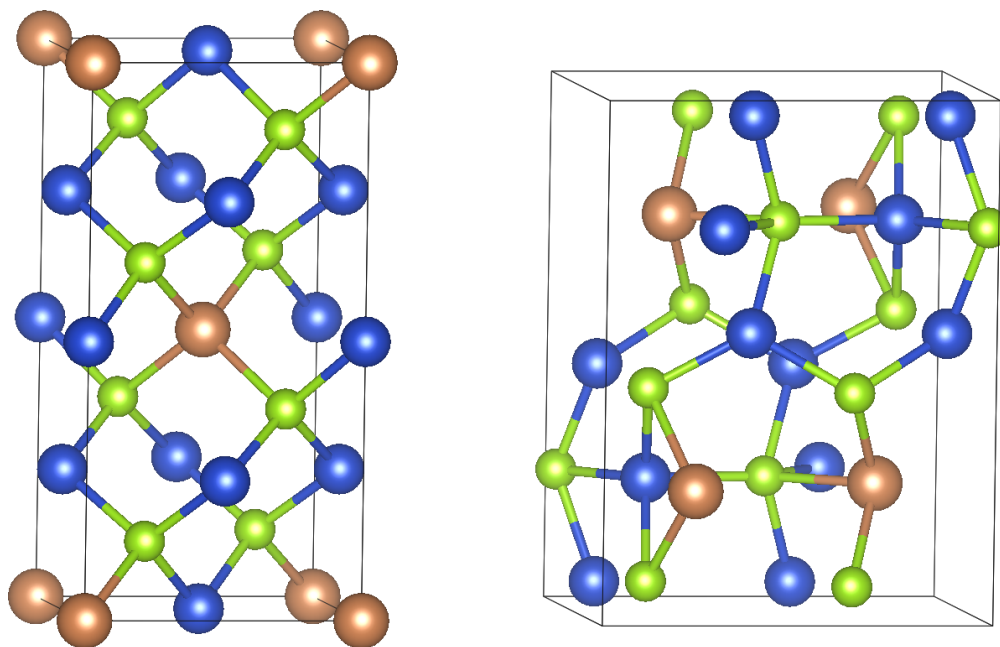
Figure 4.2: Crystal structure of Cu_3SbSe_4 (left) and Cu_3SbSe_3 (right), Cu is blue ball, Sb is brown, and Se is green.

each Se is coordinated to three Cu atoms and one Sb atom. Unlike Se4, Se3 has a more complicated orthorhombic structure (space group Pnma) with lattice constants $a = 7.986$ Å, $b = 10.614$ Å, and $c = 6.837$ Å at room temperature[121] (Fig 4.2(right)). The local coordination and bond lengths in this compound are very different from those in Se4. Sb has three Se and one Cu nearest neighbors (nns), whereas Cu has four Se and one Cu nns. The fact that Sb has an asymmetric network facilitates the existence of a dynamically active $5s^2$ lone pair of electrons in Se3. This lone pair of electrons, however, do not actively involve in band gap formation of Se3. This structural distinction is believed to be the origin of the difference in their physical properties (the physics of band gap formation and the unusual lattice anharmonicity of Se3[28]) in spite of similar compositions with identical elements.

4.3.1 GGA calculation and indication of the existence of Sb lone pair electrons

The GGA-PBE band structures for Se4 and Se3 are shown in Fig. 4.3(a) and 4.3(b) (left panels), respectively. The present GGA calculation for Se3 agrees reasonably well with the recently pub-
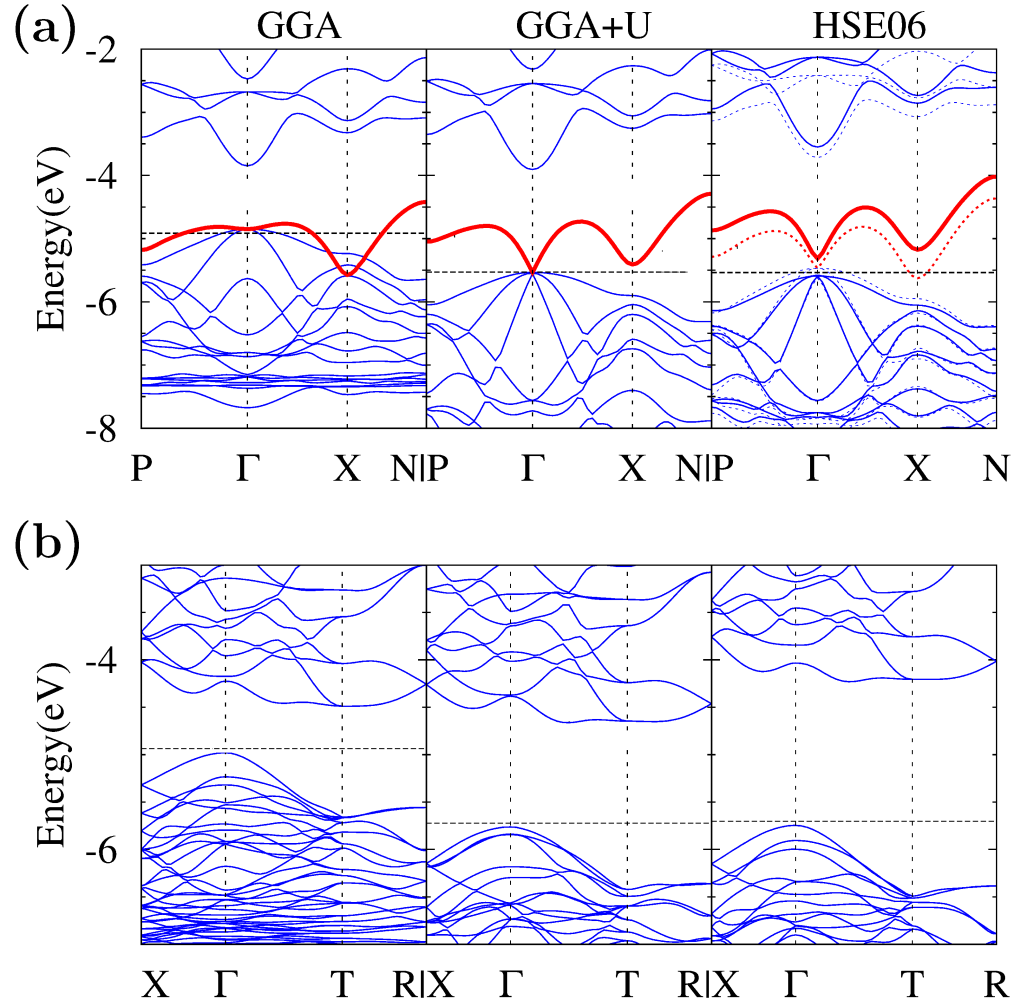
Figure 4.3: Band structures of Cu_3SbSe_4 (a) and Cu_3SbSe_3 (b) using different methods. In (a), the bold (red) line is "BOI", the doted lines present the HSE band structure using GGA position. U_{Cu-d} = 10 eV was used in GGA+U calculation. The energy is given in absolute scale and the Fermi energy is denoted by E_F.

lished LDA calculations by Sevik and Çağin (SC) [108], showing that Se3 is a narrow band gap semiconductor with an indirect band gap. However a larger band gap was found, 0.49 eV compared to 0.24 eV by SC [108]. There are several reasons that may account for this difference. First, SC used LDA which usually gives smaller lattice constant (a=7.924 Å) compared to our GGA calculation (a=8.075 Å). Second, SC define the band gap using the DOS which is very sensitive to the smearing method used in computing the DOS, whereas we obtain the band gap using the band dispersion.

In contrast to Se3, GGA calculation reveals that Se4 is not a semiconductor, disagreeing with the experimental measurements. There is a narrow band, with a width of ∼1 eV (marked as bold and red in Fig. 4.3, near the top of the valence band, which is partially filled. We refer to this band as the "band of interest" or "BOI". At the Γ point, "BOI" is degenerate with the top two valence bands. At the X point, it gets lower and overlaps with several valence bands. By exploring the physical origin of "BOI" and its sensitivity to different approximations, it reveals that the origin of the "BOI" is intimately related to the question of Sb valency in Se4.

It is quite easy to understand the semiconducting ground state of Se3 using the simple ionic picture and the octet rule. In Se3, Cu takes the 1+ ionized state, Se is 2-, and Sb is 3+ (trivalent). With this configuration, all the octets are filled, making Se3 a semiconductor. Using the similar argument, but with pentavalent Sb (5+) for Se4, one would come to the same conclusion. However, GGA band structure does not seem to support this simple picture, since there is a nondegenerate conduction band (BOI) overlapping with the valence bands, making Cu_3SbSe_4 a semimetal or a pseudo-gap system.

In order to see the similarities and the differences between Se4 and Se3 I plot the total density of states (DOS) for both the compounds (Fig. 4.4(a), top panel) and the projected DOS (PDOS) of Se4 (Figure 4.4(a), bottom panel). It can be seen that the only significant difference between them is the "BOI" state near the Fermi level (E_F) in Se4. In both compounds, the Sb 5s bands are quite narrow (∼0.5 eV) and located approximately at -9.5 eV, while the Sb p bands are above the Fermi level. This suggests that Sb is nominally 3+ in both the systems. In addition, Cu s is empty. As a
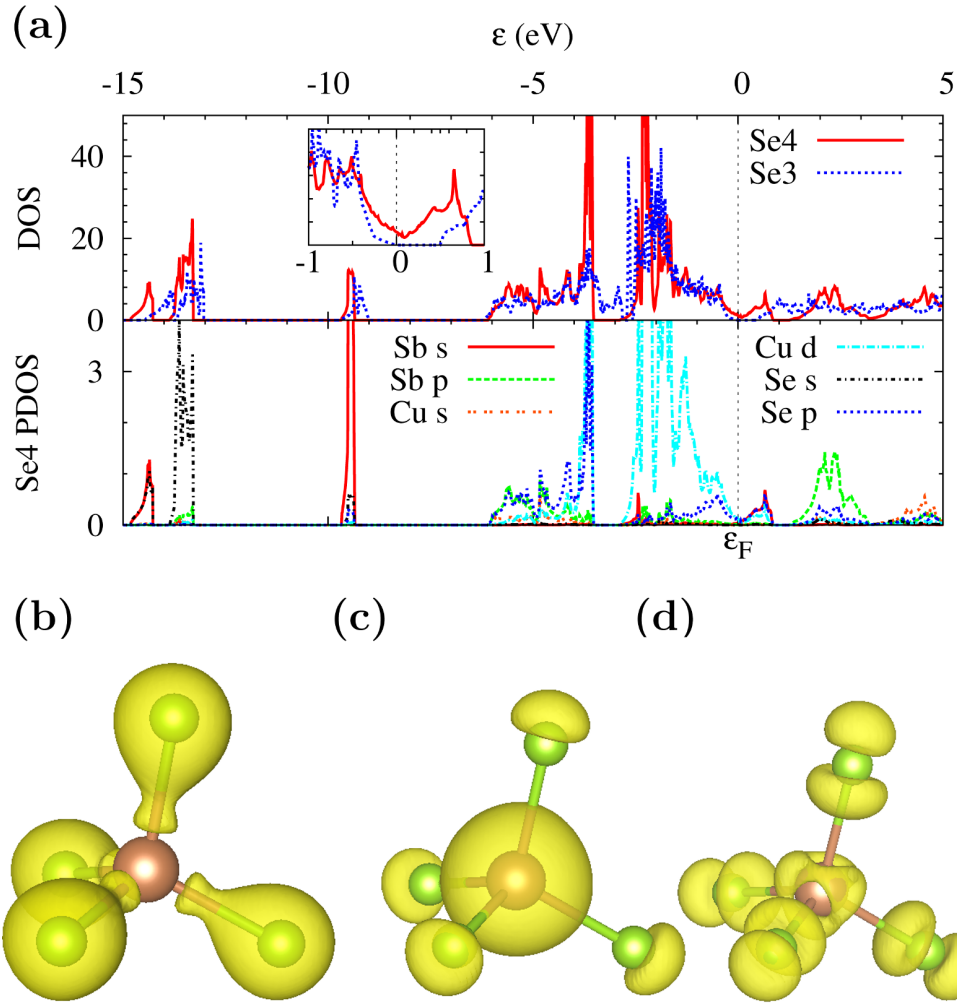
Figure 4.4: (a) Total DOS of Se4 and Se3 (top panel) and the projected DOS of Se4 (bottom panel), along with isosurface plot of charge density associated with (b) the lowest band at -14.5 eV, (c) the Sb-*s* band at -9.5 eV, and (d) the "BOI". For clarity, we only show SbSe$_4$ tetrahedron with Sb at the center. The DOS are given in unit of number of states per eV per formula unit.

consequence, Se-p is fully filled in Se3 making it a conventional semiconductor. In contrast, for Se4, Se p bands are two electrons deficient from being completely filled (corresponding to nearly unoccupied "BOI"), leading to a semi-metal. The DOS of Se4 near the Fermi energy indeed shows a pseudogap structure (Fig. 4.4 (a) inset).

To further understand the nature of the bands in Se4, we look at the partial charge densities associated with three narrow bands, one at -14.5 eV, one at -9.5 eV, and the "BOI" as shown in Figs. 4.4(b), 4.4(c), and 4.4(d), respectively. At -14.5 eV, there is a bonding state of Se s and Sb s which splits off from the other Se s states by about 1 eV. The state at -9.5 eV is mostly Sb s with some Se p, resulting in a charge density with asymmetric lobes around Se directed away from Sb which is different than usual s-p hybridization. The "BOI" band is a mixture of Se p, Sb s and Cu d.

To explain the origin of the "BOI" a simple scheme is proposed for the mixing of orbitals in Se4 as shown in Fig. 4.5, where it ignores the interaction between Se and its neighboring Cu orbitals which gives rise to the p-d hybridization with energy in the range of -6 eV to 0. In the final picture this hybridization plays an important role, particularly when the effect of Coulomb correlation is included through the parameter U. At -14.5 eV the mixing between Sb $5s$ and the symmetric combination of four nearest neighboring Se $4s$ ($\psi_{Se,s} = \sum_{\mu=1,4} \phi_{Se\mu,s}$) leads to a bonding (B) combination $\psi_{s,B} = \phi_{Sb,s} + A\psi_{Se,s}$ whose energy (-14.6 eV) is about 1 eV lower than the rest three Se $4s$ bands. The charge density associated with $\psi_{s,B}$ indeed shows the bond charge between Sb and neighboring Se atoms. The charge density for the state at -9.5 eV looks rather peculiar with asymmetric lobes around Se atoms (Figure 4.4(c)). It can then be thought of as a *bonding combination* of an antibonding (AB) state of $\phi_{Sb,s}$ and $\psi_{Se,s}$, i.e. $\psi_{s,AB} = \phi_{Sb,s} - A\psi_{Se,s}$ and the neighboring Se $4p$ states ($\psi_{Se,p}$). This results in a cancellation of Se $4s$ and $4p$ amplitudes in the region between Sb and Se, leading to the peculiar shape of the charge density, seen in Figure 4.4c. The corresponding *antibonding combination* has a finite density in the region between Sb and Se, leading to the "BOI". The charge density associated with "BOI" shows a mixing of Sb-$5s$, Se-$4p$, Se-$4s$ and Cu-d characters. Thus it is a rather subtle and complex state. As we will see, its position
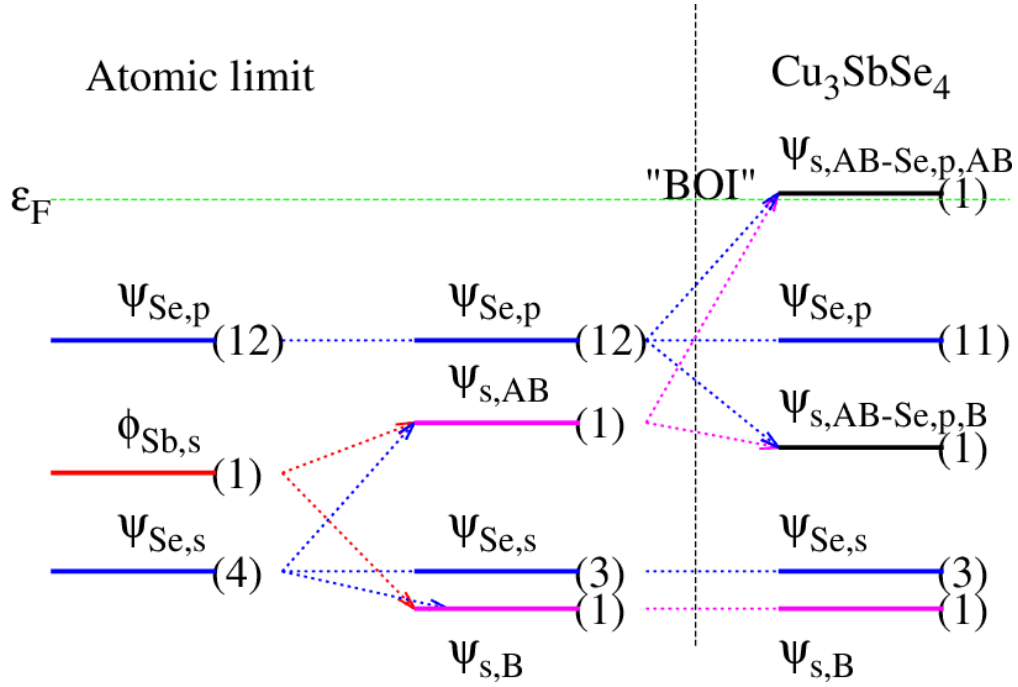
Figure 4.5: Simple bonding-antibonding scheme in Cu_3SbSe_4 showing energy levels in the atomic limit (left column) intermediate bonding-antibonding states (middle column) and bonding-antibonding states in crystal (right column). (Cu d and Sb-p are not shown for simplicity). The number of states associated with each level is given in the bracket.

and dispersion are quite sensitive to the approximations made in treating the exchange-correlation potential. However, the general mixing picture discussed above (over energy range ~ 10 eV) is valid for all the approximations used.

4.3.2 Failure of local exchange approximation – Effect of non-local exchange interaction

In order to see if the semiconducting state can be obtained in Se4 within local approximation, I have tried a recently proposed semi-local model called modified Becke-Johnson (m-BJ) model which introduces a correction which depends on the kinetic energy density ($\sum |\nabla \psi_{i\sigma}|^2$) to GGA. This model has been found to give reasonable gap values in a large number of semiconductors [52]. Within this model, Se3 is found to be a semiconductor with a gap of about 1 eV compared to 0.49 eV obtained in GGA. However, m-BJ does not open up a gap in Se4.

For Se4 to be a semiconductor, the "BOI" must split off from the rest of the Se p bands. Since
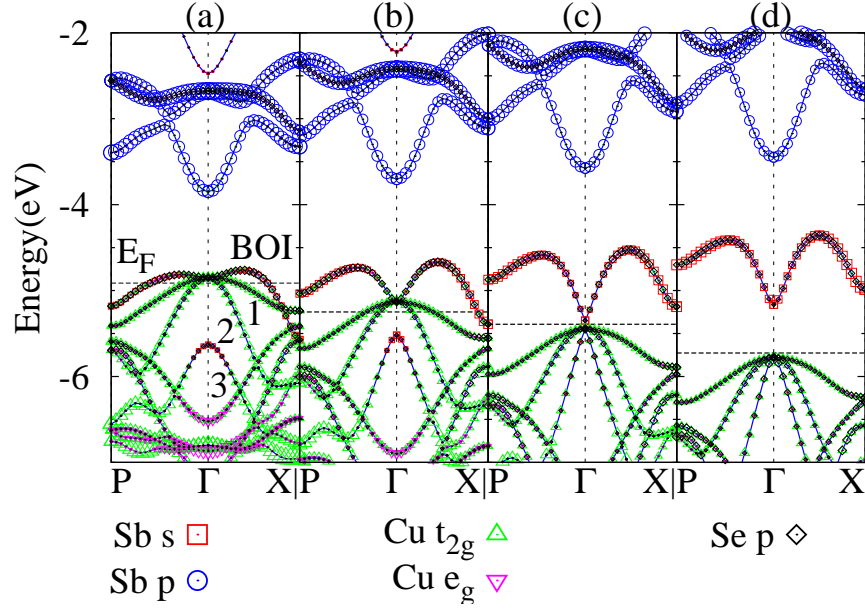
Figure 4.6: Band structure of Cu_3SbSe_4 in absolute energy scale for the ratios of exact exchange α = (a) 0, (b) 0.1, (c) 0.2 and (d) 0.3 with fat band representation of orbital character, showing that the bands with dominating d characters affected strongly; there is an exchange of band character between BOI and BOI-3 at a critical value of α, $\alpha_c \approx 0.2$.

it includes a small admixture of copper d-states the effect of intrasite d-d Coulomb repulsion can have important effects on the position and hybridization of "BOI". For this, I carried out GGA+U [65] calculations with different U values ($0 \leq U \leq 20$ eV) at the copper site. In Fig. 4.3 (middle panel) we give the band structure with U_{Cu}=10 eV. We find that in Se3, by increasing U from 0 to 10 eV, band gap changes from 0.49 eV to 1.10 eV (similar to what is seen in m-BJ). There is a large rearrangement of most of the valence bands but the dispersion of the top most valence band and the lowest conduction band does not change much (which is relevant for thermoelectric properties). However in Se4, the dispersion of the "BOI" changes drastically and there is a level-reordering in the band structure near the Fermi level. For example, at the X points, the "BOI" is pushed higher than the valence bands and there is also a dramatic change in the top four bands near the Fermi level at the Γ point. However, a gap does not open up unless U is larger than 12 eV. This value is however unphysically large compared to typical values of U for copper, 5–8 eV.[68, 122–125]

In order to circumvent the problem of using large U within local and semi-local theories, the effect non-local exchange is studied using HSE06 model ($\alpha = 0.25$). [59–61] Since Yang *et al.*

78

[109] have already reported the existence of a band gap in Se4 using this model, we wanted to investigate in detail how non-local exchange affects different bands near the Fermi level and how the gap opens up. In Se3, HSE06 increases the band gap from 0.49 in GGA to ∼1.5 eV as expected (Fig. 4.3(b) right panel). In Se4, even for this model, if we use the atomic positions optimized using GGA, there is no gap (presented as dotted lines in Fig. 4.3(a)). After carrying out further internal relaxations within HSE06, we find that, compared to GGA values, the distances between Sb and its four Se neighbors decrease by 3.4%, the distances between Cu and its neighboring Se increase by ∼1% (detail is shown in table 4.2)and a direct gap of 0.26 eV is formed at the Γ point between "BOI" and the rest of the occupied bands (Fig. 4.3(a) right panel). This value of band gap is in good agreement with experimental values (0.1–0.4 eV)[106, 110, 111] but smaller than the value of 0.4 eV found by Yang *et al*. [109]. We believe that the difference between our result and that of Yang *et al*. [109] is due to the difference in the lattice parameters used, and also due to the estimation of the gap from DOS calculation by these authors, rather than using the actual band dispersion.

To further understand the band gap formation in Se4 the effect of non-local exchange on the band structure is studied using different values of α and look not only at the "BOI" but also three other bands right below it. These three bands are denoted as BOI-*i*, where *i*=1–3 (labelled "1", "2" and "3" in Figure 4.6). Fig. 4.6 shows the band structure of Se4 with different values of α showing how different bands are affected. For each value of α, internal relaxation was performed.

For α=0 (i.e. GGA), at the Γ point, three bands "BOI", BOI-1 and BOI-2 are degenerate and have mainly Cu t_{2g} and Se p characters. When one moves away from the Γ point the character of "BOI" changes to a mixture of Sb s, Se p and Cu e_g, whereas the characters of BOI-1 and BOI-2 remain the same as at the Γ point. The character of BOI-3 is the opposite of that of BOI, i.e. a mixture of Sb s, Se p, and Cu e_g at the Γ point which changes to a combination of Se p and Cu t_{2g} by moving away from it. This inverted-band feature was discussed by Wang *et al*. [116] to point out the nontrivial topological property of Se4 which, as shown later, is not valid when HSE06 is used. There is a band-crossing at the X point where the energy of the "BOI" is lower than the other

79

Table 4.2: Nearest neighbor distances (Å) and band gaps (eV) with different exact exchange ratios

α	Sb-Se	Cu1-Se	Cu2-Se	E_g(eV)
0	2.65	2.44	2.43	–
0.1	2.59	2.46	2.44	–
0.2	2.55	2.47	2.45	0.08
0.3	2.53	2.48	2.45	0.6

three. With increasing α, the bands containing Cu t_{2g} are pushed down faster. There is a removal of band-crossing at the X point. When $\alpha \geq 0.2$, at the Γ point, the "BOI" switches its character with BOI-3 and remains nearly at the same position while the other bands keep going down. After the band gap opens up, "BOI" has consistent character throughout the **k** points sampled, namely, it is primarily a mixture of Sb $5s$, Se $4p$ and a small admixture of Cu e_g. At this point, a gap formation is observed at the Γ point. Then the "BOI" becomes the lowest conduction band (LCB) which is predominantly a mixture of Sb $5s$ and Se $4p$. As mentioned above, the band structure using HSE06 does not support the inverted-band picture suggested by Wang *et al.* [116] because of the switching of characters between BOI and BOI-3 when the gap opens up. It is interesting to note that for $\alpha = \alpha_c$, one sees a linear dispersion (Dirac cone) involving BOI and BOI-3.

Studying the nearest neighbor distances in Se4 as a function of the strength of non-local exchange reveal that by increasing α the Sb-Se distance gets shorter while Cu-Se distance gets longer.(Table 4.2) This suggests that the non-local exchange interaction is stronger between Sb and Se due to large overlap between Sb $5s$ and Se $4p$.

It is interesting that, in Se4, local and semi-local approximations to the exchange interaction fail to open up the gap. Furthermore, employing non-local exchange only is not sufficient to open a gap, one has to relax the bonds. These observations strongly suggest that the nearest neighbor distances between Se and Sb, and between Se and Cu play an important role in opening the gap. Thus, it is believed that non-local exchange interaction between the $4s$ and $4p$ electrons of Se and the neighboring Sb $5s$ and Cu $3d$ electrons are responsible for the gap formation. The band structure of Se4 obtained using HSE06 can be directly tested experimentally by (1) probing the

excitations from occupied Cu d bands to the conduction bands, i.e. by determining the peaks in the excitation spectrum one can confirm the position of Cu d states which are at about 3–4 eV below the lowest conduction band; and (2) doing NMR measurement in n-doped sample, which should show a Knight-shift of s-spin density at the Sb nucleus.

4.3.3 Unphyscal value of U and its meaning

Even though GGA+U fail to predict the semiconducting ground state of Se4 within typical (physical) range of U value (unlike the case of Fe$_2$VAl discussed in chapter 3), one can get results almost identical to that obtained in HSE06 within GGA+U (local theory) but using an unphysically large value of U ($\sim$15 eV) for the Cu-d orbitals. One can see that changing U gives similar effect as changing α. As seen in Fig. 4.7a, increasing U does two things, it lowers the occupied d bands of Cu which reduces the hybridization between the Cu d and the rest of the s, p bands (the amount of d-character in BOI at the Γ point decreases) and eventually for a sufficiently large value of U ($>$ 10eV), a gap opens up between the BOI and the rest of the occupied valence bands. one also observes a similar effect in HSE06 calculations as one increases the strength of the non-local exchange by increasing the value of the mixing parameter α as shown in Fig. 4.6.

One important difference between GGA+U and HSE06 is that the Cu-d bands are pushed down much further in the former, which can be easily observed in Fig. 4.7. In Fig. 4.7a, as U increases, the mixing between Cu d and Se p decreases, and as a result, the d character in the conduction bands near Fermi level gets weaker and eventually disappear at large U. This effect is clearly seen in Fig. 4.7b which compares band structures obtained using GGA, GGA+U and HSE06. If HSE06 indeed gives correct band structure, one should detect a Cu-d peak $\sim$ 3 eV bellow the Fermi level in XPS measurements.

Despite the differences in contributing orbitals, the band structure near the Fermi level are similar in GGA+U (U=15 eV) and HSE06 (α=0.25). Since physics of materials depend mostly on the electronic structure in this range, GGA+U (even with unphysical U) calculations can give some good insight about physical systems of interest without consuming huge computational resources
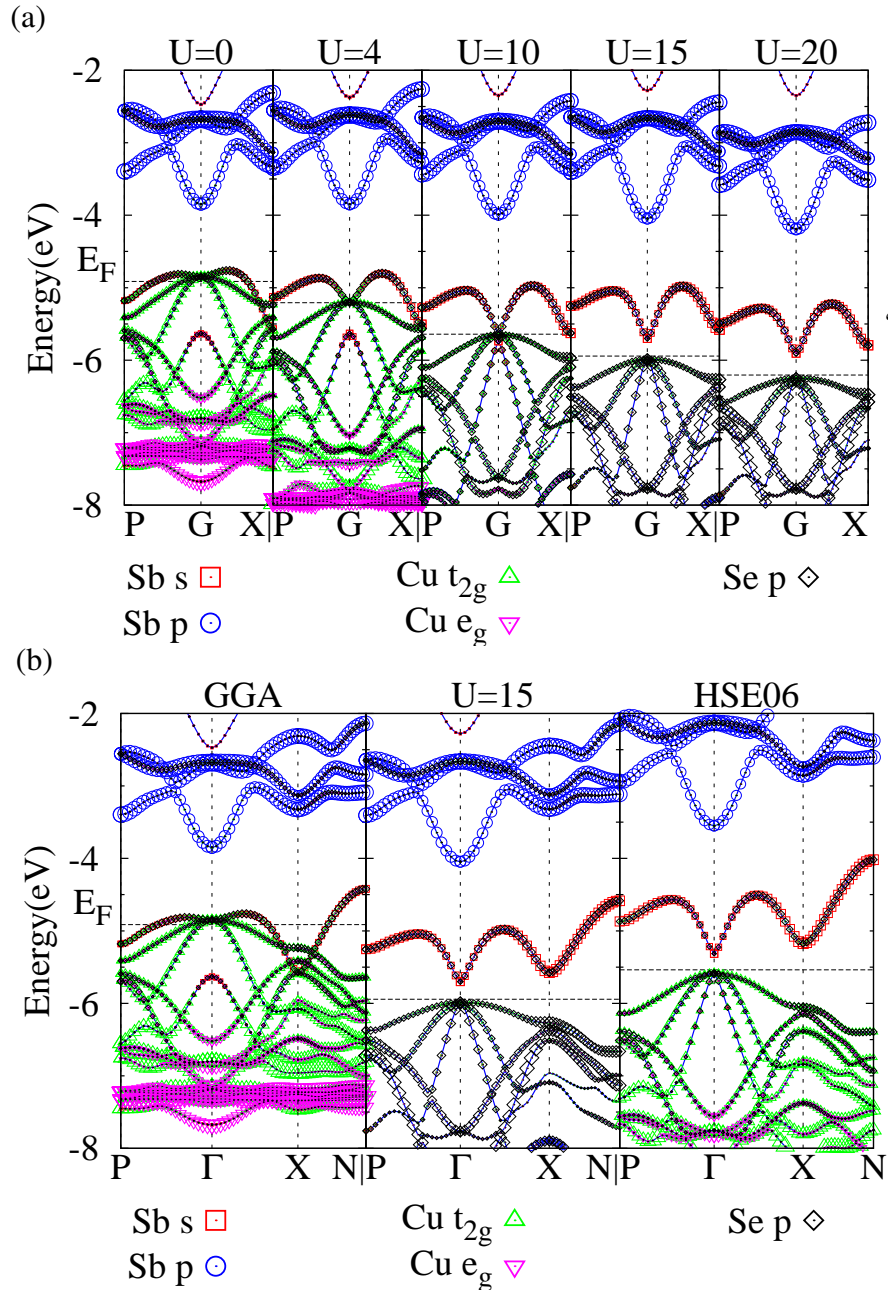
Figure 4.7: (a) Effect of U on band structure and (b) comparison between GGA+U and HSE06 band structures. The energy is given in the absolute scale.

as required by HSE06.

4.4 Bond and band gap in the a class of I_3-V-VI$_4$ Famatinite and Enargite compounds

In section 4.3.1, a simplified model is proposed for the bonding and anti-bonding states between the states of different atoms as shown in Fig. 4.5. In this picture, *s*-level of Cu and *p*-state of group Sb have highest energy and donate all their electrons to the others. The *s*-states of the Se can be treated as filled core states and the *s*-states of the monovalent cation as empty states to start. The *p*-states of Se anions and *s*-state (lone pairs) of Sb strongly interact and form the bonding and anti-bonding bands, giving rise to an unoccupied band (the so called "BOI") near the Fermi level. The position of the BOI is very sensitive to the approximation schemes used in calculations of the electronic structures and the distance between the Se atom and its four Se neighbors. The lone pair states of Sb are somewhat schizophrenic, on the one hand they bond with the *s*-states of the surrounding Se *s*-cores but also like to bond with one properly symmetrized combination of the *p* states of the surrounding Se$_4$ cluster. This latter bonding is so strong that it splits off one band from the top of the Se *p*-bands giving rise to a band gap. The *d*-bands of Cu are quite narrow and lie below but near the Fermi level. Their precise role in the band structure depends on the particular type of atoms forming the compound. The aim in this section is to extract some of the generic (universal) roles of the V lone pairs and to show that the proposed bonding-antibonding picture for Cu$_3$SbSe$_4$ is rather universal and applicable to the other tetrahedral compounds containing V-VI$_4$ (SbSe$_4$) clusters.

4.4.1 Atomic energy levels of constituents and some schematic studies.

In analyzing bonding and antibonding nature of different bonds and bands, it is helpful to know the energies of atomic levels of the constituent atoms. Table 4.3 gives the atomic energies of the *s* and *p* valence electrons for different constituents and for Cu the energy of the *d*-level is also given. Positions of these atomic levels are shown in Fig. 4.8. It is clear that Cu-d and S/Se-*s* levels are

83

Table 4.3: Atomic energies of the *s* and *p* valence electrons for different constituents and for the monovalent Cu, the energy of Cu *d*-level is included

Energy(eV)	P	As	Sb	Bi	Cu	S	Se	Te
E_s	-19.22	-18.92	-16.03	-15.19	-7.7	-24.02	-22.86	-19.12
E_p	-9.54	-8.98	-8.14	-7.79	–	-11.6	-10.68	-9.54
E_d	–	–	–	–	-20.26	–	–	–
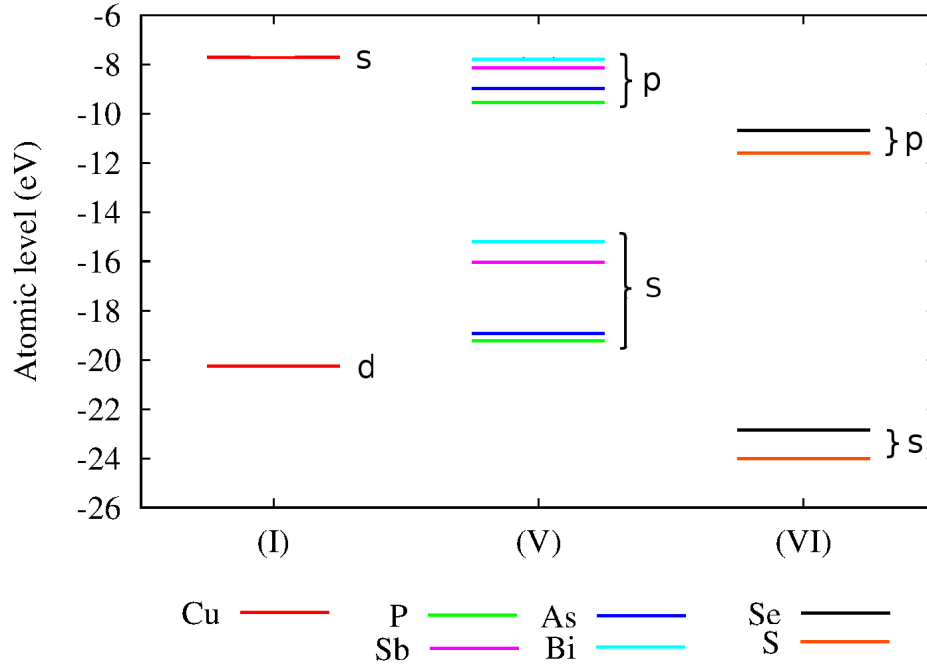
Figure 4.8: Visualization of the atomic levels of constituent atoms.

the lowest which makes S/Se-*s* states stable and occupied while Cu-*d* are near the Fermi level as usual. The energies of the *s* and *p* levels of group V atoms increase in going from P to Bi.

In Se4, the band structure was found to be affected significantly by the bond length between Sb and Se. Since nearest neighbor distances increase from P to Bi (table 4.1), one should expect competing effect of the shrinking of bonding-antibonding separation and the narrowing of the bandwidth in forming the band gaps. This competing relation is more complicated due to the differences in energies of different atomic levels. Furthermore, the role of *d* electrons of Cu also have to be considered. In order to isolate the effect of *d* electrons, one can replace Cu by an alkali atom and study the difference in electronic structure.

4.4.2 Results obtained using local approximations

To understand the crucial role played by the lone pairs (ns^2) of the group V atoms in the bonding-antibonding scheme and whether the underlying mechanism for the formation of band gap proposed in Cu_3SbSe_4 can be applied to other members of the I_3-V-VI_4 family, firstly, GGA calculations were carried out for systems in this family, $Cu_3(P,As,Sb,Bi)(S,Se)_4$. Fig. 4.9 shows the band structures of these compounds, focusing near the Fermi level, in which the BOI are marked as red thick lines. The GGA calculations show that all the compounds have similar features in their band structures which resemble the simple picture of the bonding-antibonding scheme discussed earlier. The difference between En and Fa band structures is that for each **k** the former has twice as many number of bands as the latter. As a result En has two BOIs. All the compounds have Cu-d states occupied right below the Fermi level and the lowest partially unoccupied band is the BOI. The Cu-d states mix with the Se-p states. These systems like Cu_3SbSe_4 are semimetals with pseudogaps near the Fermi energy. For these systems, the Cu-d states mix with the BOI at the Γ point of the Brillouin zone, giving rise to a three-fold degenerate band, while the next band has Sb-s and Se-p characters as the BOI. The only exception is Cu_3PS_4 where there is a band gap (of ~ 0.5 eV) between BOI and the rest of the bands below, which are occupied; it is predicted to be a semiconductor even with GGA level of approximation. The reason which makes Cu_3PS_4 unique is that it has the shortest nearest neighbor distance as listed in Table 4.1. The overlap between BOI and valence bands increases in going from P to Bi as well as from S to Se.

As discussed in section 4.3.3, since we are dealing with a large number of systems, and due to limited computational resources, GGA+U (with effective U=15 eV), instead of HSE06, is a good start to understand the band structures near the Fermi level. Also GGA+U will be much easier to implement when one studies the nature of defect states in these compounds because in this case one will have to use large supercells with number of atoms $\sim$64 or larger. Of course whenever we have some questions for a particular system one can go back to HSE06. In Fig. 4.10, GGA+U band structures of (a) Cu_3PS_4, (b) Cu_3PSe_4, (c) Cu_3AsS_4, (d) Cu_3AsSe_4, (e) Cu_3SbS_4, (f) Cu_3SbSe_4, (g) Cu_3BiS_4 and (h) Cu_3BiSe_4 are given. For most of compounds, a band gap between BOI and
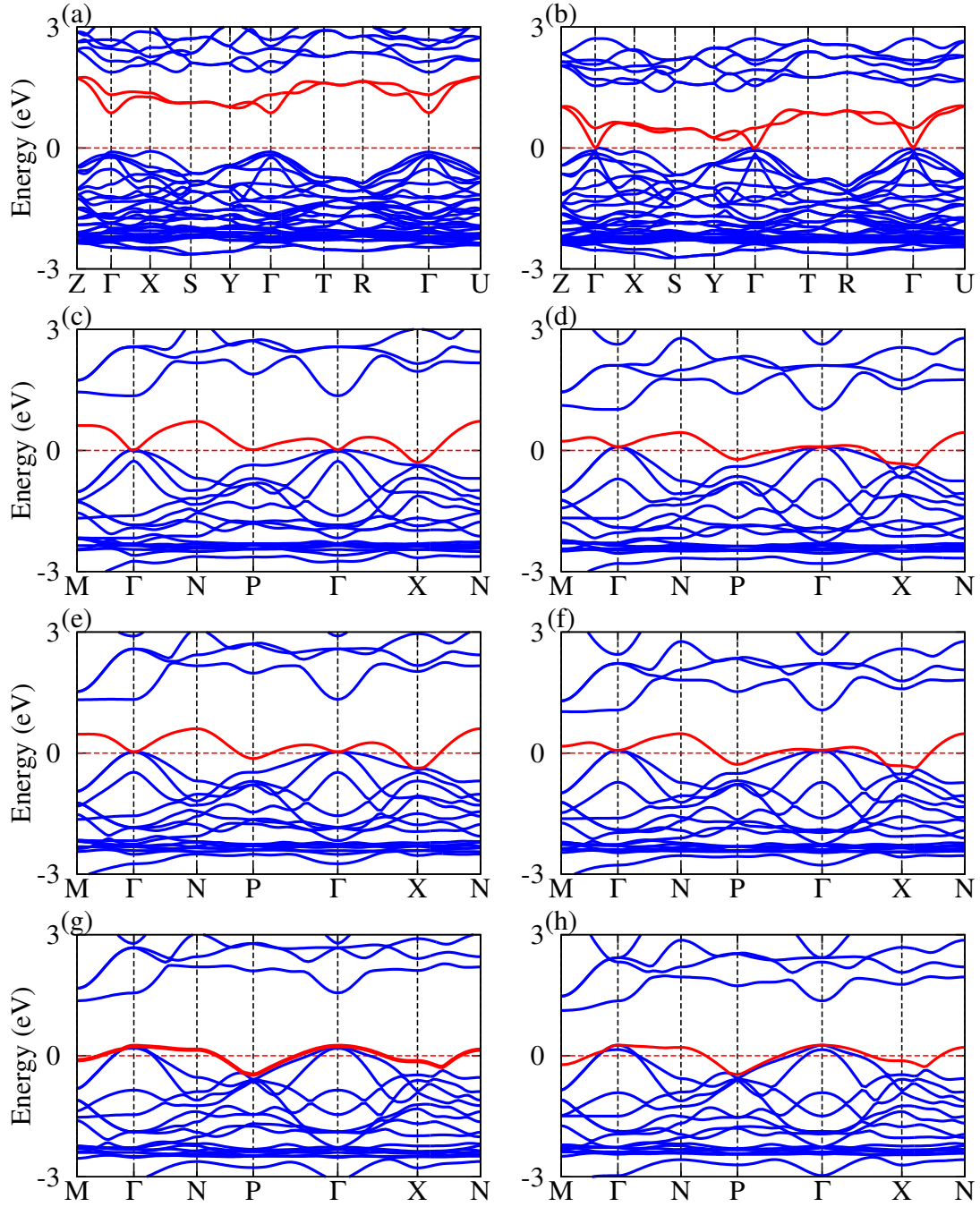
Figure 4.9: GGA bandstructure of (a) Cu_3PS_4 (b) Cu_3PSe_4 (c) Cu_3AsS_4 (d) Cu_3AsSe_4 (e) Cu_3SbS_4 (f) Cu_3SbSe_4 (g) Cu_3BiS_4 and (h) Cu_3BiSe_4. Where the first two compounds are En and the rest compounds are Fa.
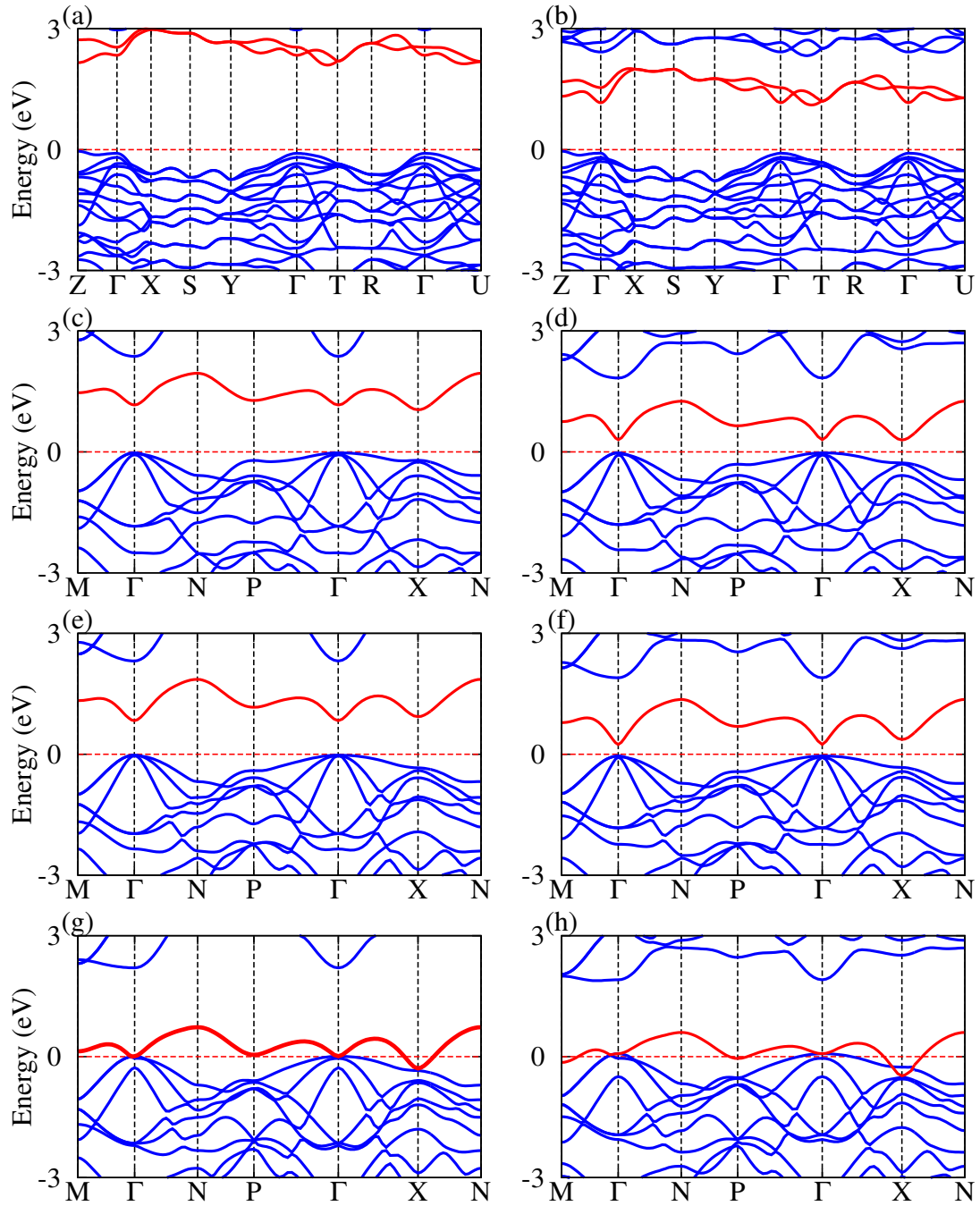
Figure 4.10: GGA+U bandstructure of (a) Cu_3PS_4 (b) Cu_3PSe_4 (c) Cu_3AsS_4 (d) Cu_3AsSe_4 (e) Cu_3SbS_4 (f) Cu_3SbSe_4 (g) Cu_3BiS_4 and (h) Cu_3BiSe_4. Where the first two compounds are En and the rest compounds are Fa.
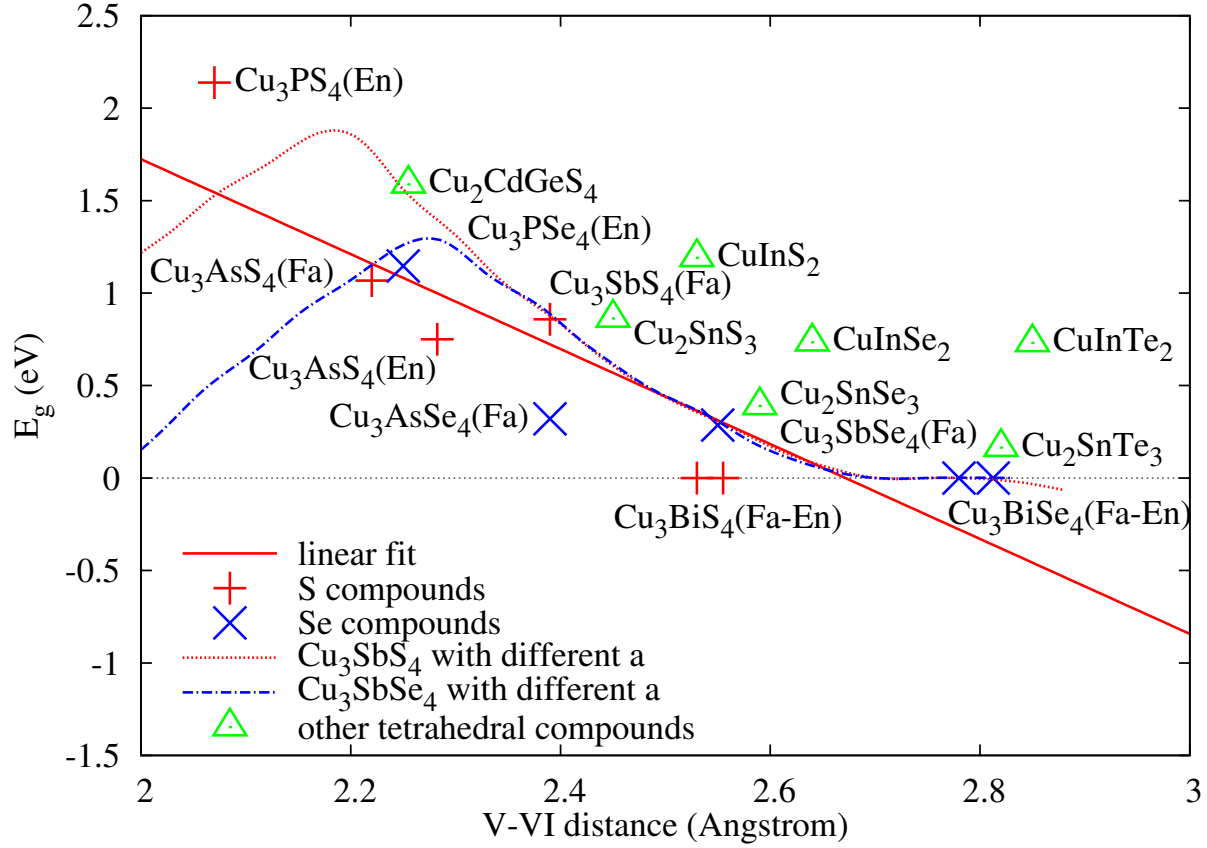
Figure 4.11: Relation between band gap and the distance between V and VI elements.

the occupied valence bands opens up except in Bi compounds. For those compounds where band gap does open up, the highest occupied bands are multiply degenerate, which makes these systems excellent p-type thermoelectrics, just like Cu_3SbSe_4 which will be discussed later in this chapter. We also explored how the band gap and the width of the BOI (now the lowest conduction band) depends on the U parameter. The larger is the U value, the larger is the band gap, and the narrower is the BOI.

To see how the band structures depend on the crystal structure, for some of the compounds, calculations were done for both Fa and En structures. Fig. 4.11 plots the magnitude of the band gap as a function of average nearest neighbor (nn) distance between V and VI elements for Fa and En. For comparison data of the other ternary compounds involving lone-pair atoms is also plotted in Fig. 4.11.

Table 4.4: Effect of different V element substitutions on the band gap of Cu_3SbSe_4 with and without ionic relaxation

| Element | w/ relaxation | | w/o relaxation |
	d_{V-VI}(Å)	E_g(eV)	
P	2.29	0.92	0
As	2.42	0.29	0
Sb	2.56	0.28	0.28
Bi	2.68	0	0

Let us first analyze the trend in I_3-V-VI_4 compounds. One can see that irrespective of the crystal structure (En or Fa), the band gap decreases with the increase of the V-VI distance (d_{V-VI}). The band gap decreases almost linearly with the d_{V-VI} up to $d \approx 2.6$Å as represented by the red solid line in Fig. 4.11. With larger d_{V-VI}, the gap disappears. With other constituents being the same, compounds with S have smaller d_{V-VI} than those with Se, and thus the band gaps are larger in the former. However, for the same d_{V-VI}, Se-compounds have larger band gap. For instance, the band gap of Cu_3SbSe_4 is $\sim$0.4 eV while Cu_3BiS_4 is gapless. One exception is the case of Cu_3SbS_4 and Cu_3AsSe_4. Both of them have $d_{V-VI} \approx 2.4$Å but the former has a larger band gap.

To explain these features, one may attempt to look at the atomic energy levels of the constituents (given in table 4.3 and Fig. 4.8). The difference between S and Se is that the atomic levels of the latter is higher than those of the former, the energy difference for s level is $\sim$1.16 eV and for p is $\sim$0.92 eV. These energy differences may account for the band gap difference between S- and Se-compounds. On the other hand, when going from As to Sb, there is a big jump in the atomic levels (Fig. 4.8). This change in the atomic levels between As and Sb may compensate for the difference in the atomic levels between S and Se, making the band gap of Cu_3AsSe_4 smaller than that of Cu_3SbS_4.

To validate the argument above, d_{V-VI} was varied in Cu_3SbS_4 and Cu_3SbSe_4 by changing the lattice parameter, keeping the relative ionic positions intact (no ionic relaxation). The results are presented in Fig. 4.11 as the purple dotted (Cu_3SbS_4) and cyan dot-dashed (Cu_3SbSe_4) curves. Interestingly, for $d_{V-VI} > 2.3$Å, two curves are almost identical and follow the general trend which

we have discussed above; band gap decreases when the d_{V-VI} increases. This result, however, does not appear to support the relation between atomic levels and band gaps which is argued above in which one would expect the difference between two curves due to the difference in atomic level between S and Se. The two curves only differ from each other for small distances where they split apart by about 1 eV and the trend turns over; the band gap now decreases with decreasing distance. This change indicates that for short distances, the increasing of the band width overcomes the splitting of bonding-antibonding band, reducing the band gap. The turning points are different in two curves, it occurs at larger distance in Se-compound.

In an attempt to resolve this puzzle, the band structures of Cu_3XSe_4, where X is P, As, Sb or Bi, are calculated using the same lattice parameter as that of Cu_3SbSe_4 for two cases: (1) with the same positions of atoms (hence, the same d_{V-VI}) and (2) with the ionic positions relaxed. The results are shown in table 4.4. It is interesting to note that, without relaxation, only Sb-compound has a positive band gap whereas other compounds have overlap between BOI and the valence bands. However, when the atomic positions are allowed to relax, we go back to the general trend where the d_{V-VI} increases as one goes from P to Bi, and as a result, the band gap decreases accordingly. Thus, different constituents affect the local geometry of tetrahedrally coordinated compounds differently, giving different values of the band gaps.

Similar effects are also observed in other tetrahedrally coordinated compounds such as I-III-VI_2, I_2-IV-VI_3. The values of the band gaps (within GGA+U, with U=15 eV) for some systems are shown as green triangle in Fig. 4.11. These materials, in general, have larger band gaps than the I_3-V-VI_4 compounds.

To verify that the underlying physics of the band-gap formation is dominated by the interaction between the lone pairs of V and the p-states of VI and less so by the hybridization with the d-states of Cu, calculations were done for an artificial compound Na_3SbSe_4. The structural parameters, since it is, to the best of my knowledge, not known in the literature, are initially chosen to be the same as Cu_3SbSe_4 but then allowed to fully relax. Fig. 4.12 gives the band structures of Na_3SbSe_4 obtained using GGA (U=0) and HSE06 calculations. GGA already opens up a band
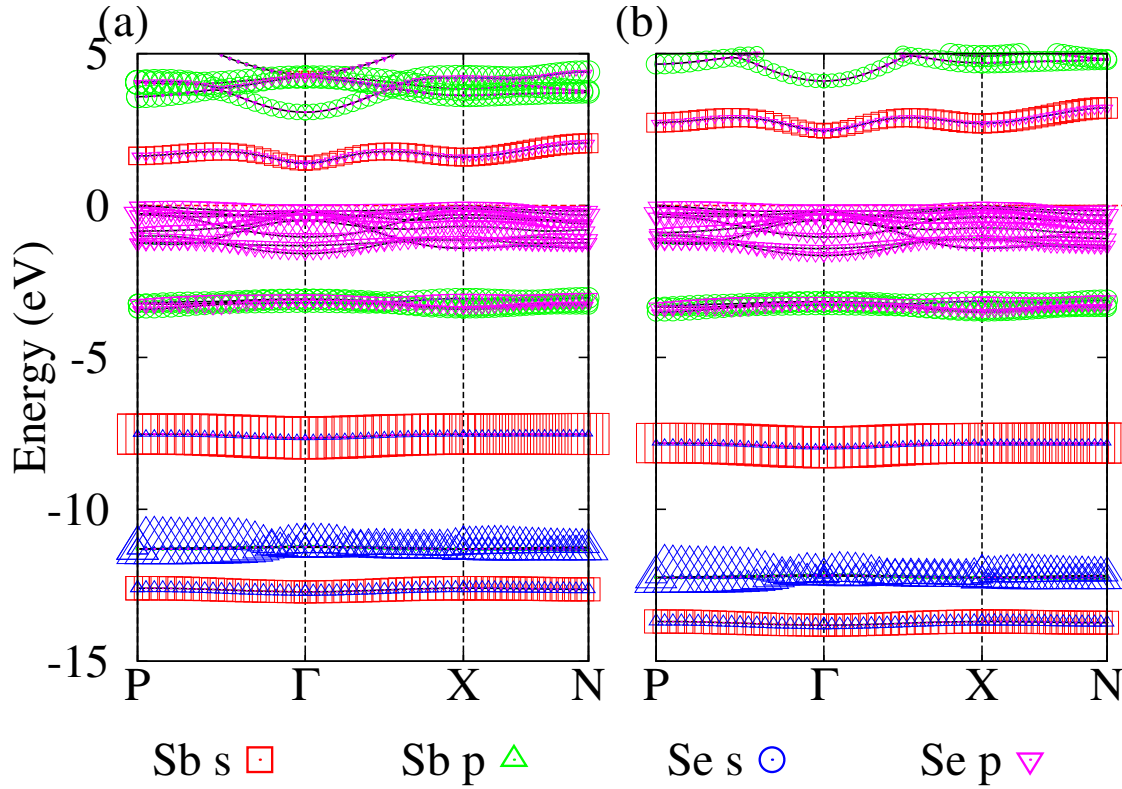
Figure 4.12: Band structure of Na3SbSe4 (Fa structure) obtained using (a) GGA and (b) HSE06 with fatband representation showing atomic orbital associated with energy levels.

gap of ~1.5 eV similar to Cu_3PS_4 and HSE06 increases the band gap to ~2.5 eV. The bands are rather narrow compared to the Cu compounds because the lattice constant for the Na compound is 6.29 Å compared to 5.73 Å for the Cu compound. Also the distance between Sb and nn Se decreases from 2.65 Å in the Cu compound to 2.49 Å in the Na compound. This leads to a stronger interaction between V and VI atoms leading to a larger band gap in Na_3SbSe_4. Another interesting feature shows up, clearly due to the absence of d-levels, other bands split off from the Se-p bands but pushed below. This band has strong Sb-p character indicating a strong mixing between the Sb-p conduction bands and the Se-p valence bands. A closer examination of the band structure of the Cu compounds also shows this feature.
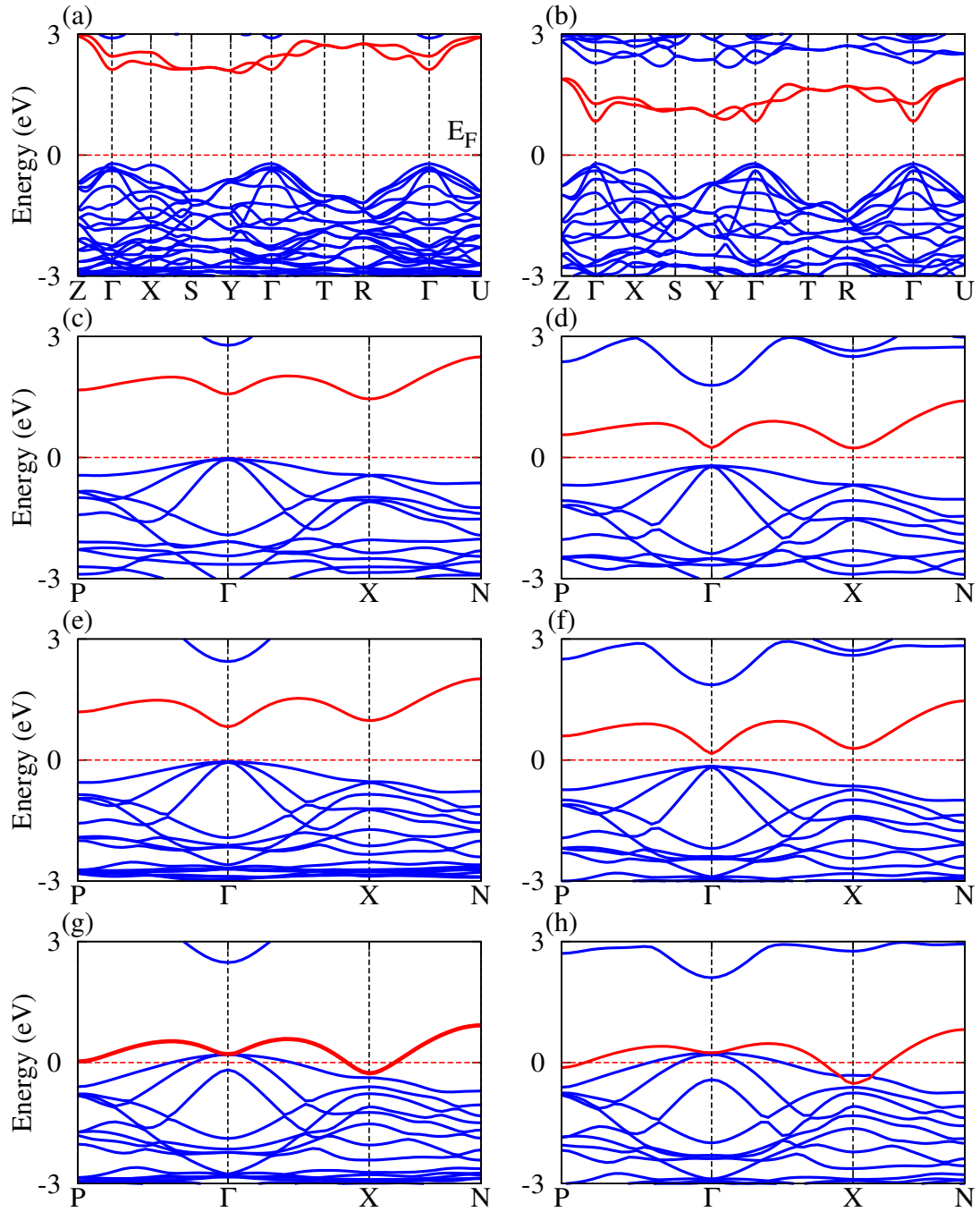
Figure 4.13: HSE06 bandstructure of (a) Cu_3PS_4 (b) Cu_3PSe_4 (c) Cu_3AsS_4 (d) Cu_3AsSe_4 (e) Cu_3SbS_4 (f) Cu_3SbSe_4 (g) Cu_3BiS_4 and (h) Cu_3BiSe_4. Where the first two compounds are En and the rest compounds are Fa.
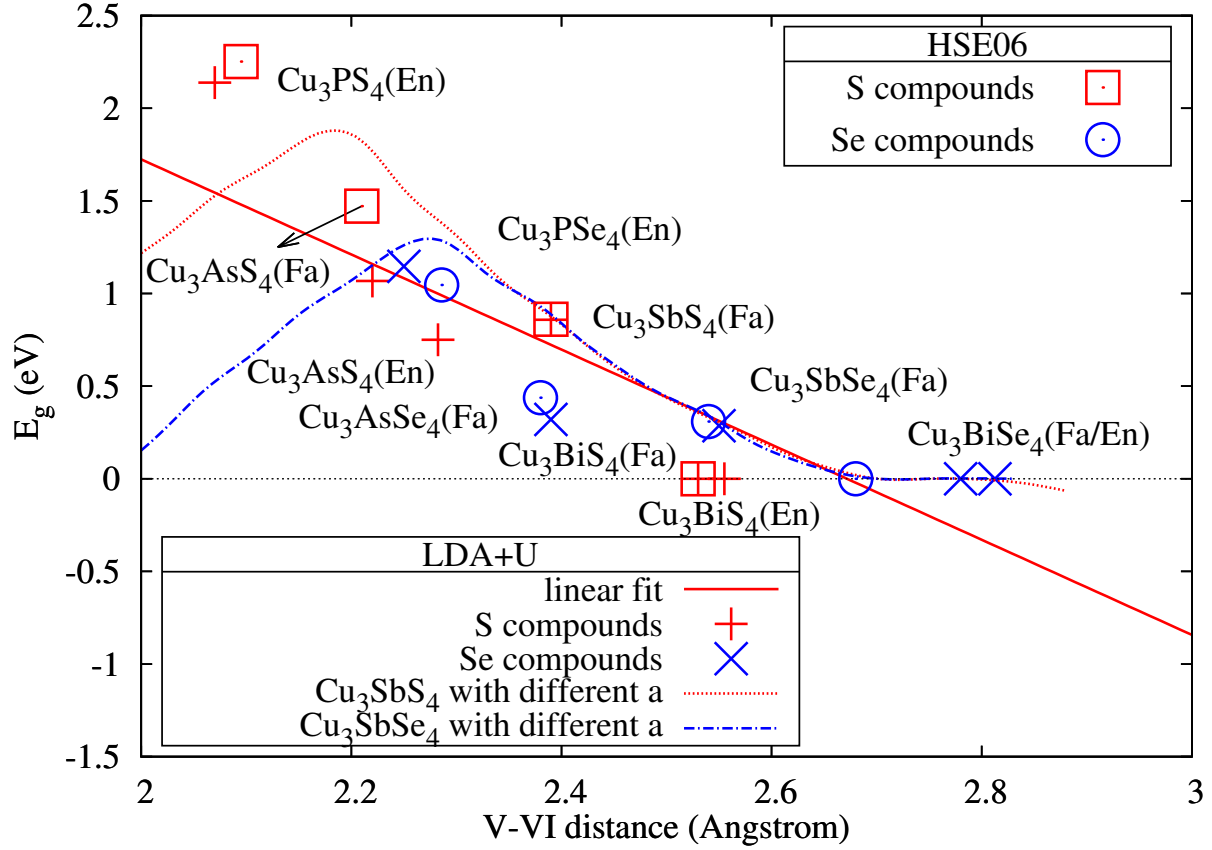
Figure 4.14: Band gap as a functions of V-VI distance for Fa and En: a comparison between GGA+U and HSE

4.4.3 Effect of non-local exchange

As discussed above, even though GGA+U can give good understanding of the electronic structure of Fa and En in the vicinity of the Fermi level, the non-local exchange interaction is important, and it is always a good idea to check GGA+U result using hybrid functional calculation. Especially, I would like to address the band structure of the two compounds containing Bi, Cu_3BiS_4 and Cu_3BiSe_4. Both GGA (Fig. 4.9g,h) and GGA+U (Fig.4.10g,h) did not give a gap. The HSE band structures of Fa and En are given in Fig. 4.13. Indeed, the results obtained from HSE calculations confirm the features of band structures produced by GGA+U. For the two Bi-compounds, there is no gap opening and both these compounds are semimetals and the band structures are similar to those obtained from GGA+U.
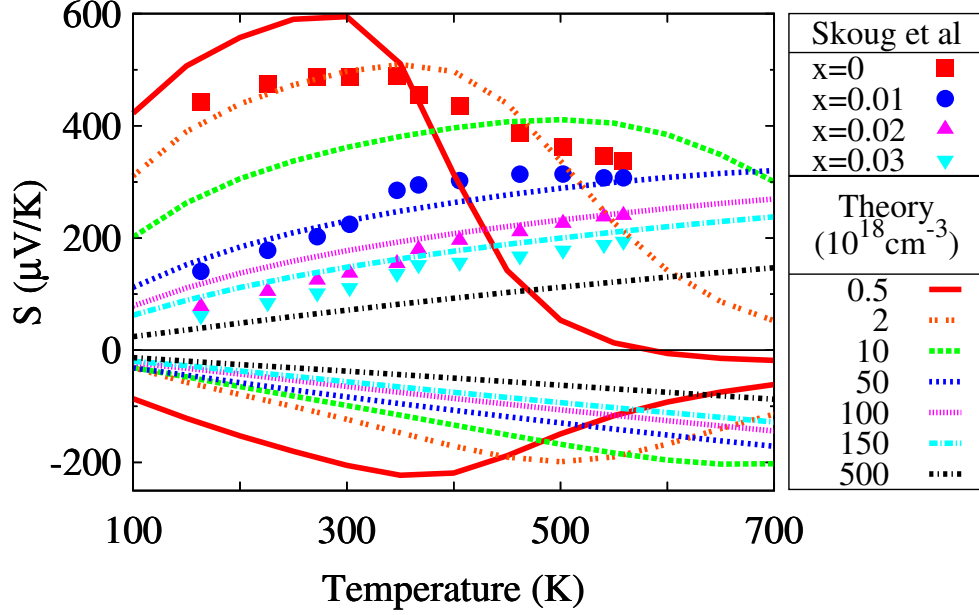
Figure 4.15: Theoretical seebeck coefficient (negative means *n*-type, positive means *p*-type) of Se4 using Boltzmann's equation for different carrier concentration (10^{18}cm^{-3}) together with experimental data reported by Skoug *et al.* [106] in the similar range of doping levels. *x* is the excessed holes per unit cell, $x = 0.01$ corresponds to hole concentration of 50×10^{18} cm^{-3}.

Indeed, figure 4.14 show that the relation between band gap and V-VI bond length from HSE calculation is almost identical to that which is discussed for GGA+*U* previously. This agreement, again, confirms that one can use GGA+*U* with an effectively chosen *U* to obtain reasonable results while using much less computational resources than that needed for HSE calculations.

4.5   Thermopower calculation of Cu$_3$SbSe$_4$

Once the electronic structure is understood, the thermoelectric properties, particularly thermopower, of materials can be easily obtained using Boltzman's transport equation. And since the band structures are similar between members of Fa and En, with the exception of the band gaps, one can study one system and extrapolate the results to the other. For example, a compound with a larger band gap than that of the studied one would be expected to have thermopower saturating at a higher temperature since it requires higher higher energy for the cancellation effect of excited electron-

hole to occur. By looking at the band structure, one can also deduce that Fa and En would be better *p*-type thermoelectrics since there is a three-fold degenerate band with different effective masses at the top of the valence band. It is indeed the case as will be shown latter on.

We choose to study Se4 compound which is extensively studied in experiment with which we will compare our calculated results. With the band structure obtained from HSE06 calculations using $\alpha = 0.25$ and $21 \times 21 \times 21$ **k**-mesh, we calculate thermopower (*S*) as a function of temperature (*T*) for different electron (*n*) and hole (*p*) concentrations in the range 0.5-500 (in the unit of $10^{18}/cm^3$) (Fig. 4.15).

In the *p*-doped Se4, at 300 K, *S* is about 600 μV/K for hole concentration *p*=0.5 and decreases to $\sim$100 for *p*=150, where concentration is given in unit of $10^{18}cm^{-3}$. This behavior agrees with experiment by Skoug *et al.* [106] For fixed *p*, the present calculation shows reasonable agreement with experiment by Skoug *et al.* [106] in terms of both the magnitude and the temperature dependence but not with Yang *et al.* [109] (Figure 4.15). For a similar doping level Yang *et al.* get a much lower thermopower than Skoug *et al.* and our calculated values. This suggests that their samples have, perhaps, larger hole concentrations due to defects (most likely Se vacancies).

S increases with *T* up to 700 K for high concentrations (*p*=50, 100 and 150) which agree with doping level of x=0.01, 0.02 and 0.03 of Skoug *et al.* [106]. However, for *p*≈0.5, which corresponds to nominally undoped sample, Skoug *et al.* [106] found that *S* peaked around 500 μV/K at 300 K and decreased slowly with *T* reaching a value of $\sim$300 μV/K at 500 K, while one finds in theoretical results a dramatic drop from $\sim$600 μV/K at 300 K to $\sim$80 μV/K at 500 K as a result of electron-hole excitations. This discrepancy might be caused by various reasons. One of them may be the pinning of the chemical potential around its 300-K value due to the creation or stabilization of defects. This assumption is consistent with the hole-concentration measurement showing an increase of *p* with *T*. [106]

Comparing Se4 and Se3 (done by Sevik and Çağin [108]), from a cursory look at their band structures (Figure 4.3), one expects that Se4 should have large *S* values in the *p*-doped regime due to heavy holes and large degeneracy. On the other hand, Se3 should be a better *n*-type thermo-

electric because of flatter conduction band with multiple minima. These expectations are indeed observed in our calculations. For $p=10$, the maximum values of S are obtained at the same temperature ($\sim$500 K) for both Se4 and Se3. However the value is larger in Se4 (400 μV/K) than in Se3 (300 μV/K). Thus Se4 is a better p-type thermoelectric. In contrast, for n-doping the maximum $|S|$ in the concentration range $1 < n < 100$, is $\sim$200 μV/K in Se4 whereas it is around 450 μV/K in Se3, making the later a much better n-type thermoelectric. Unfortunately, to the best of my knowledge, there are no published thermopower measurements in n-doped Se3 and Se4 to confirm the calculated results.

4.6 Summary

In this chapter, I have discussed the electronic structures of valence compensated ternary compounds given by the formula I_3-V-VI$_4$ which belong to the family of Famatinite and Enargite. Particular attention is given to Cu_3SbSe_4 compound for its interesting properties reported experimentally. The calculations reveal that even though one can look at these compounds as derivatives of Zinc blende or Wurtzite strucutre, which have been extensively studied and are quite well understood, the electronic properties of Famatinite and Enargite compounds are quite different.

First of all, unlike the monoatomic and binary tetrahedrally bonded compounds, the simple octet rule cannot be applied to Famatinite and Enargite family, or other diamond-like ternary compounds. It is shown that V ions are primarily in the 3+ valence state, not 5+ as one would infer from naive valence counting, verifying that there exist lone pair of electrons on the V site. The effect of the local bonds as well as the role of V lone-pair electrons on the band structure are discussed. V lone pair electrons strongly interact with the surrounding VI-p orbitals, giving rise to the special BOI (single band in Famatinite and two bands in Enargite) which play the role of the lowest conduction band. V lone pairs are directly involved in the band gap formation. On the other hand, the filled d-shells of Cu contribute indirectly in the band gap, only through changing the bonding nature and bond length between V and VI atoms.

By comparing the electronic structure of a large number of ternary I_3-V-VI$_4$ systems using dif-

ferent methods (local and non-local), we bring out the importance of the non-local exchange in gap opening. My calculations, however, also show that GGA+U (with an appropriately chosen value of U, about 15 eV) can reproduce extremely well the electronic structure near the gap. This method is still very useful in surveying a wide range of materials, giving useful insight to understand the physics of materials.

Results also suggests that one can easily tune the band gap to a desirable value by choosing proper constituent or doping elements.

Famatinite and Enargite are expected to be better p-type thermoelectrics due to large degeneracy of the valence bands. Study of Cu_3SbSe_4 shows that the band gap and thermopower values in p-doped Cu_3SbSe_4 agree very well with experiment,[106, 110, 111] showing that Se4 should be a better p-type thermoelectric thermoelectric.

This work gives a foundation for further study of tetrahedrally bonded ternary materials, for example to investigate the electronic structure of defects in these compounds.

CHAPTER 5

HALF-HEUSLER–HEUSLER COMPOSITE

5.1 Introduction

Half-Heusler and Heusler compounds have been of great interest for several decades for thermo-electric, magnetic, half-metallic and many other interesting properties. Development in the study of this family of compounds can be found in several review articles,[85, 126–133] among which Graf et al. [85] gave a quite comprehensive overview of the field. An interesting example of such compounds is Zr-Ni-Sn, a promising thermoelectric material.[134–150] They can go from semiconducting half-Heusler (HH)[139] limit, ZrNiSn with cubic MgAgAs structure, to metallic Heusler limit (some times referred to as full-Heusler, FH), $ZrNi_2Sn$[139] with cubic MCu_2Al-type structure, where M=Zr,Ti,Hf. Because of their excellent thermoelectric properties, ZrNiSn and related HH systems, TiNiSn and HfNiSn, and their solid solutions have attracted considerable ex-perimental and theoretical interest over last several years.[23, 140, 142, 143, 148–166] The idea of going from HH to FH limit in other systems has also been tried. In the Ti-Co-Sn system for example these two phases represent the edge members of the solid solution $TiCo_{2-x}Sn$, where the electrical conductivity changes from semiconducting to metallic as one decreases x from 1 to 0.[167]

Recently Makongo et al. [23, 157] have come up with an exciting observation, which shows that large enhancements of both thermopower and electrical conductivity (hence the powerfactor PF) of half-Heusler (HH) phases of (Zr,Hf)NiSn can be achieved at high temperatures through in-sertion of nanometer scale FH coherent inclusions within the HH matrix, caused by adding a small concentration of extra Ni atoms. They denoted these systems as HH$(1-x)$/FH(x) nanocomposites which can be alternatively characterized as $ZrNi_{1+x}Sn$, where $0 < x < 1$. As shown in Fig. 5.1, in Bi-doped HH(0.94)-HF(0.06) they found a PF of 3.3 mW/mK^2 compared to 1.6 mW/mk^2 for
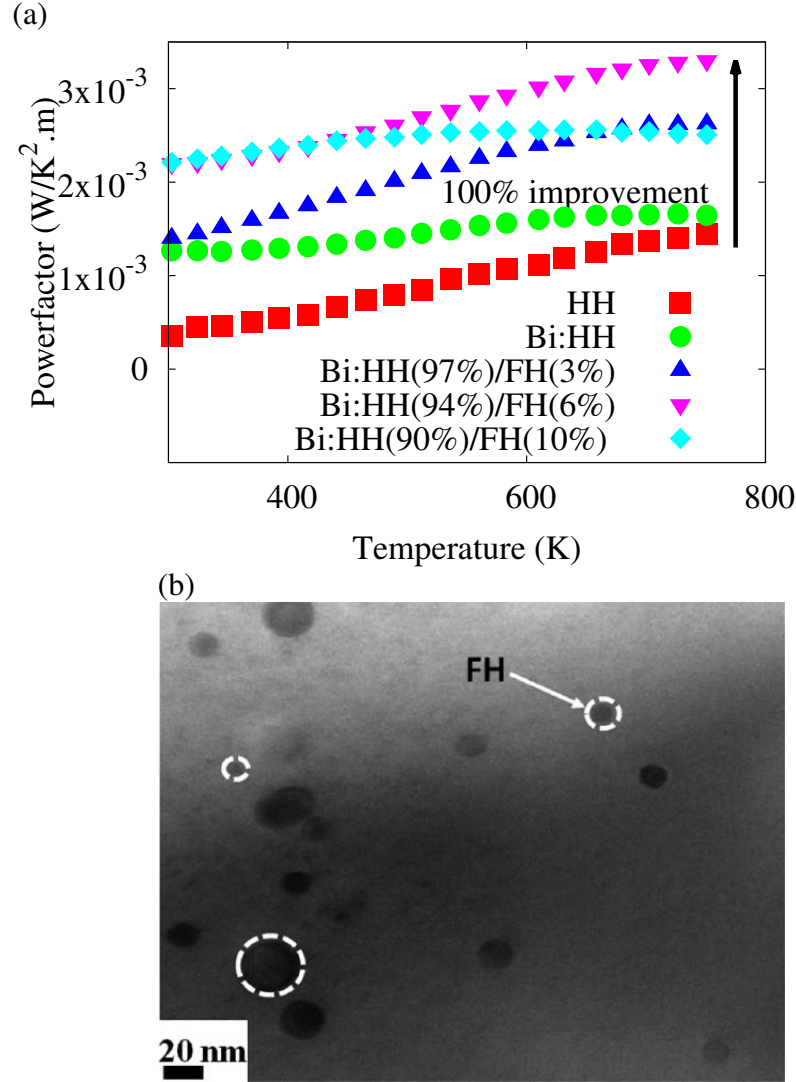
Figure 5.1: (Source: Makongo et al. [23]) Improvement of powerfactor (PF) (a), and TEM image showing FH-nano-inclusions in HH(b)

simply Bi-Doped HH around 700 K. Chai and Kimura [160] also saw a large density of nanosized FH precipitates within HF matrix in slightly Ni rich TiNiSn alloys and found an increase in the power factor at high temperatures ($S^2\sigma \sim 3.5$ mW/mK^2 at 700 K compared to $\sim$2.5 mW/mK^2 at the same temperature for the parent compound TiNiSn[153]). They ascribed an energy filtering mechanism proposed by Faleev and Léonard [22] to explain this enhancement. The basic idea behind this filtering mechanism is to reduce the commonly observed electron-hole cancellation effect in thermopower by selectively allowing only one type of carrier to transport energy and charge. There is however no direct evidence of such energy filtering in the presence of FH nano particles;

(a)

(b)
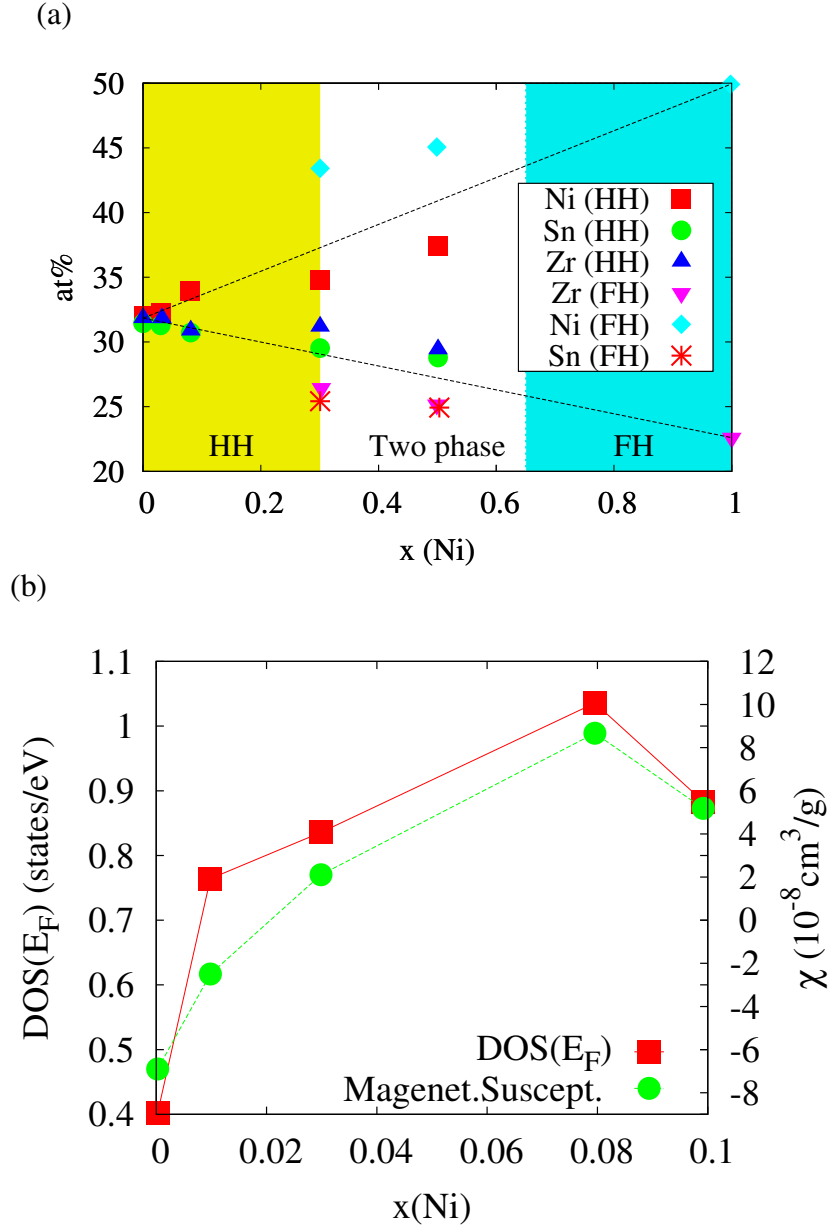
Figure 5.2: (Source: Romaka et al. [149]) (a) Phase diagram of HH-FH mixture, (b) Comparison between measured susceptibility and density of state calculated using Korringa-Kohn-Rostocker method with coherent potential approximation and local density functional (KKR-CPALDA)[168].

more careful studies of electronic structure are needed to support this idea.

More recently, Romaka et al. [149] have carried out a thorough investigation of structural phase transitions in half-Heusler - Heusler stannides $(Zr,Hf)Ni_{1+x}Sn$ and have shown how different physical properties change as one goes from HH to FH limit. They found that in $ZrNi_{1+x}Sn$,
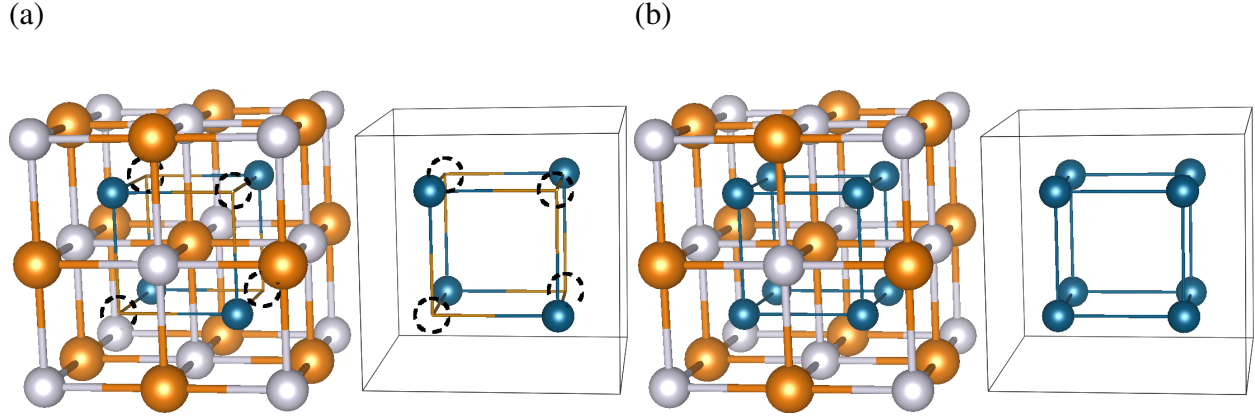
Figure 5.3: Crystal structure of (a) Half-Heusler (HH) and (b) Full-Heusler (FH) compounds, where Zr (orange circles) and Sn atoms (gray circles) form a NaCl sub-lattice, inside which there are 8 small cubes. HH is formed by filling every other cube with Ni atoms (blue circles), while FH is formed by filling all the cubes. The empty-cube sites (quasi-particle of Ni-vacancy) in HH is presented by a dashed-line circle.

macroscopic phase separation of HH and FH phases takes place in the region $0.3 \leq x \leq 0.7$ (see Fig. 5.2a). Their average XRD measurements matched very well to the cubic MgAgAs structure for $x \leq 0.3$ and to the cubic MCu_2Al-type structure for $x \geq 0.7$. However the presence or absence of nanostructures of one phase in the matrix of the other phase in these concentration ranges ($x \leq 0.3$ or $x \geq 0.7$) could not be established. One intersting result, relevant to this theis, is that for $0 < x < 0.1$, Romaka et al. [149] found and increase in the density of states (inferred from susceptibility measurement – Fig. 5.2b) suggesting that new states appear at the Fermi-energy with increasing x. They also reported a theoretical DOS, calculated using Korringa-Kohn-Rostocker method with coherent potential approximation and local density functional (KKR-CPALDA)[168], in good agreement with the susceptibility measurement. However, one has to note that KKR-CPA method considers the excess atoms to be distributed randomly in the host matrix, thus, it cannot address the effect of nanostructure on the electronic structure.

One can visualize the structure of these HH and FH compounds as follows (Fig. 5.3). One starts from a NaCl-type lattice of (Zr,Hf)Sn consisting of two interpenetrating FCC sub-lattices. Inside the large cubic unit cell of length a, there are 8 small cubes of length $a/2$. In (Zr,Hf)NiSn, the centers of 4 out of these 8 cubes are occupied by Ni atoms so that each (Zr,Hf) or Sn is

tetrahedrally bonded to 4 Ni atoms. The other 4 small cube centers are empty. In $(\text{Zr,Hf})\text{Ni}_2\text{Sn}$ all the 8 small cube centers are occupied by Ni atoms. Thus one can tune from HH to FH or vice versa by varying the amount of Ni. Due to the additional Ni, FH compounds have an additional inversion symmetry compared to HH. The lack of mutual solubility of the HH and FH phases with similar crystal structures (as seen in Fig. 5.3) is quite remarkable in view of the fact that one can start from one structure and either add or remove Ni atoms to reach the other structure without changing the basic structure of the ZrSn matrix. Note that the lattice constants are however slightly different between HH and FH (6.15 Å and 6.32 Å respectively).

There are several fundamental questions that arise in the study of these mixed HH-FH systems, for example in $\text{ZrNi}_{1+x}\text{Sn}$, such as: what is the nature of the phase diagram in the $\text{ZrNi}_{1+x}\text{Sn}$ in the T vs x plane? what are the short and long range structural features and how they change with x? what are the electronic and lattice properties of the mixed system? There are several recent works on related issues: Romaka et al. [149] have addressed the electronic structure issue using LDA-single site CPA approximation[168]; Kirievsky et al. [164] have studied the thermodynamics of Ni-rich TiNiSn compound, i.e. the phase separation and energetics of antisite defects in the simple cubic supercell of the relevant system. However, as pointed out earlier, CPA approximation used by Romaka et al. [149] cannot address the clustering of nanostructure and the simple cubic supercell used by Kirievsky et al. [164] in their electronic structure calculations is too small. I will discuss some of their results later in this thesis. In this work I address two of these basic issues. First, do the additional Ni atoms (or Ni vacancies) go randomly to the empty (or occupied) cube sites or form some sort of local ZrNi_2Sn (or ZrNiSn) nanoclusters? Second, what is the effect of these nanoclusters, if they form, on the electronic structure and vice-versa. In order to address these questions I have carried out electronic structure calculations using *ab-initio* density functional methods and quasi-periodic model[169] to describe the nanostructures.

The structure of this chapter is as follows. In Sec. 5.2, I discuss briefly some of the details of electronic structure calculations and the model to describe the nanostructures, beyond which already discussed in chapter 2. In Sec. 5.3, I discuss the energetics of nanoclustering and the

electronic structure, focusing on the nature of the gap states as one adds Ni atoms to ZrNiSn or the modification in the density of states near the Fermi energy as one adds Ni-vacancies to $ZrNi_2Sn$. Finally, in Sec. 5.4, I present a summary of my main findings and discuss further work in this area.

5.2 Methods of electronic structure calculation and modeling nanostructures

It is well known that LDA/GGA calculations usually underestimate the band gaps in semiconductors (as discussed in Chapter 2 as well as seen in Fe_2VAl (Chapter 3) and Cu_3SbSe_4 (Chapter 4)), however, the problem is opposite in the case of MNiSn (M=Ti, Zr, Fh)[139, 170] where the LDA calculations predicted a band gap of ~ 0.5 eV, two times larger than that of found from resistivity measurements[135] ($E_g = 0.12, 0.18$ and 0.22 for M=Ti, Zr and Fh respectively). I have tested the case of ZrNiSn with approximations on higher rung of DFT (Fig. 2.2), i.e. hybrid functional HSE06, and have found the problem worsen (E_g=0.58 eV). Thus, in this chapter all total energy and electronic structure calculations were done using density functional theory (DFT) within generalized gradient approximation (GGA). For the exchange-correlation potential we used the model suggested by Perdew, Burke, and Ernzerhof (PBE).[47] We employed projector-augmented wave (PAW) method[75, 76] as implemented in the VASP code.[77–79] with a plane-wave energy cutoff of 400 eV and an energy convergence criterion (between two successive self-consistent cycles) of 10^{-4} eV (total energy/unit cell).

To study the evolution of HH-HF we have done calculations for $ZrNi_{1+x}Sn$, where $x = 0 - 1$, using the supercell method.[169] At $x = 0$ and $x = 1$ we have pure HH and FH compounds respectively. The supercell method has been used by Kirievsky et al. [164] for $TiNi1 + xSn$, however, with simple cubic $1 \times 1 \times 1$ cell (maximum 8 Ni atoms per unitcell) which gives a very large concentration of defects. They focused primarily on the thermodynamics of the HH-HF mixture and the quasi-binary-system phase diagram. Here, I use a larger unitcell, $2 \times 2 \times 2$ (maximum 64 Ni atoms per unitcell) to reduce the interaction between defects in neighboring cells and focus on the formation of nanostructure of FH (HH) in HH (FH). I study the dilute limit of the defect (i)

starting from the HH structure and then adding more Ni atoms to create the FH inclusion and (ii) starting from the FH structure and then removing some Ni atoms to create HH inclusion. I use the notation HH+nNi (FH-nNi) to refer to a $2 \times 2 \times 2$ super cell of HH with n additional Ni (FH with n deficient Ni). For the HH end, to study how the FH phase forms, I tried all possible configurations of excess Ni-pair and looked for the lowest-energy (the most favorable) configuration; once the preferred pair-configuration was found, I added the third Ni and, again, looked for the lowest energy configuration. An analogous procedure was applied for the FH end with Ni vacancies.

In all the calculations, structures were allowed to relax. The lattice parameters of HH and FH are found to be 6.15 Å and 6.321 Å respectively. The defective structures, then, were derived from the host structures and ionic positions were allowed to relax. The charge densities and total energies were calculated self-consistently with an $8 \times 8 \times 8$ Monkhorst-Pack[171] **k**-grid. The electronic density of states (DOS) was then obtained using a denser **k**-mesh ($12 \times 12 \times 12$), from the self-consistent charge density and wavefunction.

In studying properties of defects in a material, it is useful to calculate the formation energy of the defect. There are extensive theoretical studies which have been dedicated to this problem. Here I follow the work of Zhang et al. [172]. Applying to HH-FH, the formation energy of a defect can be calculated by

$$\Delta H_f(X) = \Delta E_f(X) + n\mu_{\text{Ni}}, \tag{5.1}$$

where

$$\Delta E_f(X) = E(X) - E(0) + nE_{\text{Ni}}. \tag{5.2}$$

In these equations, $E(X)$ and $E(0)$ are the ground state energies of a system with defect X and that of the host system respectively, n is the number of Ni added ($n < 0$) or removed ($n > 0$) from the host-system (HH or FH), E_{Ni} is the ground state energy of Ni solid, and μ_{Ni} is the chemical potential of Ni. μ_{Ni} is usually considered as a parameter which can vary from Ni-rich to Ni-poor environment. The limit of μ can be defined from thermodynamic equilibrium conditions which was carefully discussed by Zhang et al. [172].

Table 5.1: Formation energies (eV) of HH-FH systems (for the lowest energy configurations)

	HH+1Ni	HH+2Ni	HH+3Ni	HH+4Ni	FH-1Ni	FH-2Ni
$\Delta E_f(X)$	0.423	0.758	1.083	1.372	0.417	0.789

5.3 Results and Discussions

5.3.1 Formation energy and energetics of clustering

5.3.1.1 HH with excess Ni

Table 5.1 gives the energies needed to add (or remove) Ni to (from) HH or FH. For simplicity, only $\mu = 0$ is considered because the differences (not the absolute value) in energies are the studied. All the energies are positive, which means it costs energy whenever a Ni is added or removed from HH or HF systems. The energy required to add one Ni to HH host (0.423 eV) is slightly higher than that needed to remove one Ni from FH matrix (0.417 eV). When the second Ni is added to HH, the needed energy is smaller than that for the first one ($0.758 - 0.423 = 0.335$ eV), and so on for the third Ni. The similarity is seen at the FH end. When more than one Ni is added to HH or taken out of FH, the minimum energy configuration was found by varying the positions of the extra Ni atoms or vacancies.

With the first excess Ni's (Ni_1) is fixed, when the second Ni (Ni_2 is added to the HH matrix, there are several possible empty cube sites that it can occupy. In Figure 5.4(left column) we plot the ground state energy of HH+2Ni as a function of the distance between the added Ni-pair (Ni_1 and Ni_2). It is clear that two Ni are attracted, since the energy is lowest at the smallest distance (4.22Å). The structure of the preferred positions of Ni is shown in figure 5.4, right column. The ground state energy increases as the distance increases and then saturates at large distances, when the distribution of excess Ni is more homogeneous over the space. The energy difference between the lowest- and the highest-energy states is about 0.1 eV.

The saturation of the energy at large distance is due to the finite size of the periodic super-
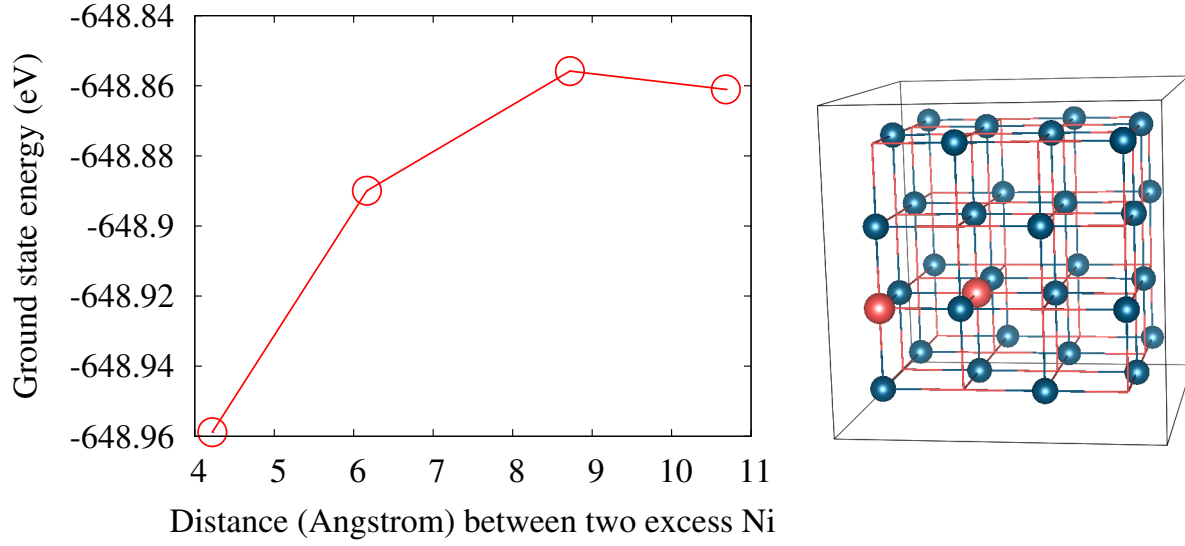
Figure 5.4: Left column presents energetics of two extra Ni in HH: energy vs. distance. Right column presents the preferable configuration of the excess Ni (orange circle) (only Ni matrix (blue circles) is shown).

cell. Even with a $2 \times 2 \times 2$ unit cell, the size is only $12.3\text{Å} \times 12.3\text{Å} \times 12.3\text{Å}$, there is an artificial periodicity of the defects. At large distance, the interaction between Ni_2 (Ni_1) with Ni_1 (Ni_2) in the neighboring unit cells compensates the interaction between those in the same unit cell. For a bigger unit cell, one should expect the saturation at a larger distance.

When the third Ni (Ni_3) is added to HH, the problem is a little bit more complicated. For convenience, we determine the position of Ni_3 using the polar coordination (r, θ) with respect to the Ni_1-Ni_2, where the origin is at Ni_1 and the x axis is along the Ni_1-Ni_2 bond.

Fig. 5.5(left column) plots the relative positions of Ni_3 in the Ni_1-Ni_2 reference with the ground state energy presented in color code varying from dark purple (low value) to yellow (high value).

Table 5.2: Ground state energy as a function of Ni_3's relative position with respect to Ni_1-Ni_2

r(Å)	4.349				6.151	7.533		8.699	10.654
θ(°)	60	90	120	180	90	73.22	90	120	90
E (eV)	-654.14	-654.10	-654.08	-654.06	-654.03	-654.03	-653.99	-653.99	-654.00

106
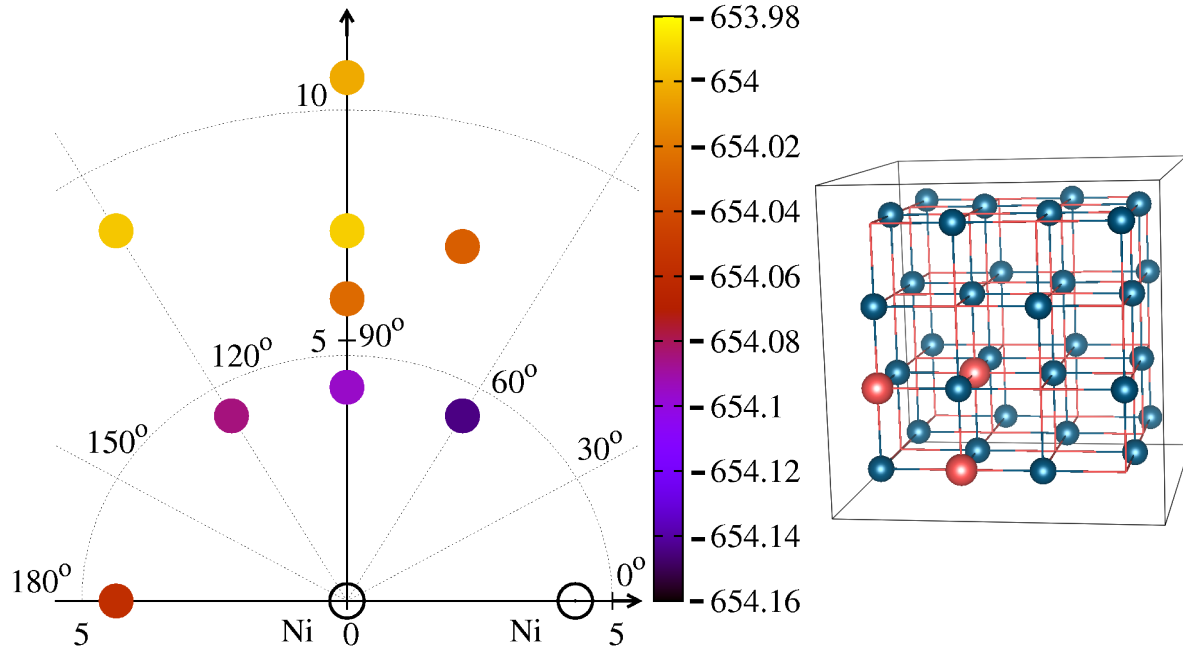
Figure 5.5: Left column presents energetics of three extra Ni in HH: position of the third Ni (Ni_3) is given in polar coordinate, with respect to Ni_1-Ni_2, whose positions were previously determined by studying the energetics of a pair of excess Ni (FIG. 5.4). Ground state energy of each configuration is represented by color code from low (purple) to high (yellow) energy. Right column shows the preferred configuration of the Ni_3 (only Ni matrix (blue circle) is shown). The excess Ni are orange circles.

The value of the ground state energy of each configuration is given in table 5.2. The results confirm the attractive interaction between 3 excess Ni atoms, similar to which found for a pair of excess Ni. For the same r, the energy, in general, increases with increasing θ. For instance, for the smallest distance, $r = 4.349$, the ground state energy is -654.14 eV at $\theta = 60°$, whereas it is -654.06 eV at $\theta = 180°$. Similarly, for the same θ the ground state energy increases with increasing distance. The maximum energy difference between two configurations is about 0.14 eV.

Similar to the case of Ni-pair, with 3 excess Ni, the ground state energy also saturates at large distance, and for the same reason (periodic supercell).

The lowest ground state is found for Ni_3 at (4.34Å, 60°), where Ni_3 is closest to both Ni_1 and Ni_2; the crystal structure of this configuration is given in Fig. 5.5(right column). Excess Ni atoms tend to come close to each other and form a nano-cluster of FH in the HH matrix.

107
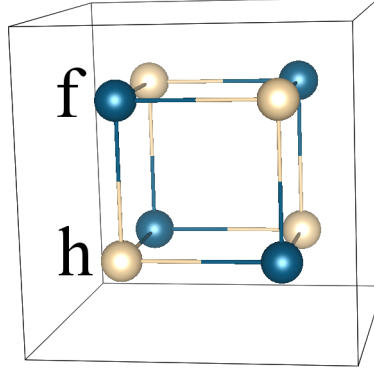
Figure 5.6: Conventional notations for Ni-sites: "f" for Ni at (1/4,1/4,1/4) and equivalent atoms (dark blue), "h" for Ni at (3/4,3/4,3/4) and equivalent atoms (bright yellow).

The results strongly support the HH-FH phase separation observed in experiments[23, 149, 158–160, 163] In experiment, however, the phase separation is only observed at a high concentrations of Ni, for example, Romaka et al. [149] showed that the two macroscopic phases of $ZrNi_{1+x}Sn$ can be seen only within the range of $0.30 < x < 0.65$ (Fig. 5.2a). The present results, on the other hand, predict that the nanostructures of FH form in a HH matrix, at least at low temperature, even at small concentrations of excess Ni($x \sim 0.1$, or 3 excess Ni in 32 host Ni), thereby supporting the ideas put forward by Makongo et al. [23]

5.3.1.2 FH with deficient Ni

At the FH end, one should note that there are two different Ni-sites: "h"-site (h) at (1/4,1/4,1/4) and its equivalent, which is occupied by Ni in HH, and "f"-site (f) at (3/4,3/4,3/4) and its equivalent, which is empty site in HH (Fig. 5.6). When removing Ni, the Ni-vacancy can be located at either of these two sites.

If one Ni is removed, due to symmetry, two sites are equivalent. The energy cost for removing 1 Ni out of $2 \times 2 \times 2$ unit cell is ~ 0.417 eV. Similar to the case of HH+nNi, the energy cost to remove the second Ni (to add the second vacancy) is smaller than that needed to remove only one Ni (Table 5.1). When 2 Ni are removed, for the convenience, the first vacancy (V1) is assumed to be at a f site, the second one can be at either h or f site. We denote the pair of vacancies by

(a)
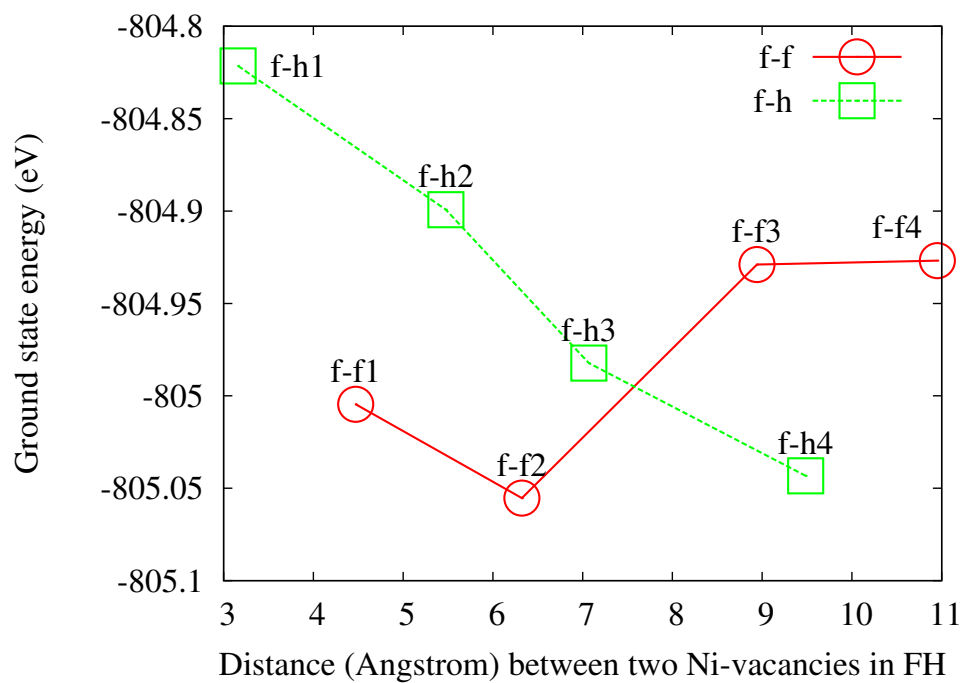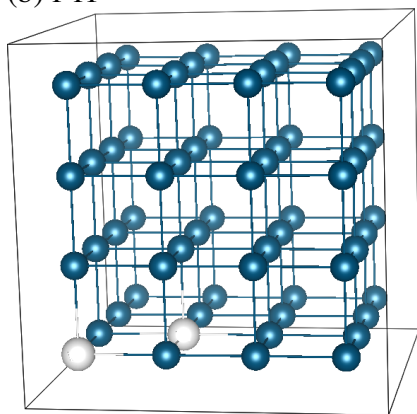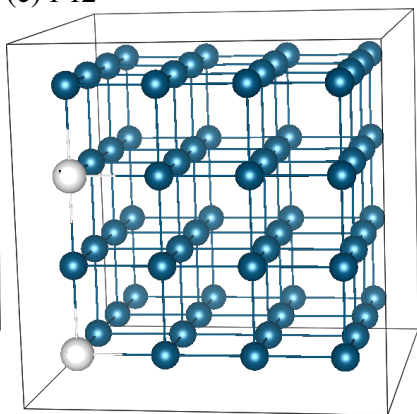
(b) f-f1   (c) f-f2   (d) f-h4
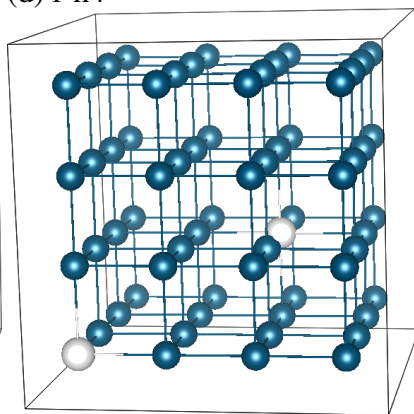
Figure 5.7: The top figure shows energetics of FH with two Ni-vacant sites (white circles); the bottom shows structures of the three most preferable configurations, which have ground state energies close to each other: (a) f-f1, (b) f-f2, and (c) f-h4. Only Ni matrix (blue circles) is shown.

the name of the sites which they occupy,i.e. f-f and f-h, note that f-f and h-h are equivalent. In Fig. 5.7(a), we plot the ground state energies as a function of the distance between 2 Ni-vacancies, considering f-f and f-h separately. Fig. 5.7(a) shows that f-f and f-h are energetically different.

For the f-h case, the interaction between two vacancies is repulsive,i.e. the total energy is the lowest for the largest distance. The relation between energy and distance is almost linear. The difference between the lowest and the highest energies is about ~ 0.22 eV. For the f-f case, in contrast, the interaction between the two vacancies is, in general, attractive, the smaller is the distance, the lower is the energy. There is, however, a competing effect between repulsion and attraction at small distance, which makes the ground state energy higher at the smallest distance, 4.47Å (f-f1), than at the larger one, 6.32Å (f-f2) (-805.00 eV for f-f1 compared to -805.055 eV for f-f2, as shown in Fig. 5.7(a)). The energy saturates at large f-f distance.

The structure of f-f2 (Fig. 5.7(c)) has 2 Ni-vacancies distributing evenly at the every other site along lattice axis (say x), forming a quasi one dimensional chain. This structure is similar to the configuration (i) in reference [164], except that they put one vacancy in $1 \times 1 \times 1$ simple cubic super cell, thus it forms a 3-dimensional ordered structure. In their work, Kirievsky et al. [164] calculated electronic structures of 11 configurations with different fraction of Ni over the eight cubic site in TiSn matrix and studied their energetics using a quasi binary model $(TiNi_2Sn)_c(TiSn)_{1-c}$, where the formation energy is given by

$$\Delta U = E_{tot}^{mixture} - (c \cdot E_{tot}^{TiNi_2Sn} + (1-c) \cdot E_{tot}^{TiSn}), \tag{5.3}$$

where E_{tot} is the total energy of corresponding system. They found that the configuration (i), $c = 0.875$, had negative free-energy of formation whereas most of the other configurations (except $c = 0.5$ which corresponds to Half-Heusler phase TiNiSn) have positive free-energy of formation. One should note that the definition of formation energy use by in reference [164] is different from the definition used in this thesis. Furthermore, they have used a $1 \times 1 \times 1$ supercell where the periodic cell constraints are much significant. Thus, it is not practical to directly compare values of formation energies between two works.
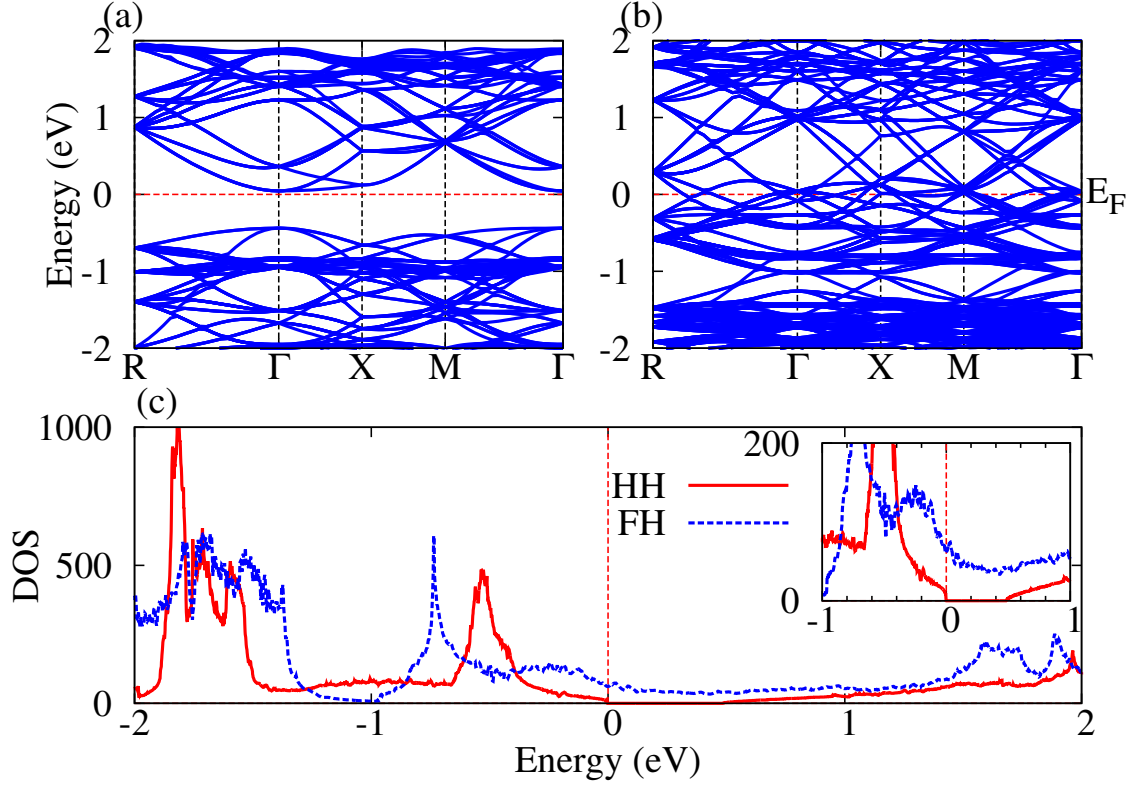
Figure 5.8: Band structures of (a) HH and (b) FH in the Brillouin zone (BZ) of $2 \times 2 \times 2$ cubic supercell; and (c) the density of states (DOS) within energy range [-2,2]; in the onset, we zoom in the range [-1,1] to show the fundamental difference between HH and FH: the former is metal whereas the latter is semiconductor, with a band gap ~ 0.5 eV.

It is interesting that the ground state energy of f-f2 (the lowest energy among f-f) is about ~ 0.012 eV lower than that of f-h4 (the lowest among f-h) (see Fig. 5.7). Thus, f-f2 and f-h4 can coexist at $x = 0.9375$. This suggest a frustration of excess Ni-vacancies in the FH matrix.

To summarize, supercell calculations show that the energetics of FH-nNi is different from that of HH+nNi. In the former case, the Ni-vacancy tend to distribute almost evenly in spacealthough there is some suggestion for vacancy ordering. Thus, the nanostructure of the HH phase is not formed in FH at low vacancy concentrations, whereas in the latter case, excess Ni tend to form nano-clusters of FH in HH.

5.3.2 Electronic structure

Before we discuss the electronic structure of HH-FH mixture, let us first review the electronic structures of the end compounds ZrNiSn and $ZrNi_2Sn$. Electronic structures of ZrNiSn and $ZrNi_2Sn$ are well understood and were extensively studied both theoretically[139, 170] and experimentally[135, 136]. ZrNiSn is a semiconductor with an indirect band gap of ~ 0.5 eV[139, 170, 173] between Γ and X points in the FCC Brillouin Zone (BZ). The band gap is formed from the hybridization of Zr-d and Sn-p orbitals. The band gap formation was carefully discussed by Larson et al. [173]. Top of the valence bands are three-fold degenerate, one of which has a light effective mass while the others have heavier ones. On the other hand, bottom of the conduction bands is a non-degenerate band with anisotopic effective mass. All Ni-d and Sn-s bands are occupied, where the latter is located at about -15 eV below the valence band maximum. $ZrNi_2Sn$, on the other hand, is a good metal.

Fig. 5.8 gives the band structures of ZrNiSn (Fig. 5.8a) and $ZrNi_2Sn$ (Fig. 5.8b) in the Brillouin zone (BZ) of $2 \times 2 \times 2$ simple-cubic supercell, and the corresponding density of state (DOS)(Fig. 5.8c). Going from a fcc primitive unit cell to $2 \times 2 \times 2$ simple-cubic supercell, due to band folding – since the BZ is smaller in the larger cell – the band structure of ZrNiSn shows a direct (instead of indirect as in fcc) band gap or ~ 0.5 at the Γ point, in good agreement with other works[139, 170, 173]. The band structure of both ZrNiSn and $ZrNi_2Sn$ appear more complicated in the $2 \times 2 \times 2$ supercell since we have more bands in the first BZ. Fig. 5.8c shows comparison of the DOS of the 2 compounds, near the Fermi level. The inset shows the DOS close to the Fermi energy.

When extra Ni (Ni_1) is introduced into HH matrix (or removed from FH), there is a change in the electronic structure and a redistribution of the charge density with respect to the host system (HH or FH). To analyze this charge redistribution, we calculate the charge-density difference (charge-difference) $\Delta\rho = \rho^X(\mathbf{r}) - \rho^0(\mathbf{r})$, where $\rho^X(\mathbf{r})$ and $\rho^0(\mathbf{r})$ are the charge densities of the defective system and corresponding host system. Fig. 5.9 depicts the charge difference contour on the (-110) plane for HH+1Ni (Fig. (5.9a) and FH-1Ni (Fig. (5.9b), where blue indicates charge depletion and red indicates charge accumulation.
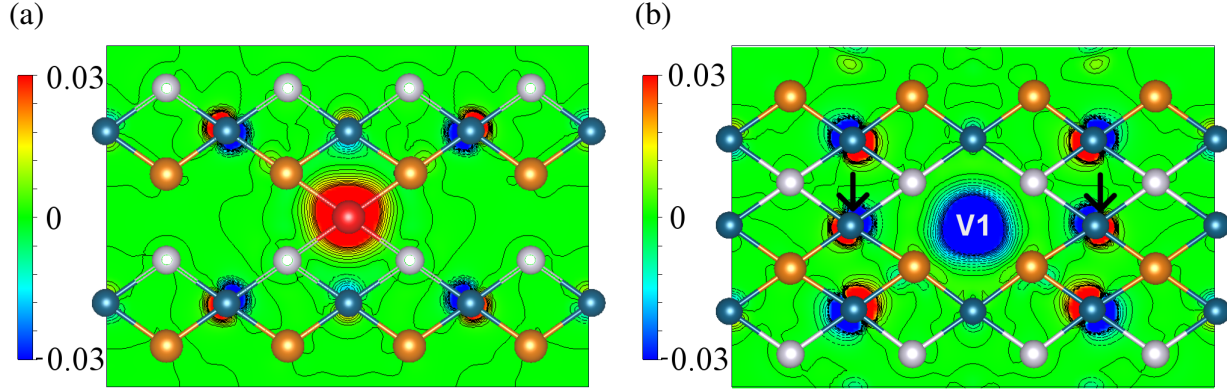
(a)

(b)

Figure 5.9: Charge difference between (a) HH+1Ni and (b) FH-1Ni and their parent compounds (HH and HF), where blue color indicates charge depletion whereas red color indicates charge accumulation. The figure show the contour plot on (-110) plane. Charge difference is defined as $\rho^X(\mathbf{r}) - \rho^0(\mathbf{r})$, where $\rho^X(\mathbf{r})$, and $\rho^0(\mathbf{r})$ are charge density of defective and pure system respectively. Host Ni are blue circles, excess Ni is red circle, Zr are brown circles, Sn are gray circles.

For HH+1Ni, the additional Ni introduces more electrons to the HH system, these electrons localize around Ni_1 (Fig. 5.9a). The additional electrons at the excess Ni site cause the rearrangements of charge in the neighboring space. However, this rearrangement occurs mostly at the Ni-sites. Electrons tend to move further away from Ni_1. In Fig. 5.9a one can clearly see the blue lobes at the Ni-sites are directed towards Ni_1, whereas the red lobes at the same sites are directed away from Ni_1. In Fig. 5.9 one sees that the Ni atoms of the host matrix (HH) connect to N_1 in directly through Zr or Sn, let us call these connections Zr- and Sn-channels. With those channels defined, one can realize that the charge rearrangements are not the same on all Ni, they are larger on Ni which interacts with the Ni_1 through only one channel, either Sn-channel or Zr-channel, where $Ni-Zr(Sn)-Ni_1$ form a straight line. The charge rearrangements on other Ni-sites, which connect to Ni_1 through two channels of the same type (either two Sn-channels or two Zr-channels), are smaller even though they may be at shorter distances with respect to Ni_1.

A similar picture is also seen in HF-1Ni (Fig. 5.9b), except that the removal of Ni (V1) takes away electrons. A subtle difference between FH-1Ni and HH+1Ni is that there is an interesting charge rearrangement on Ni indicated by arrows in Fig. 5.9b (hereafter it is called Ni_x). Ni_x indirectly connect to V1 through two channels, one Zr-channel and one Sn-channel, the Ni_x-Sn(Zr)-V1

Figure 5.10: Evolution of electronic structure of HH with excess Ni: band structures (a) HH+1Ni, (b) HH+2Ni, and (c) HH+3Ni, and (d) density of states of HH with 1, 2, 3 and 4 additional Ni.

angle is about $\sim 110°$. The charge rearrangement on Ni_x site does not occur on the Ni-V1 direction but on the Ni-Sn direction, as shown in Fig. 5.9b. The blue lobe around Ni_x is closer to V1 than the red lobe, opposite to those around the other Ni atoms with linear link Ni-Sn(Zr)-V1, whose red lobes are closer to V1. This difference in charge rearrangement is most likely the reason for the difference in energetics of FH-nNi from HH+nNi and is a reflection of different local bonding in FH and HH systems.

In Fig. 5.10, we give the band structures and DOS of HH+nNi systems, note that hereafter we consider only the lowest-energy state for each n. As one can see in Fig. 5.10(a,b,c), adding Ni to HH matrix has two effects: splitting of the host HH bands due to impurity induced symmetry lowering, and introducing defect states inside the gap. There is still some local residual symmetry which preserve the degeneracy of the valence band maximum at the Γ point. The splitting of the HH conduction bands reduce the band gap from ~ 0.5 eV to ~ 0.37 eV. The dispersion of the host
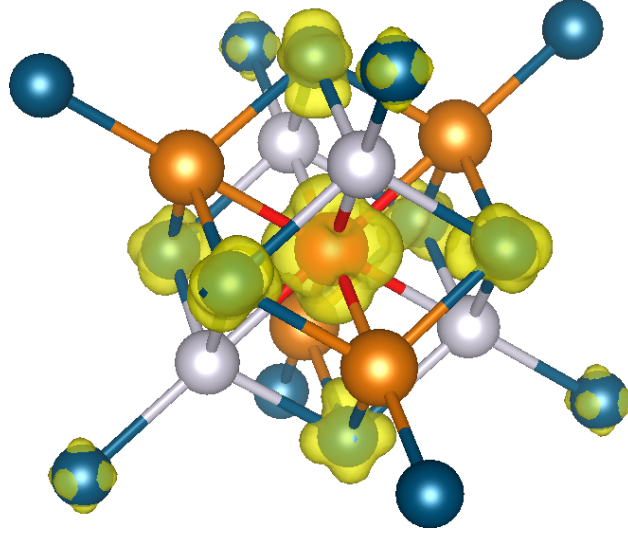
Figure 5.11: The isosurface of the charge density associated with the in-gap defect states in HH+1Ni. Host Ni are blue circles, excess Ni is the red circle, Zr are brown circles, Sn are gray circles.

bands near the gap changes slightly. There are two defect states per additional Ni located just below the HH conduction band edge. Projected density of states for HH+nNi reveal that the defect states in the gap are associated primarily with Ni-eg orbitals. When one excess Ni is added to the HH matrix, it brings 10 more electrons which occupy 5 Ni_1-d bands, 3 t_2g and 2 eg. All the Ni_1-d bands are below the Fermi level, the t_2g bands are located at ~ -1.5 eV, whereas the eg bands are located right below the HH conduction bands, giving rise to the in-gap states. The defect states in the gap are localized, its bandwidth is ~ 0.14 eV. The charge density associated with the in-gap defect states is given in Fig. 5.11, clearly showing the Ni-eg character. The dispersion of the defect bands is small in x, y, or z directions, but larger in other directions, such as Γ-M (110), Γ-R (111), which are directions of Ni_1-Zr(Sn) bonds.

When more Ni are added to the HH matrix, more impurity bands are introduced into the gap region, and eventually fill up the gap, converting the semiconducting state of HH into metallic state of FH. Comparing the DOS of HH+nNi (Fig. 5.10d), one can clearly see the evolution of the electronic structure. With one extra Ni, DOS starts to show a peak right below the conduction bands. As the number of excess Ni increases the peak gets higher and shifts downwards. These
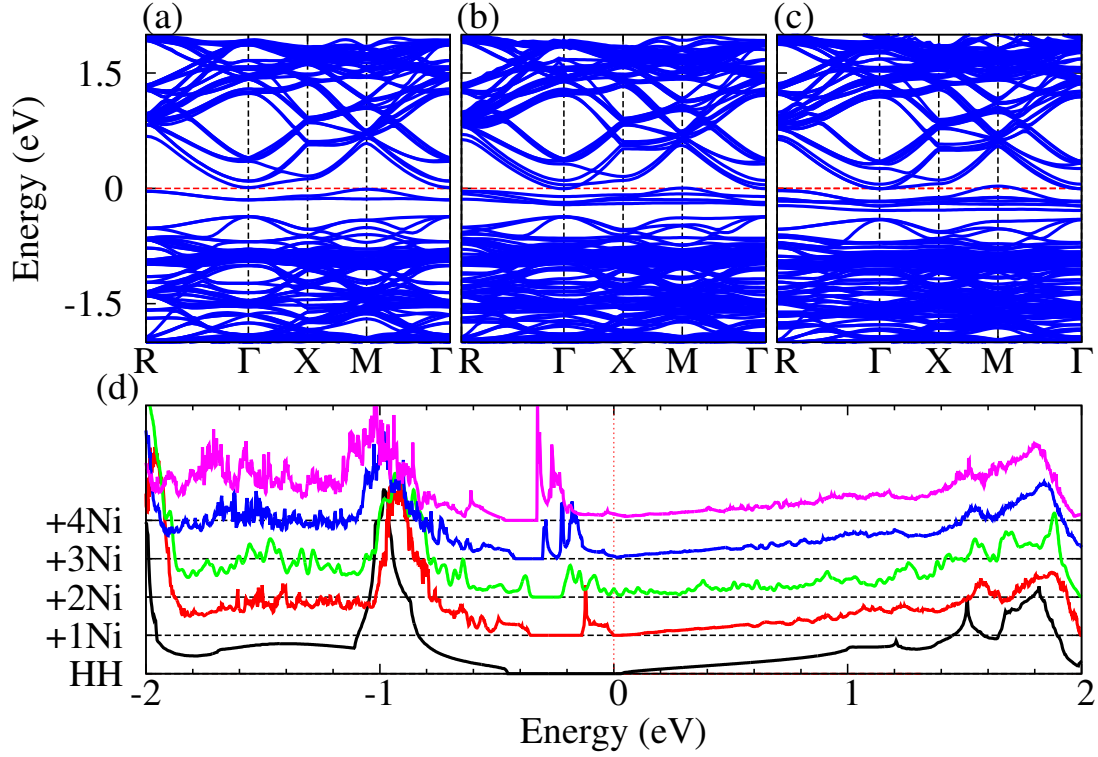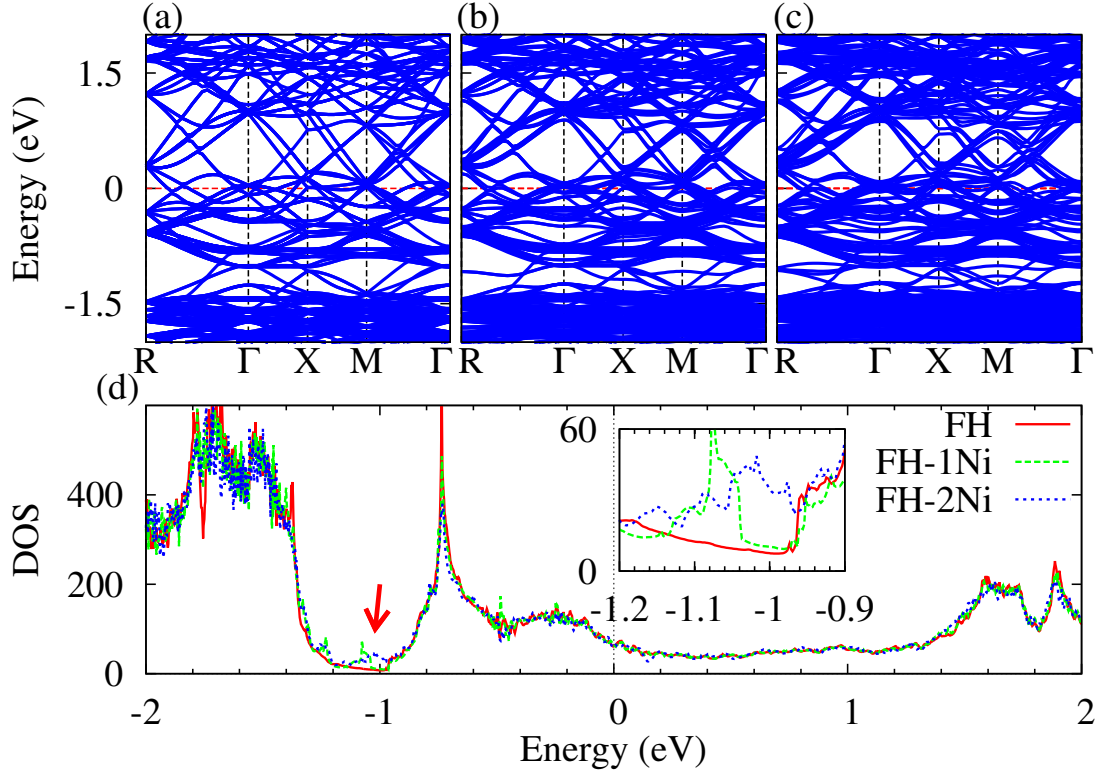
Figure 5.12: Evolution of electronic structure of FH with deficient Ni: band structures (a) FH, (b) FH-1Ni, and (c) FH-2Ni , and density of states of those systems. The inset show the DOS, indicated by the arrow, around -1 eV in small range [-1.2,-0.9].

localized defect states are occupied and act as donor-states which can inject carriers into the conduction bands and the system behaves like a *n*-type semiconductor. These states can affect the thermoelectric properties of HH-FH composite systems.

The effect of Ni-vacancy in FH is less subtle than that of Ni excess in HH. Fig. 5.12 gives the electronic structure of FH-*n*Ni. The dominant effect of Ni-vacancy on the band structure of FH is the band splitting, which makes it appears to be more complicated. One can see some extra bands appearing around ∼-1 eV. These extra bands give rise to a small peak in the DOS at ∼-1 eV (Fig. 5.12d inset). These effects, however, just introduce small perturbation in the DOS (figure 5.12d), which do not change the metallic properties of FH, at least for small concentration of Ni-vacancy.

5.4 Summary and Conclusion

To summarize this chapter, I have discussed the energetics and electronic structures of the HH-FH mixture, $ZrNi_{1+x}Sn$. The evolution from HH to FH and from FH to HH was studied using a $2 \times 2 \times 2$ supercell model. The focus is on the small concentration ($< 10\%$) limit of defects (excess Ni in HH and Ni-vacancy in FH).

The calculations predict an attractive interaction between excess Ni atoms in the HH matrix, i.e. the excess Ni atoms tend to come close to each other and form nano-clusters within the HH matrix. Vacancies in the FH matrix, on the other hand, are found to possibly occupy either of two crystallographic sites, h(1/4,1/4,1/4) or f(3/4,3/4,3/4), and their energetics are distinctively different from that of excess Ni in the HH matrix. If two Ni-vacancies in FH occupy the equivalent sites(either type h or f), the interaction between them is attractive at the distance larger or equal 6.32 Å and repulsive at smaller distance. If two Ni-vacancies in FH occupy the sites of different types (one at h-site and another at f-site), then the interaction is repulsive, the two vacancies tend to stay away from each other. Thus, at low concentration of vacancies, the nano-structure of HH in FH matrix is energetically not preferred.

Analysis of the change charge density shows that excess Ni (or Ni-vacancy) in HH (FH) causes large charge rearrangement in the host matrix. The charge rearrangement occurs mostly on Ni-sites and is larger at Ni sites which are connected to the excess Ni (Ni-vacancy) indirectly through one channel mediated by either a Zr or a Sn atom. The charge rearrangement is modest at the Ni-sites which are connected to the defect site through channels mediated by two atoms of the same type. FH with one Ni-vacancy has an interesting charge rearrangement at the Ni-sites connected to the vacancy through two channels mediated by one Zr and one Sn. This charge rearrangement is in different directions compared to that at other Ni-sites and is most likely responsible for the difference in energetics between FH-nNi and HH+nNi.

While the effect of Ni-vacancies in FH on the electronic structure is modest, the excess Ni in HH changes the HH's electronic structure dramatically. The excess Ni in HH introduces new impurity states in the gap of HH band structure, giving rise to finite density of states below the

117

conduction bands. Due to the in-gap impurity states, HH with excess Ni can behave like a *n*-type semiconductor.

The present study of ZrNi$_{1+x}$Sn agrees well with experimental and other theoretical studies on crystal and electronic structures of this mixture. The calculated results however cannot confirm or deny the energy filtering effect of the FH nano-inclusion in the HH matrix, which has been suggested by several authors to be the reason for the improvement in the material's thermoelectric properties. In order to understand that problem, larger-supercell calculations and transport studies are needed.

CHAPTER 6

CONCLUSION AND OUTLOOK

Thermoelectrics are an important part in the solution of the energy problems. They can contribute to both improving energy conversion efficiency (saving waste heat), and power generation. In the last several years the field of thermoelectrics has developed quickly; however, there are still emerging needs of new discoveries in material for thermoelectric applications, including finding new compounds and finding new ways of improving the existing ones.

The job of increasing the figure of merit ZT of thermoelectrics is challenging since there is a competing relation between quantities that are involved in ZT. There are several ideas of how to improve ZT including, but not limited to, introducing resonant states, energy filtering, creating aharmonicity, etc. , all of which, now, can involve the inclusion of low-dimensional structures, and require a deeper understanding of electronic structure and transport properties in complex multi-component systems.

The advances in theories and computational methods, density functional theory in particular, of electronic structure have been extremely helpful in studying physical properties of materials. Density functional theory calculations have improved greatly in the last decade, in both accuracy and productivity. The improvement in density functional theory calculations is due to the improvement of approximations used in treating the effect of electron-electron interaction, more interaction and correction terms are added, going from LDA/GGA to hybrid functional and to random phase approximation.

In this thesis, I have employed density functional theory first principles cacluations, using several approximations including LDA/GGA, LDA+U, meta-GGA and hybrid functional approximation, to study electronic structures and transport properties of several novel thermoelectric materials, including the Heusler compound Fe_2VAl, Cu_3SbSe_4 and its related tetrahedrally coordinated systems, and the nanocomposites of Half-Heusler and Heusler compounds.

Chapter 3 discusses the electronic structure and thermopower of the Heusler compound Fe_2VAl. Using LDA+U, I have shown that Fe_2VAl is a narrow band gap semiconductor (E_g=0.5 eV), rather than a pseudo-gap system as predicted in LDA/GGA (negative gap). The values of intra-site Coulomb repulsion, $U_{Fe} = 4$ eV and $U_V = 1.5$ eV, were calculated using constrained density functional theory. Using electronic structure obtained from LDA+U, I have studied the thermopower of Fe_2VAl and have shown that the results are in better agreement with experiment, compared to the results calculated with GGA band structure. Fe_2VAl is shown to be a better p-type thermoelectric due to large degeneracy at the top of the valence bands. I have also noted that the better agreement with experimental data can be achieved if a smaller value of U (1 eV) is used. Furthermore, the pseudo-gap behavior observed in certain experiments is still not understood. This may be due to new physics, such as defects, dynamic interaction or excitonic effect and further works need to be done in order to have a better understanding of this material.

In chapter 4, I discussed the band gap problem in Cu_3SbSe_4 and related tetrahedrally coordinated compounds I_3-V-VI_4 (belonging to the Famatinite and the Enargite families), where I=Cu, V=P, As, Sb, or Bi and VI=S, or Se, and have pointed out the importance of lone-pare electron of group V elements in the band gap formation in this family of materials. Both GGA, LDA+U and hybrid functional calculations were done and discussed. A simple bonding-antibonding scheme explaining the band-gap formation has been proposed. In this simple picture, the lone-pair electrons of V stereochemically interact with the surrounding VI-p orbital, giving rise to a special band (BOI) which is the lowest of the conduction bands, forming a band gap. Exceptions are those systems which contain Bi, all of them are found to be (semi)metal in all the approximations. I have also studied the relation between the value of band gaps and the bond length between V and VI elements and have shown that the relation is almost linear, band gap decreases with increasing bong length. The results suggested that one can tune the band gap in these compounds by choosing proper composition of dopants.

Chapter 5 has been dedicated to the study of the problem of nanostructure inclusion of Heusler ($ZrNi_2Sn$) compounds in the Half-Heusler (ZrNiSn) matrix and vice versa, focusing on the low

density limit using $2 \times 2 \times 2$ periodic supercell model. The electronic structures of the nanocomposites have been discussed. It is important to note that all approximations to density functional theory tend to overestimate the band gap of ZrNiSn. The results predict that extra Ni atoms in ZrNiSn tend to form nano clusters even at low concentrations, but excess Ni-vacancies in $ZrNi_2Sn$ do not. The latter tend to distribute almost evenly in space. These findings are in agreement with experiments. Inclusion of $ZrNi_2Sn$ phase in ZrNiSn introduces in-gap impurity states corresponding to a finite density of state right below the conduction band edge, the more excess Ni are put, the more states are introduced, in agreement with susceptibility measurement. These in-gap states change the electronic structure, and consequently the thermoelectric properties of ZrNiSn. The nanocomposite of $ZrNiSn$-$ZnNi_2Sn$ acts like a n-type semiconductors. The detail effects of the nanostructure inclusion on thermoelectric properties of ZrNiSn, however, have not been discussed in this thesis. Further works are under progress.

In conclusion, I have studied several systems of thermoelectric significance and have contributed to a better understanding of some of their fundamental issues. The results have shown that even though climbing up the density functional theory ladder of approximation, in general, improves the accuracy of electronic structure calculations, there is no universal approximation which is good enough to be used for all the materials – LDA+U gave reasonable results for Fe_2VAl but failed in predicting band gaps in tetrahedrally coordinated systems, and both GGA, LDA+U and hybrid functional calculation overestimate the band gap in ZrNiSn. It is clear that there are still some outstanding questions which have not been addressed in this thesis. For examples: What are dynamic correlation effects in pseudo-gap systems involving d-electrons? How can one make critical evaluations of non-local exchange (hybrid functional) theories vis-a-vis mBJ, and other approximations? What defects can occur in Heusler and tetrahedrally coordinated systems, and their roles in electronic structures and thermoelectric properties of these compounds? What are the effects of nano-inclusion on thermoelectric properties of Half-Heusler–Heusler composite? Whether transport and energy filtering effects are taken place in such the system? Further work addressing some of those questions is under progress.

BIBLIOGRAPHY

BIBLIOGRAPHY

[1] *World energy outlook 2012* (International Energy Agency, Organisation for Economic Co-operation and Development, 2012), retrieved from http://www.oecd-ilibrary.org.

[2] T. Seebeck, Proc. Prussian Acad. Sci. (1825-273).

[3] G. Magnus, Poggendorf's Annalen der Physik **83**, 469 (1851).

[4] I. B. Cadoff and E. Miller, eds., *Thermoelectric materials and devices*, Materials Technology Series (Reinhold Publishing Corporation, New York, 1960).

[5] G. Mahan, B. Sales, and J. Sharp, Physics Today **50**, 42 (1997).

[6] R. R. Heikes and J. Roland W. Ure, *Thermoelectricity: science and engineering* (Inter-science publishers, New York - London, 1961).

[7] M. V. Vedernikov and E. K. Iordanishvili, in *XVII International Conference on Thermoelectrics, 1998. Proceedings ICT 98* (1998), pp. 37–42.

[8] NASA, *Radioisotope power systems for space exploration* (2011), nASA facts.

[9] *New horizons mission powered by space radioisotope power systems*, URL `http://energy.gov/ne`.

[10] R. R. Furlong and E. J. Wahlquist, Nuclear News **42**, 2635 (1999).

[11] G. J. Snyder, The Electrochemical Society Interface p. 54 (2008), and therein references.

[12] J. Yang and F. R. Stabler, Journal of Elec Materi **38**, 1245 (2009).

[13] C. B. Vining, Nat Mater **8**, 83 (2009).

[14] M. Zebarjadi, K. Esfarjani, M. S. Dresselhaus, Z. F. Ren, and G. Chen, Energy Environ. Sci. (2011), and therein references.

[15] T. M. Tritt, Annual Review of Materials Research **41**, 433 (2011).

[16] J. W. Fairbanks, *Automotive thermoelectric generators and hvac* (2012), presented at Directions in Engine-Efficiency and Emissions Research (DEER) Conference 2012, URL `http://www1.eere.energy.gov/vehiclesandfuels/resources/conferences/deer/`.

[17] G. D. Mahan and G. O. Sofo, in *Proc. Natl. Acad. Sci.* (1996), vol. 93, p. 7435.

[18] J. O. Sofo and G. D. Mahan, Phys. Rev. B **49**, 4565 (1994).

[19] E. J. Skoug, C. Zhou, Y. Pei, and D. T. Morelli, Jr. Electronic. Matter **38**, 1221 (2009).

[20] S. Ahmad, K. Hoang, and S. D. Mahanti, Phys. Rev. Lett. **96**, 056403 (2006).

[21] J. P. Heremans, V. Jovovic, E. S. Toberer, A. Saramat, K. Kurosaki, A. Charoenphakdee, S. Yamanaka, and G. J. Snyder, Science **321**, 554 (2008).

[22] S. V. Faleev and F. Léonard, Phys. Rev. B **77**, 214304 (2008).

[23] J. P. A. Makongo, D. K. Misra, X. Zhou, A. Pant, M. R. Shabetai, X. Su, C. Uher, K. L. Stokes, and P. F. P. Poudeu, J. Am. Chem. Soc. **133**, 18843 (2011).

[24] D. M. Rowe, Journal of Physics D: Applied Physics **7**, 1843 (1974).

[25] G. A. Slack and M. A. Hussain, Journal of Applied Physics **70**, 2694 (1991).

[26] D. T. Morelli and G. A. Slack, *High Thermal Conductivity Materials* (Springer, New York, 2006), chap. 2, p. 37.

[27] E. J. Skoug, J. D. Cain, and D. T. Morelli, Appl. Phys. Lett. **96**, 181905 (2010).

[28] Y. Zhang, E. Skoug, J. Cain, V. Ozolins, D. Morelli, and C. Wolverton, Phys. Rev. B **85**, 054306 (2012).

[29] M. Faraday, *Experimental researches in electricity* (printers And Publishers To The University Of London, London, 1949), vol. I, 2nd ed., sect. 432-6.

[30] A. H. Wilson, Proc. R. Soc. Lond. A **133**, 458 (1931).

[31] H. H. Lin and J. B. Kuo, in *Wiley Encyclopedia of Electrical and Electronics Engineering* (John Wiley & Sons, Inc., 2001), ISBN 9780471346081.

[32] M. Z. Hasan and C. L. Kane, Rev. Mod. Phys. **82**, 3045 (2010).

[33] J. Chu and A. Sher, *Introduction* (Springer New York, 2008), pp. 1–17.

[34] G. D. Mahan, **65**, 1578 (1989).

[35] D. Do, M.-S. Lee, and S. D. Mahanti, Phys. Rev. B **84**, 125104 (2011).

[36] D. Do, V. Ozolins, S. D. Mahanti, M.-S. Lee, Y. Zhang, and C. Wolverton, J. Phys.: Condens. Matter **24**, 415502 (2012).

[37] D. Do and S. D. Mahanti, arXiv e-print 1306.0503 (2013).

[38] R. M. Martin, *Electronic Structure, Basic Theory and Practical Method* (Cambridge University Press, 2004).

[39] L. H. Thomas, Proc. Cambridge Philos. Soc. **23**, 542 (1927).

[40] E. Fermi, Atti. Accad. Naz. Lincei, Cl. Sci. Fis. Mat. Nat. Rend. **6**, 602 (1927).

[41] E. Schrodinger, Phys. Rev. **28**, 1049 (1926).

[42] P. Hohenberg and W. Kohn, Phys. Rev. **136**, B864 (1964).

[43] W. Kohn and L. J. Sham, Phys. Rev. **140**, A1133 (1965).

[44] W. Kohn, Rev. Mod. Phys. **71**, 1253 (1999).

[45] M. Levy, J. P. Perdew, and V. Sahni, Phys. Rev. A **30**, 2745 (1984).

[46] J. P. Perdew, A. Ruzsinszky, L. A. Constantin, J. Sun, and G. I. Csonka, J. Chem. Theory Comput. **5**, 902 (2009).

[47] J. P. Perdew, K. Burke, and M. Ernzerhof, Phys. Rev. Lett. **77**, 3865 (1996).

[48] J. P. Perdew and Y. Wang, Phys. Rev. B **45**, 13244 (1992).

[49] E. Engel and S. H. Vosko, Phys. Rev. B **47**, 13164 (1993).

[50] Z. Wu and R. E. Cohen, Phys. Rev. B **73**, 235116 (2006).

[51] J. Tao, J. P. Perdew, V. N. Staroverov, and G. E. Scuseria, Phys. Rev. Lett. **91**, 146401 (2003).

[52] F. Tran and P. Blaha, Phys. Rev. Lett. **102**, 226401 (2009).

[53] A. D. Becke, Phys. Rev. A **38**, 3098 (1988).

[54] C. Lee, W. Yang, and R. G. Parr, Phys. Rev. B **37**, 785 (1988).

[55] A. D. Becke, J. Chem. Phys. **96**, 5648 (1993).

[56] A. D. Becke, J. Chem. Phys. **104**, 1040 (1996).

[57] D. I. Bilc, R. Orlando, R. Shaltaf, G.-M. Rignanese, J. Íñiguez, and P. Ghosez, Phys. Rev. B **77**, 165107 (2008).

[58] C. Adamo and V. Barone, The Journal of Chemical Physics **110**, 6158 (1999).

[59] J. Heyd, G. E. Scuseria, and M. Ernzerhof, The Journal of Chemical Physics **118**, 8207 (2003).

[60] J. Heyd and G. E. Scuseria, The Journal of Chemical Physics **121**, 1187 (2004).

[61] J. Heyd, G. E. Scuseria, and M. Ernzerhof, The Journal of Chemical Physics **124**, 219906 (2006).

[62] P. A. M. Dirac, Proc. Cambridge Philos. Soc. **26**, 376 (1930).

[63] J. C. Slater, Phys. Rev. **81**, 385 (1951).

[64] A. Svane and O. Gunnarsson, Pys. Rev. Lett. **65**, 1148 (1990).

[65] V. I. Anisimov, F. Aryasetiawan, and A. I. Lichtenstein, Journal of Physics: Condensed Matter **9**, 767 (1997).

[66] V. I. Anisimov and O. Gunnarsson, Phys. Rev. B **43**, 7570 (1991).

[67] O. Gunnarsson, O. K. Andersen, O. Jepsen, and J. Zaanen, Phys. Rev. B **39**, 1708 (1989).

[68] G. K. H. Madsen and P. Novák, Europhys. Lett. **69**, 777 (2005).

[69] V. I. Anisimov, M. A. Korotin, and E. Z. Kormaev, J Phys.: Condens. Matter **2**, 3973 (1990).

[70] M. J. Han, T. Ozaki, and J. yu, Phys. Rev. B **73** (2006).

[71] L. Hedin, Phys. Rev. **139**, A796 (1965).

[72] A. D. Becke, The Journal of Chemical Physics **98**, 1372 (1993).

[73] J. M. Ziman, *Principles of the Theory of Solids* (Cambridge University Press, 1964).

[74] G. K. Madsen and D. J. Singh, Computer Physics Communications **175**, 67 (2006).

[75] P. E. Blöchl, Phys. Rev. B **50**, 17953 (1994).

[76] G. Kresse and D. Joubert, Phys. Rev. B **59**, 1758 (1999).

[77] G. Kresse and J. Hafner, Phys. Rev. B **47**, 558 (1993).

[78] G. Kresse and J. Furthmüller, Computational Materials Science **6**, 15 (1996).

[79] G. Kresse and J. Furthmüller, Phys. Rev. B **54**, 11169 (1996).

[80] K. Schwarz and P. Blaha, Computational Materials Science **28**, 259 (2003), proceedings of the Symposium on Software Development for Process and Materials Design.

[81] S. L. Dudarev, G. A. Botton, S. Y. Savrasov, C. J. Humphreys, and A. P. Sutton, Phys. Rev. B **57**, 1505 (1998).

[82] Y. Nishino, M. Kato, S. Asano, K. Soda, M. Hayasaki, and U. Mizutani, Phys. Rev. Lett. **79**, 1909 (1997).

[83] C.-S. Lue and J. H. Ross, Phys. Rev. B **58**, 9763 (1998).

[84] H. Okamura, J. Kawahara, T. Nanba, S. Kimura, K. Soda, U. Mizutani, Y. Nishino, M. Kato, I. Shimoyama, H. Miura, et al., Phys. Rev. Lett. **84**, 3674 (2000).

[85] T. Graf, C. Felser, and S. S. Parkin, Progress in Solid State Chemistry **39**, 1 (2011).

[86] J. Korringa, Physica **16**, 601 (1950).

[87] D. J. Singh and I. I. Mazin, Phys. Rev. B **57**, 14352 (1998).

[88] M. Weinert and R. E. Watson, Phys. Rev. B **58**, 9732 (1998).

[89] R. Weht and W. E. Pickett, Phys. Rev. B **58**, 6855 (1998).

[90] G. Y. Guo, G. A. Botton, and Y. Nishino, J. Phys.: Condens. Matter **10**, L119 (1998).

[91] M. Kumar, T. Nautiyal, and S. Auluck, Journal of Physics: Condensed Matter **21**, 446001 (2009).

[92] C. S. Lue and Y.-K. Kuo, Phys. Rev. B **66**, 085121 (2002).

[93] Y. Nishino, S. Deguchi, and U. Mizutani, Phys. Rev. B **74**, 115115 (2006).

[94] M. Vasundhara, V. Srinivas, and V. V. Rao, Phys. Rev. B **77**, 224415 (2008).

[95] Y. Nishino, Intermetallics **8**, 1233 (2000).

[96] D. I. Bilc and P. Ghosez, Phys. Rev. B **83**, 205204 (2011).

[97] H. C. Kandpal, G. H. Fecher, C. Felser, and G. Schönhense, Phys. Rev. B **73**, 094422 (2006).

[98] B. Balke, G. H. Fecher, H. C. Kandpal, C. Felser, K. Kobayashi, E. Ikenaga, J.-J. Kim, and S. Ueda, Phys. Rev. B **74**, 104405 (2006).

[99] P. Larson, S. D. Mahanti, S. Sportouch, and M. G. Kanatzidis, Phys. Rev. B **59**, 15660 (1999).

[100] M.-S. Lee and S. D. Mahanti (to be published), to be published.

[101] G. Snyder, Nature materials **7**, 105 (2008), and therein references.

[102] H. Grimm and A. Sommerfeld, Zeitschrift für Physik **36**, 36 (1926).

[103] A. Rockett and R. W. Birkmire, Journal of Applied Physics **70**, R81 (1991).

[104] S. Chichibu, T. Mizutani, K. Murakami, T. Shioda, T. Kurafuji, H. Nakanishi, S. Niki, P. J. Fons, and A. Yamada, Journal of Applied Physics **83**, 3678 (1998).

[105] E. J. Skoug, J. D. Cain, and D. T. Morelli, Journal of Alloys and Compounds **506**, 18 (2010).

[106] E. Skoug, J. Cain, P. Majsztrik, M. Kirkham, E. Lara-Curzio, and D. Morelli, Science of Advanced Materials **3**, 602 (2011).

[107] E. J. Skoug and D. T. Morelli, Phys. Rev. Lett. **107**, 235901 (2011).

[108] C. Sevik and T. Çağin, Journal of Applied Physics **109**, 123712 (2011).

[109] C. Yang, F. Huang, L. Wu, and K. Xu, Journal of Physics D: Applied Physics **44**, 295404 (2011).

[110] H. Nakanishi, S. Endo, and T. Irie, Jpn. J. Appl. Phys. **8**, 443 (1969).

[111] O. Madelung, *Semiconductors: Data Handbook* (Springer, 2004).

[112] L. Pauling, *The Nature of Chemical Bond and the Structure of Molecules and Crystals* (Cornell University Press, New York, 1939).

[113] J. C. Phillips, *Bonds and Bands in Semiconductors* (Academic Press, New York and London, 1973).

[114] G. N. Lewis, J. Am. Chem. Soc. **38**, 762 (1916).

[115] I. Langmuir, J. Am. Chem. Soc. **41**, 868 (1919).

[116] Y. J. Wang, H. Lin, T. Das, M. Z. Hasan, and a. Bansil, New Journal of Physics **13**, 085017 (2011).

[117] J. Garin and E. Parthé, **28**, 3672 (1972).

[118] A. Pfitzner and S. Reiser, **217**, 51 (2002).

[119] A. Pfitzner and T. Bernert, **219**, 20 (2004).

[120] A. Pfitzner, Z. Kristallogr. **209**, 685 (1994).

[121] A. Pfitzner, Z. anorg. allg. Chem. **621**, 685 (1995).

[122] M. S. Hybertsen, M. Schlüter, and N. E. Christensen, Phys. Rev. B **39**, 9028 (1989).

[123] R. Laskowski, P. Blaha, and K. Schwarz, Phys. Rev. B **67**, 075102 (2003).

[124] M. Papagno, D. Pacilé, G. Caimi, H. Berger, L. Degiorgi, and M. Grioni, Phys. Rev. B **73**, 115120 (2006).

[125] A. Önsten, M. Månsson, T. Claesson, T. Muro, T. Matsushita, T. Nakamura, T. Kinoshita, U. O. Karlsson, and O. Tjernberg, Phys. Rev. B **76**, 115127 (2007).

[126] I. Galanakis, P. Mavropoulos, and P. H. Dederichs, J. Phys. D: Appl. Phys. **39**, 765 (2006).

[127] I. Galanakis and P. Mavropoulos, J. Phys.: Condens. Matter **19**, 315213 (2007).

[128] M. I. Katsnelson, V. Y. Irkhin, L. Chioncel, A. I. Lichtenstein, and R. A. de Groot, Rev. Mod. Phys. **80**, 315 (2008).

[129] S. Picozzi, in *Advances in Solid State Physics*, edited by P. D. R. Haug (Springer Berlin Heidelberg, 2008), no. 47 in Advances in Solid State Physics, pp. 129–141, ISBN 978-3-540-74324-8, 978-3-540-74325-5.

[130] T. Graf, S. S. P. Parkin, and C. Felser, IEEE Transactions on Magnetics **47**, 367 (2011).

[131] F. Casper, T. Graf, S. Chadov, B. Balke, and C. Felser, Semiconductor Science and Technology **27**, 063001 (2012).

[132] Z. Bai, L. Shen, G. Han, and Y. p. Feng, arXiv:1301.5455 (2013).

[133] I. Galanakis, arXiv:1302.4699 (2013).

[134] F. G. Aliev, N. Brandt, V. V. Kozyr'kov, V. V. Moshchalkov, R. V. Skolozdra, Y. V. Stadnyk, and V. K. Pecharski, Pis'ma Zhr. Eksp. Teor. Fiz. **45**, 535 (1987).

[135] F. G. Aliev, V. V. Kozyrkov, V. V. Moshchalkov, R. V. Scolozdra, and K. Durczewski, Zeitschrift für Physik B Condensed Matter **80**, 353 (1990).

[136] F. Aliev, Physica B: Condens. Matter **171**, 199 (1991).

[137] F. G. Aliev, V. V. Pryadun, R. Villar, S. Vieira, J. M. Calleja, N. Mestres, and R. V. Scolozdra, Int. J. Mod. Phys. B **07**, 383 (1993).

[138] N. Mestres, J. Calleja, F. Aliev, and A. Belogorokhov, Solid State Commun. **91**, 779 (1994).

[139] A. Slebarski, A. Jezierski, S. Lütkehoff, and M. Neumann, Phys. Rev. B **57**, 6408 (1998).

[140] H. Hohl, A. P. Ramirez, C. Goldmann, G. Ernst, B. Wölfing, and E. Bucher, J. Phys.: Condens. Matter **11**, 1697 (1999).

[141] P. Larson, S. D. Mahanti, and M. G. Kanatzidis, Phys. Rev. B **62**, 12754 (2000).

[142] Q. Shen, L. Zhang, L. Chen, T. Goto, and T. Hirai, J. Mater. Sci. Lett. **20**, 21972199 (2001).

[143] J. D. Germond, P. J. Schilling, N. J. Takas, and P. F. P. Poudeu, MRS Proc. **1267** (2010).

[144] Y. Kimura, T. Tanoguchi, and T. Kita, Acta Materialia **58**, 4354 (2010).

[145] P. Qiu, J. Yang, X. Huang, X. Chen, and L. Chen, Appl. Phys. Lett. **96**, 152105 (2010).

[146] Y. Kimura, T. Tanoguchi, Y. Sakai, Y.-W. Chai, and Y. Mishima, MRS Proc. **1295** (2011).

[147] M.-S. Lee and S. D. Mahanti, Phys. Rev. B **85**, 165149 (2012).

[148] S. Chen, K. C. Lukas, W. Liu, C. P. Opeil, G. Chen, and Z. Ren, Adv. Energy Mater. (2013).

[149] V. Romaka, P. Rogl, L. Romaka, Y. Stadnyk, A. Grytsiv, O. Lakh, and V. Krayovskii, Intermetallics **35**, 45 (2013).

[150] D. F. Zou, S. H. Xie, Y. Y. Liu, J. G. Lin, and J. Y. Li, J. Appl. Phys. **113**, 193705 (2013).

[151] S. Sakurada and N. Shutoh, Appl. Phys. Lett. **86**, 082105 (2005).

[152] L. Chaput, J. Tobola, P. Pécheur, and H. Scherrer, Phys. Rev. B **73**, 045121 (2006).

[153] S.-W. Kim, Y. Kimura, and Y. Mishima, Intermetallics **15**, 349 (2007).

[154] L. L. Wang, L. Miao, Z. Y. Wang, W. Wei, R. Xiong, H. J. Liu, J. Shi, and X. F. Tang, J. Appl. Phys. **105**, 013709 (2009).

[155] C. Yu, T.-J. Zhu, R.-Z. Shi, Y. Zhang, X.-B. Zhao, and J. He, Acta Materialia **57**, 2757 (2009).

[156] H. Hazama, M. Matsubara, R. Asahi, and T. Takeuchi, Journal of Applied Physics **110**, 063710 (2011).

[157] J. P. Makongo, D. K. Misra, J. R. Salvador, N. J. Takas, G. Wang, M. R. Shabetai, A. Pant, P. Paudel, C. Uher, K. L. Stokes, et al., Journal of Solid State Chemistry **184**, 2948 (2011).

[158] S. Poon, D. Wu, S. Zhu, W. Xie, T. Tritt, P. Thomas, and R. Venkatasubramanian, Journal of Materials Research **26**, 2795 (2011).

[159] J. E. Douglas, C. S. Birkel, M.-S. Miao, C. J. Torbet, G. D. Stucky, T. M. Pollock, and R. Seshadri, App. Phys. Lett. **101**, 183902 (2012).

[160] Y. W. Chai and Y. Kimura, Appl. Phys. Lett. **100**, 033114 (2012).

[161] G. Joshi, T. Dahal, S. Chen, H. Wang, J. Shiomi, G. Chen, and Z. Ren, Nano Energy **2**, 82 (2013).

[162] O. Appel, M. Schwall, D. Mogilyansky, M. Köhne, B. Balke, and Y. Gelbstein, Journal of Electronic Materials **42**, 1340 (2013).

[163] C. S. Birkel, J. E. Douglas, B. R. Lettiere, G. Seward, N. Verma, Y. Zhang, T. M. Pollock, R. Seshadri, and G. D. Stucky, Physical Chemistry Chemical Physics **15**, 6990 (2013).

[164] K. Kirievsky, Y. Gelbstein, and D. Fuks, Journal of Solid State Chemistry **203**, 247 (2013).

[165] X. Yan, W. Liu, S. Chen, H. Wang, Q. Zhang, G. Chen, and Z. Ren, Adv. Energy Mater. (2013).

[166] R. A. Downie, D. A. MacLaren, R. I. Smith, and J. W. G. Bos, Chem. Commun. **49**, 4184 (2013).

[167] Y. Stadnyk, L. Romaka, A. Horyn, A. Tkachuk, Y. Gorelenko, and P. Rogl, Journal of Alloys and Compounds **387**, 251 (2005).

[168] H. Akai, Journal of Physics: Condensed Matter **1**, 8045 (1989).

[169] R. M. Nieminen, *Topics in Applied Physics: Theory of defects in semiconductors* (Springer, 2006), vol. 104, pp. 36–40.

[170] S. Öğüt and K. M. Rabe, Phys. Rev. B **51**, 10443 (1995).

[171] H. J. Monkhorst and J. D. Pack, Phys. Rev. B **13**, 5188 (1976).

[172] S. B. Zhang, S.-H. Wei, A. Zunger, and H. Katayama-Yoshida, Phys. Rev. B **57**, 9642 (1998).

[173] P. Larson, S. D. Mahanti, S. Sportouch, and M. G. Kanatzidis, Phys. Rev. B **59**, 15660 (1999).